Reverberation Chamber Characterization Using Enhanced Backscatter Coefficient Measurements

by

Colton Ray Dunlap

B.S., New Mexico Institute of Mining and Technology, 2009

A thesis submitted to the

Faculty of the Graduate School of the

University of Colorado in partial fulfillment

of the requirements for the degree of

Doctor of Philosophy

Department of Electrical, Computer and Energy Engineering

2013

This thesis entitled:
Reverberation Chamber Characterization Using Enhanced Backscatter Coefficient Measurements
written by Colton Ray Dunlap
has been approved for the Department of Electrical, Computer and Energy Engineering

_____

Edward Kuester

_____

Dr. Christopher Holloway

Date _____

The final copy of this thesis has been examined by the signatories, and we find that both the
content and the form meet acceptable presentation standards of scholarly work in the above
mentioned discipline.

Dunlap, Colton Ray (Ph.D., Electrical Engineering)

Reverberation Chamber Characterization Using Enhanced Backscatter Coefficient Measurements

Thesis directed by Professor Edward Kuester

The primary focus of this thesis is to evaluate the use of the enhanced backscatter coefficient as a quantity for characterizing the spatial uniformity of the reverberation chamber (RC). An RC is a statistical measurement facility constructed from a large metallic hallow cavity containing an irregularly shaped paddle stirrer for mixing electromagnetic fields to obtain many statistically independent samples. The average power, measured from antennas placed inside of the RC, is ideally uniform over any chosen antenna position and orientation within the RCs working volume. Spatial uniformity is a fundamental assumption to all RC theoretical analysis, and thus the spatial dependence of the RC is directly related to the uncertainty of the measurements. Comparisons are made with standard multiple-configuration measurements (different antenna positions) to show that comparable values of standard deviation caused by spatial non-uniformity are obtained using the transfer function (as typically used) and the enhanced backscatter coefficient. Additionally, it is shown that the enhanced backscatter coefficient for an ideal RC is theoretically a constant value of 2, but has variation over frequency when measured. This variation over frequency is used in a single-configuration measurement to obtain values of standard deviation that are nearly the same as those found using multiple-configuration measurements. This is possible because the statistical variation of the reverberation chamber is similar over frequency and over different measurement positions. Furthermore, data is presented from various tests showing that the value of the enhanced backscatter coefficient is sensitive to calibration issues, and the improper use of frequency stirring. This helps to justify that the enhanced backscatter coefficient can be used as a benchmark quantity for determining if computations from the RC measured data are useful and can be trusted. One- and two-dimensional Greens function models are also used to explore the enhanced backscatter coefficient value for different types of stirring mechanisms. Lastly, application of the enhanced

backscatter coefficient for determining the total efficiency of an antenna measured in the reverberation chamber is presented. Along with the estimates of total efficiency, the confidence interval of the results is computed from the frequency variation of the enhanced backscatter coefficient.

Acknowledgements

First and foremost, I would like to thank Professor Edward Kuester and Dr. Christopher Holloway. Professor Kuester has been an extremely insightful instructor and a very patient and knowledgeable adviser. Dr. Holloway was instrumental in getting me the research opportunity at NIST and has provided invaluable guidance in this work. I would also like to thank John Ladbury, Dr. Ryan Pirkl, and Jason Coder. I learned much from Mr. Ladbury during our many discussions about reverberation chamber measurement and analysis techniques. Dr. Pirkl assisted me quite often with understanding statistical analysis and computational methods. Mr. Coder often assisted me with understanding measurement processes as well as other practical matters. I also thank the rest of my NIST RF Fields Group colleagues for their assistance and cooperation in conducting various tests. I additionally would like to thank the thesis committee members Dr. David A. Hill, Professor Scott E. Palo, and Professor Jem Corcoran for their review of my work and helpful comments.

Lastly, I dedicate this work to my wife April, son Isaac, daughter Autumn, mother Juanita, father George, and sister Katie.

Contents

Tables

Table

Figures

Figure

Chapter 1

Introduction

Real world electromagnetic (EM) measurements can be influenced by a large number of factors, many of which cannot be controlled. If sources of electromagnetic interference (EMI) are present in the area, additional errors will afflict measurements designed to characterize antennas and wireless devices. The widespread presence and never-ending use of wireless communications means that field experiments can be difficult to perform, especially if the measurements require high precision and/or low powers relative to the background noise. Nevertheless, field experiments are important for determining if the device under test (DUT) will operate correctly in the environment it is intended for. Generally, however, these tests are performed after the device has been fully characterized under idealized conditions that can be compared to analytic or numerical models.

In order to eliminate uncontrolled variables, people have developed many different idealized environments. These include anechoic chambers, transverse electromagnetic (TEM) cells, and reverberation chambers (RCs). Each of these three environments have idealized characteristics that allow measurements to be compared with various models. Anechoic chambers have non-reflecting boundaries and they ideally behave like infinite free space. TEM cells are essentially large transmission lines of constant characteristic impedance that allow propagation of the warped plane waves that are the fundamental modes of the cell. An RC is an electrically large shielded metal room that is used at frequencies high enough to allow many resonant cavity modes to be excited simultaneously. Mode stirring allows measurements to be thought of as being statistically uniform, and comparisons can then be made with models that subject the DUT to plane wave radiation

incident from all directions and containing all polarizations. It should be noted that while each measurement environment has various means of collecting measurement samples, measurements are additionally taken as a function of frequency by sweeping the sources over some range of operating frequencies. Measurements can also be taken as a function of time as well, but these types of measurements will not be considered here. Any time domain data that is presented will have been obtained using the inverse Fourier transform of certain frequency domain data.
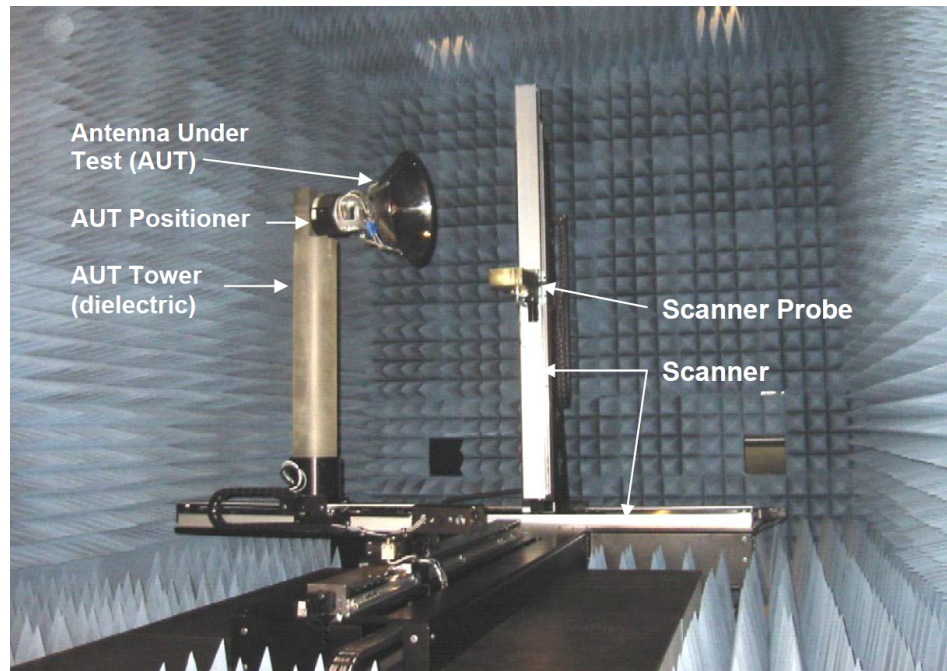
Figure 1.1: An anechoic chamber located at Ohio University's Russ College of Engineering and Technology [1].

Since anechoic chambers have non-reflecting boundaries, EM radiation is allowed to propagate away from an EM source as if it were in free space. As such, these environments are highly useful for characterizing antenna and wireless device radiation patterns as a function of angle. In addition, measurements can be directly compared with models that assume no outer boundary reflections, as is typically done for antennas. An example picture of an anechoic chamber is shown in Figure 1.1. As shown, the radiated power transmitted from the antenna under test (AUT) directed towards the scanner probe antenna is measured. The positioners allow measurement samples to

be collected at different AUT angles and scanner positions, creating two and three dimensional pictures of the antenna's radiation pattern. While these systems work very well, measurements of total radiated power (TRP) require many samples at many points around the AUT, as well as at different polarization angles with respect to the probe. In addition, the requirement for the AUT or DUT to be mounted to a positioner to be reoriented limits the size and form factor of the test objects. Also, the large cost of these facilities is often prohibitive for potential users. For a history of anechoic chambers see [16]. For a discussion on characterization of anechoic chambers using reflectivity measurements see [2]. For a comparative look at the effectiveness of different absorber materials used in anechoic chamber measurements see [24]. For a comprehensive treatment of anechoic chamber uses, specifications, and design considerations see [20].

TEM cells allow users to subject a DUT to a well-characterized (ideally uniform) field, or conversely the radiation from a DUT can couple into the TEM mode of the cell. These structures require that the frequency is lower than the cutoff frequency of any mode other than the fundamental mode (where the cutoff frequency is zero). By moving the DUT to different orientations within the cavity of the cell, different components of the DUT radiated fields are used to excite the TEM mode in the cell. Components of the radiated EM fields that do not couple to the fundamental mode of the cell quickly attenuate and will ideally not be measured. Thus, each orientation will give a measure of a component of the radiated power that couples to the TEM mode. Using many orientations allows all radiated components to be measured and by combining the data a measure of the TRP can be obtained. If one assumes that the DUT has dipole type radiation, then only three orthogonal axis orientations is required to obtain the TRP, but more complicated radiation patterns will require more orientations. Figure 1.2 shows a diagram and picture of a TEM Cell. These test structures are far less expensive than anechoic chambers and can be used from very low frequencies up to the cutoff frequency of the next highest order mode. However, the size of the DUT must not be so big as to interfere with the field uniformity. Additionally, larger TEM cells have lower cutoff frequencies for the higher order modes. This makes large objects difficult or impossible to test at high frequencies in TEM cells. For general information and theoretical
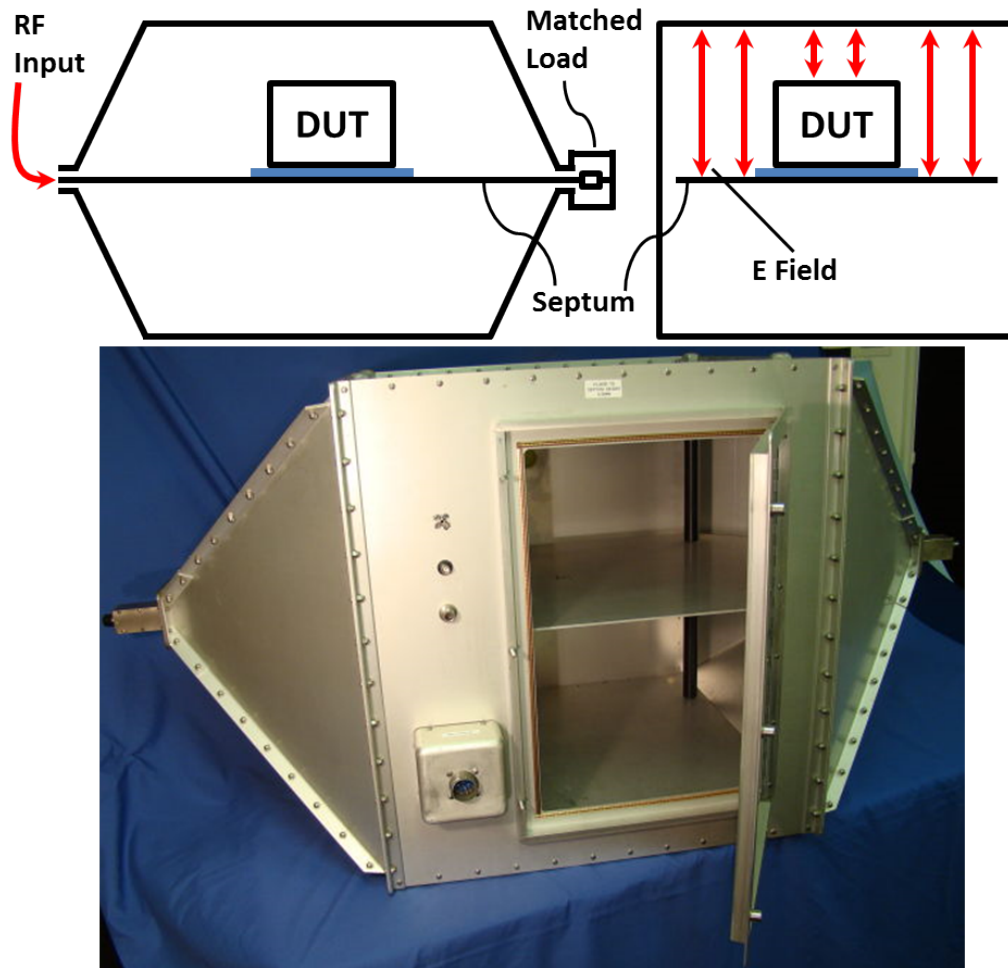
Figure 1.2: The lower picture shows an example of a TEM cell. The upper diagram shows how a DUT would be placed within the cavity of the cell. For immunity measurements a signal would be injected into the cell in order to determine the effects on the DUT.

development of TEM cell design see [5].

A reverberation chamber is an electrically large shielded metal room that, when operated at high enough frequency, permits the excitation of a large number of modes with closely proximate resonant frequencies. A diagram of an RC is shown in Figure 1.3. The mode density is the number of modes that can be excited per given bandwidth of frequencies. It is desirable to operate the RC at frequencies that have very high mode density. The field distribution of the excited modes creates locations of high and low field magnitudes called hot and cold spots, respectively. Measurements require that some method of relocating the hot and cold spots between measurement samples be implemented. This relocation of the mode field distributions (and to a lesser extent, the resonant frequencies) is termed mode mixing or stirring. For any stirring method, many samples are collected that are used to perform the statistical analysis. The statistical independence of each collected sample directly relates to the uncertainty of the statistical results. An effective stirring method will produce highly independent samples, or conversely, the collected samples will have low correlation.

If enough statistically independent samples can be obtained, then the average of the power measured at any location within the RC's working volume will be constant (within some standard deviation) and the RC is said to be spatially uniform [21]. Spatial uniformity of the RC allows measurements to be compared to models of a DUT subjected to incident EM fields from all directions and polarization angles. Conversely, the total field of a radiating source can be measured without moving the source itself. In addition, mode density increases with frequency, meaning that large objects can be tested at high frequencies so long as the DUT is still relatively small compared to the RC. While the DUT size is still a factor in the required size of the RC, generally it is the lowest desired operating frequency that drives the choice of how large the RC needs to be for a particular test. Conducting low frequency measurements in the tens of MHz range and lower requires building sized chambers that are very prohibitive for most potential users, and only a few of these facilities exist worldwide. However, above 1 GHz an RC can potentially be small enough to fit on a lab table. In addition, while these facilities are generally more expensive than TEM cells, they are

also still much less expensive than anechoic chambers. For a comparative review of EMC/EMI measurement methodologies in open test areas, anechoic chambers, TEM cells, and reverberation chambers see [41].

Selection of a measurement environment is not the only consideration to make when performing different EM radiation tests. The manner in which the data is collected may also differ for a single environment used for different types of measurements. Two approaches that can be taken in a given measurement environment are (1) to take measurements that are looking for mean values or (2) to look for the worst case. When characterizing the performance of an antenna or DUT, measured data is averaged in order to compare with analytic or numerical models. In this case, developers of wireless devices are often more interested in how the device performs on average. However, in Electromagnetic Compatibility (EMC) measurements, there is usually some maximum radiated field magnitude that developers must ensure the DUT does not exceed in its emissions, or must be able to withstand without error or damage. In these cases, rather than taking an average of the data, maximum field quantities are used to determine the DUT's field emission levels, or field immunity, relative to the field magnitude threshold.

While anechoic chambers, TEM Cells, and RCs have different properties from one another, they are often used to conduct the same types of measurements. For example, they each can be used to obtain the TRP from an EM radiating source. However, the manner in which one would obtain the TRP in each respective environment is very different. TRP measurements in anechoic chambers require the object under test to be rotated about its various axes in order to obtain the angle dependent radiation that can then be integrated over to obtain the TRP. In addition, the measured radiated power is only the component of the TRP that couples into the reference antenna used to take the measurements. Thus, in addition to rotating the test object, the reference must also be re-oriented to get the contributions at all polarization angles.

TEM Cell measurements of TRP are similar to those of anechoic chambers in that the test object must be rotated about its various axes to get the power radiated in all directions. However, in the TEM Cell the radiated energy must couple into the fundamental mode of the cell rather
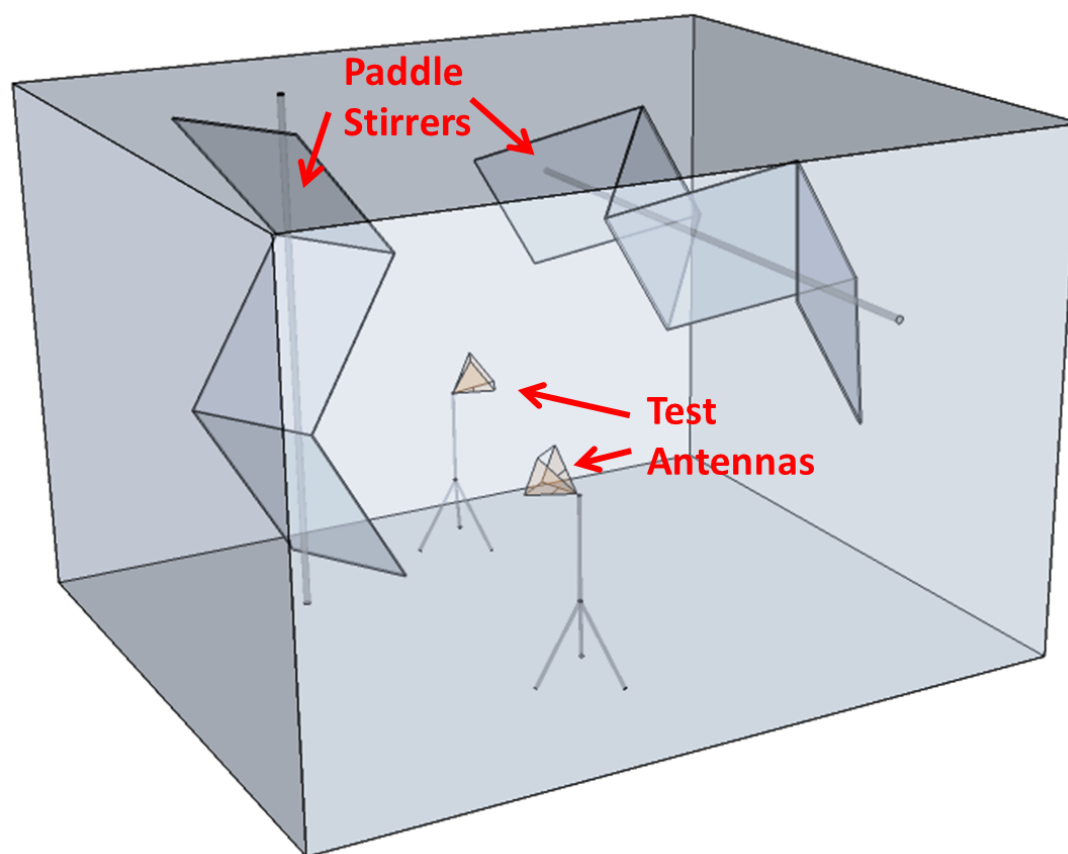
Figure 1.3: A diagram of an RC showing typical antenna placement, as well as paddle placement and shape. The paddles and test antennas are surrounded by metallic walls (shown transparently for visual aid).

than to a reference antenna, and the field of this mode cannot be reoriented. As a result, any EM radiation that does not couple into the fundamental mode will not be included in the TRP computation made from the measured data.
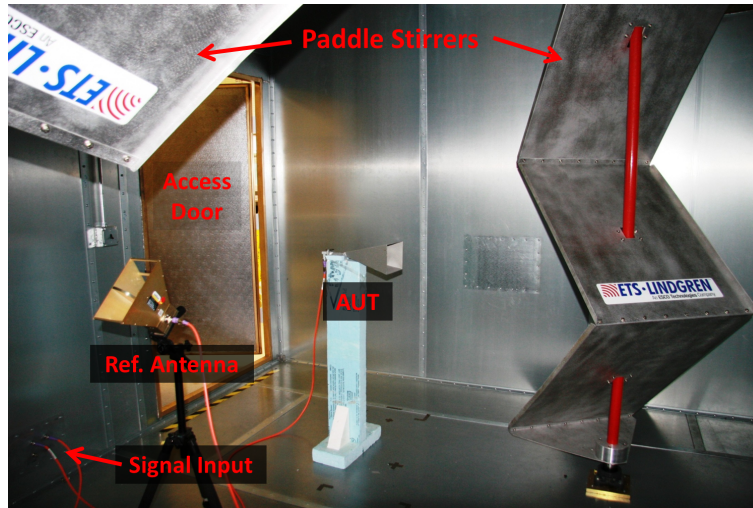
Figure 1.4: The 4.28 m width by 3.66 m depth by 2.9 m height NIST RC made primarily out of aluminum, featuring two independently rotating paddles. Also shown are two horn antennas, each faced at a different paddle: a wide band dual-ridged horn antenna used as a reference and an 8.2 to 12.4 GHz standard gain horn used as the AUT.

To measure TRP in the RC, many samples of the radiated power are taken as the fields within the cavity are stirred. Figure 1.4 shows a typical antenna measurement setup in the National Institute of Standards and Technology (NIST) 4.28 m x 3.66 m x 2.9 m RC. The desired TRP quantity is related to the mean of the measured powers over the collected stirred samples. One assumption that is made in making this statement is that the field of the RC is statistically uniform over its entire working volume, or in brief, that the RC is spatially uniform [21]. Spatial uniformity means that if a source and receiver are placed within the RC, the same mean power should be measured no matter where they are located. Two methods for stirring, or mixing, the mode distribution are commonly used in RC measurements: mechanical stirring and frequency stirring. Mechanical stirring can be further broken into many other types of stirring but all involve physically moving something within the chamber. Position stirring is similar to what is done in anechoic

chambers and TEM cells, with the addition that the object under test can also be displaced and not just reoriented. As an alternative, paddle stirring is often much more convenient because it requires no movement of the object under test. When paddle stirring is employed, a large irregularly shaped paddle is placed somewhere in the chamber. With no movement of the paddle there will be a distribution of high and low field magnitudes, called hot and cold spots, throughout the chamber cavity. The paddle is then turned either continuously or in steps in order to reorient the location of the hot and cold spots while measurements are taken.

Frequency stirring is used to achieve the same spatial uniformity in the RC, except that samples are taken by sweeping the source frequency over some narrow bandwidth, or window, of frequencies [38]. As the center frequency is changed the maximum and minimum field magnitudes of the EM modes spatially move around the chamber. The power measured at the various discrete frequency points within a window of frequencies are averaged just as paddle stirred data is averaged over all measured paddle positions. The average computed from the window of frequencies is then attributed to the center frequency in the window. Measurements over frequency are accomplished by sliding the same bandwidth window over a larger range of frequencies, as shown in Figure 1.5. Frequency stirring is similar to smoothing the data over frequency, with a few key differences. Frequency stirring must be applied to the raw measured (typically complex) data, while smoothing is generally applied to the final computation of the desired quantity. For example, S-parameters measurements collected with a network analyzer can be frequency stirred in order to obtain the average reflection coefficient and transfer function. These can potentially be used to compute the TRP of a DUT. Often the TRP results can have as much as 5 dB of variation, making it difficult to compare different measurement sets. In order to clean up the visual representation of the TRP results, the data can be smoothed using the sliding window method described above. In addition, different types of averaging windows can be chosen when smoothing final results, but frequency stirring is meant to be an un-weighted average just as other stirring methods are, so a rectangular window must be used. If the RC is spatially uniform, then the frequency and paddle stirring methods should give the same average power. However, perfect spatial uniformity is only a

characteristic of an idealized RC. Real RCs are never perfect and thus every computation of average power using the RC is always subject to some amount of error due to spatial dependence of the fields. In this case spatial dependence is defined as the variation of the average power measured at different locations within the RC. It is critically important to understand the spatial dependence of any RC being used because it directly relates to the uncertainty of all measurements conducted.

In a well-built chamber with good measurement equipment the dominant source of error in any RC measurement will be the spatial dependence of the fields [21]. Among other factors, the statistical analysis used in deriving EM field values of various kinds assumes that an infinite number of samples was used for calculation. This is of course never true and lack of samples is often a leading cause of measurement error. A related issue is the mode density at the frequency range being measured. When the mode density is very high, mixing techniques are generally more efficient in that the range of measured values needed for an unbiased average can be obtained with fewer measurement samples. Low mode density forces users to measure more samples in order to maintain low uncertainty, and if the density is too low unbiased averages may not be realizable. As a general rule of thumb, the mode density increases with frequency and decreases with increasing size of the DUT relative to the volume of the RC. Also, the idealized analysis makes the assumption that all of the measured samples are uncorrelated. However, real measurements will in general have some non-zero correlation between the various samples, which limits the resolution of all stirring methods. For example, paddle steps that are too short will be highly correlated, reducing the effectiveness of the stirring mechanism. Similarly, frequency stirring samples must be taken at a wide enough frequency step and bandwidth so as to not have highly correlated samples [50].

The use of position stirring may be confusing since spatial uniformity is the goal RC measurements strive for. The data that is desired is that which will give the same statistical field values as if the RC were truly spatially uniform. However, there are certain conditions in which spatial dependence within the RC is unavoidable, such as at low frequencies or when the DUT is large relative to the particular RC. In addition, no stirring method is perfect and using a combination of stirring techniques is useful in acquiring the number of statistically independent samples required
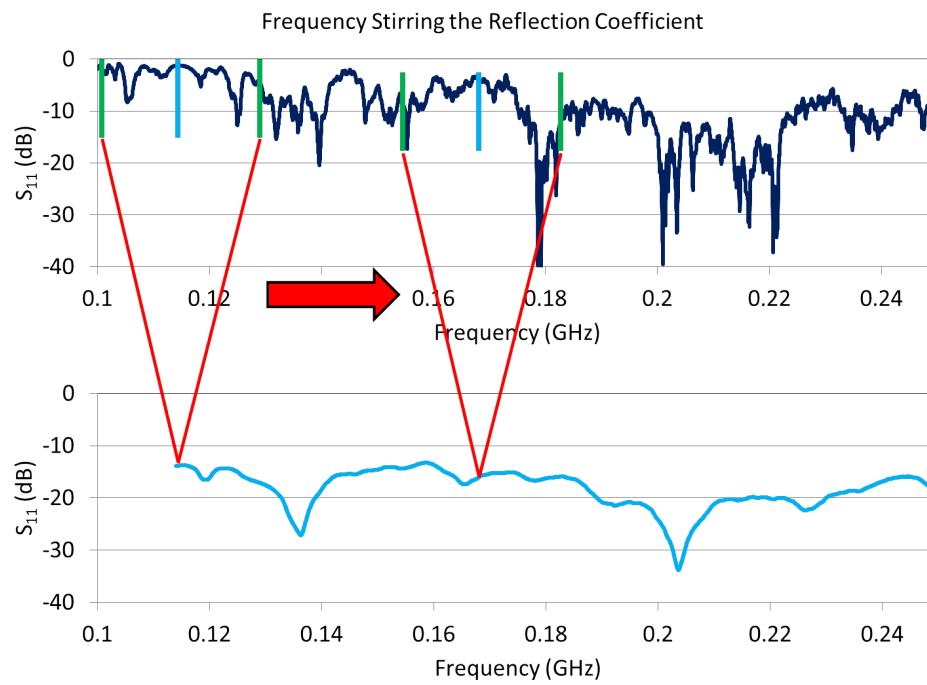
Figure 1.5: These plots show the effects of using frequency stirring to obtain statistical values of measured S-parameters. This process can be used to mix the raw measured data.

for unbiased data. In these cases taking samples with the DUT and/or reference at different locations can be used to help characterize and even correct for the spatial dependence of the RC and reduce statistical errors. In nearly all computations made from RC measurements, statistical analysis techniques are used whether they are completely valid or not. It is up to the test engineer to determine a stirring method, or combination of stirring methods, in order to keep the amount of statistical error low so that a high degree of confidence can be attributed to the statistically determined field values.

There are a number of different methods that can be used to characterize the spatial uniformity of the Reverberation Chamber. One is to plot the distribution of the measured data and compare them with the probability density functions (PDFs) predicted for an ideal chamber. Gaussian and Chi distributions of various degrees are typical for measured RC data [21]. While this technique is relatively easy to carry out, one must be careful when interpreting the results. The measured PDF of an antenna placed in a single position may approximate to the correct type of PDF obtained theoretically. However, it will still be important to take these measurements in multiple locations and compare the PDFs for each position to ensure that they are not only the correct type, but that there is little variation in their respective magnitudes and shapes when compared to one another.

A more straightforward method to obtain this same information is to instead just look at the variance of the measured data [34] as a function of antenna position in the RC. This technique is carried out by placing antennas at many positions within the RC and taking measurements, using, say, 100 paddle positions for each antenna position. Then the variance of the measured data is calculated for each position. With an overlay of the multiple variance plots the standard deviation of the data gives a measure of the spatial uniformity of the chamber. For an ideal chamber and an infinite number of measurement samples the measured standard deviation would be zero. In addition to using multiple locations for these spatial uniformity measurements, it will also be important to use multiple antenna polarization angles because each orthogonal antenna polarization will give a statistically independent sample with the antenna at the same physical location [34].

While these measurements have the potential of giving a very good characterization of the RC's spatial uniformity, they can also be difficult or impractical to perform.

The focus of this thesis is the evaluation of a different method for characterizing the spatial uniformity of the RC, using measurements of the enhanced backscatter coefficient. In EM, the term backscatter refers to the scattering of an EM wave towards the direction of the source. Enhanced backscatter refers to the phenomenon by which the sum of the scattered fields in the backscatter direction are larger in magnitude than the scattered fields in other directions. The factor of backscatter enhancement, termed the enhanced backscatter coefficient, is equal to the ratio of the average power at the source to the average power in other locations within the scattering space. The value of this coefficient is a topic of study in many fields including optics, acoustics, and remote sensing where it has been shown to have values ranging from slightly more than 1 to $(\frac{3}{2})^3$ depending on the type of wave, the dimension of the problem, and the randomness of the environment [7][62][42][36][31]. Under simplifying conditions on an ideal RC, defined later, using geometrical optics Dr. David A. Hill and others have shown that the enhanced backscatter coefficient in an electromagnetic RC approximates to 2 [21].
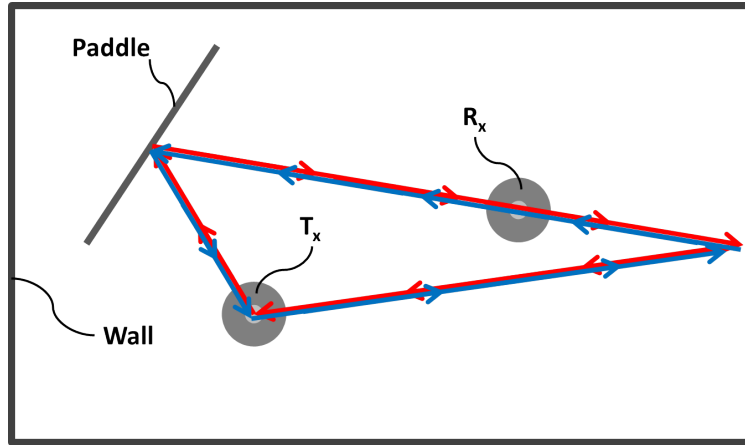
Figure 1.6: This diagram shows a greatly simplified model of a single time reversed pair of waves represented by rays in a rectangular cross section of an RC. At the source the waves add in phase. At other points along the path the waves add with a random phase difference.

Backscatter enhancement occurs in the reverberation chamber because forward and backward

waves following the same spatial path but in opposite directions add in phase at the source [59]. At other locations within the RC these time reversed pairs will not necessarily add in phase but will have some random phase and polarization shift between the pair. To illustrate this effect, a very simple ray trace diagram that shows the trajectory of a single time reverse pair is shown in Figure 1.6. As shown in the diagram, the two rays traverse the exact same path, reflecting off the same surfaces and traveling the same distance as they trace back to the transmitter. Assuming that the rays are radiated at the same instant in time and with the same polarization angle, the rays will add in phase and with the same polarization with respect to each other. However, if the two rays intersect at the same point somewhere else along their mutual trajectory, as the receiver is in the diagram, the rays will in general have a phase difference and polarization mismatch. The effect of this on the ensemble average of all stirred samples is that the mean stirred power measured at the transmitter will have a higher magnitude than the mean stirred power at other locations within the RC. Note that this diagram is merely to illustrate the enhanced backscatter phenomenon and is not representative of the truly complex nature of a real RC.

The value of the enhanced backscatter coefficient is dependent on the RC's spatial uniformity. In an RC measurement with well mixed data the enhanced backscatter coefficient has been observed to take on values that are close to 2. Deviations from this value are an indication that there is spatial dependence of the fields within the RC. This relationship allows the enhanced backscatter coefficient to be used as a metric for characterizing the spatial uniformity of the RC. It has been shown previously that measurements of the enhanced backscatter can give an idea of how well the RC is performing and if some change in the configuration has altered the spatial uniformity [15]. However, it would be more useful if these measurements could be used to directly determine the uncertainties in the measured data. As discussed previously with frequency stirring, EM fields vary with changes in frequency in an analogous manner to changes in position. Using this idea, observed changes in the enhanced backscatter coefficient over frequency can be used to estimate the error associated with spatial dependence in the measured data.

The primary goals of this thesis are twofold. First, it will be shown that the enhanced

backscatter coefficient can be used as a characteristic quantity that can be used as a benchmark to compute the spatial uniformity of the reverberation chamber. This is done by taking measurements with multiple RC configurations that consist of identical antennas placed in multiple locations and orientations. The spatial uniformity of the RC will be quantified as the relative uncertainty computed from the variation of the transfer function, and from the variation of the enhanced backscatter coefficient obtained from the multiple RC configurations. These two relative uncertainty estimates will be compared as a means of validating the use of the enhanced backscatter coefficient as an alternative and more complete estimate of the RC's spatial uniformity. Secondly, the enhanced backscatter coefficient is ideally flat over frequency, but in practice the value obtained has variation, and the mean value over frequency is fairly constant. It will be shown that the variation of the enhanced backscatter coefficient over frequency for a single RC configuration can be used to obtain an equivalent estimate of the uncertainty that is obtained using multiple configurations. By using the single configuration uncertainty estimate computed from the enhanced backscatter coefficient, the uncertainty of the quantities computed from the RC measurements can be estimated directly rather than having to rely on separate RC characterization measurements.

The next chapter gives an overview of Reverberation Chambers and discuses the important parameters and statistical properties that need to be considered in RC measurement and analysis. The third chapter looks at current techniques for characterizing the RC and shows some measured results. The fourth chapter goes into detail about the enhanced backscatter coefficient and how it can be used to characterize the spatial uniformity of the RC. The fifth chapter discusses the formulation and results of some simplified bounded source models for exploring the spatial dependence of the RC. The sixth chapter presents the complete analysis required to compute the total efficiency of an antenna from S-parameter data measured in the RC, and the uncertainty of the measurement is computed from the single configuration method.

Chapter 2

Important Parameters and Statistical Properties in Reverberation Chamber (RC) Measurements

In this chapter the parameters and statistical properties relevant to RC measurements will be given. In particular, focus shall be given to the measured parameters used in the analysis carried out in later chapters. The mathematical concepts and terminology required for later discussion will also be given.

2.1   Overview

Any electrically large cavity with highly conductive walls can be used as an RC. However, the desire for low leakage, low wall absorption, and low measurement uncertainty places other requirements on how an RC is constructed and used. Companies that build RC facilities take great care to ensure they have very low leakage when they are sealed. Leakage can not only effect the spatial uniformity of the RC, but in many EMC applications a DUT may need to be qualified to withstand incident fields of many thousands of volts per meter. The shielded RC environment is ideal for performing these tests because they provide an efficient environment for subjecting a DUT to very high field levels, as well as preventing harmful radiation from leaking out. The vast majority of RCs are made from highly conductive metals. This helps to make sealing them an easier task, and keeps the absorption of the walls low, which is important because wall absorption can distort the spatial uniformity of the RC.

In the past RC measurements were primarily performed using a signal/waveform generator

to inject a signal into the RC cavity, while a spectrum analyzer or power meter measures the signal. In modern RC facilities a vector network analyzer (VNA) offers an integrated measurement solution that is relatively fast and reliable. In addition, collecting vector scattering parameters (S-parameters) gives the possibility to correct for antenna mismatch. It should be noted that the measurement results shown in this thesis were taken using a VNA, and multiple antenna measurements with a VNA require that each antenna is used as both transmitter and receiver. However, for clarity discussions of measurements that contain multiple antennas will refer to transmit and receive antenna roles and functions.
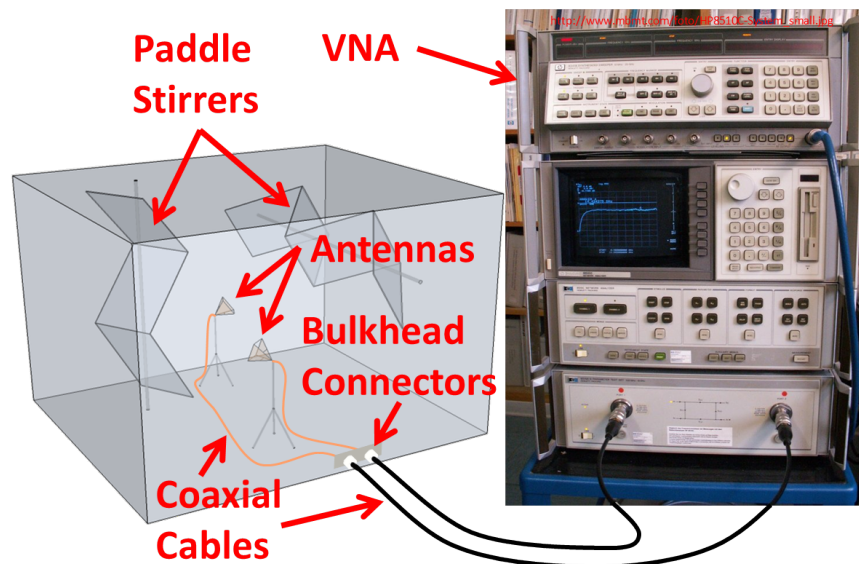
Figure 2.1: The connection path of 2 antennas placed in an RC to an externally placed VNA through bulkhead connectors.

In order to prevent the test equipment from biasing the measurements, antennas or field probes (electric or magnetic) are placed inside the RC and connected to the test equipment through cables and bulkheads attached to the RC wall, for example see Figure 2.1. For EMI measurements the antenna attached to the signal generator is replaced with a DUT to measure its output emissions. For EMC the DUT is illuminated by the injected signal to determine if the electronics are negatively affected. Some RC configurations may include a DUT and a reference receive antenna in order to

monitor the effects on the DUT as well as quantify the field that is incident on the DUT. The spatial uniformity of the RC means that the field incident on the DUT and reference antenna are, on average, the same [34].

The highly conductive surfaces inside the RC cavity create boundary conditions that the EM fields must satisfy. The shape of the cavity as well as the shape and placement of objects, such as antennas and paddles, determine the modal structure that exists. The measured field at any single point will be the summation of the cavity modes at that point. Since the RC is electrically large it can support a large number of simultaneously excited modes. Each mode is excited differently depending on how strongly the sourced field couples into it, and the fields established at a point are a combination of these modes. The complex nature of this multiple scattering environment means that while in reality the RC is deterministic, a full characterization of the fields at all points in the RC would be extremely difficult. In addition to this complexity, the pseudo random variation of measured field quantities motivates the use of statistical analysis techniques for analysis of data measured in an RC. The randomization of the fields is achieved by changing the boundary conditions that the fields must satisfy and, as previously mentioned, two common methods are paddle and frequency stirring.

In any EM measurement environment the amount of power transferred is subject to the various properties that make the particular environment unique. In any of these environments, field values computed from the measured results are obtained making various assumptions. These assumptions, if violated, can lead to significant error in the final computations. In anechoic chamber measurements the major assumption is that no reflection occurs at the boundaries. In TEM cells the assumption is that the DUT is subjected to a uniform field. Finally, in the RC the assumption is that the field is statistically uniform throughout the working volume. As will be shown for the RC case, there are several factors that contribute to non-uniformity of the average EM field in the RC, and it is important to characterize this deviation to assess the uncertainties in the measured results.

2.2 Electromagnetic Field Properties

The quantity that is used in many open environment EM tests is the power density (Poynting Vector). However, the Poynting Vector in an ideal RC would have a mean value of zero [21]. Thus, a quantity often used to characterize the field strength in RC measurements is the mean energy density. The time-average energy stored per unit volume of an EM field, as found in many common texts, is defined as:

$$W(\vec{r}) = \frac{1}{2} \left[\epsilon |\vec{E}(\vec{r})|^2 + \mu |\vec{H}(\vec{r})|^2 \right] \tag{2.1}$$

where $\vec{E}$ and $\vec{H}$ are the electric and magnetic field vectors, and ϵ and μ are the permittivity and permeability of the space that fills the RC cavity, which will be approximated as being the same as a vacuum. The vector $\vec{r}$ is the radial position vector in spherical coordinates with magnitude $\sqrt{x^2 + y^2 + z^2}$, defined using standard rectangular coordinates. If a source inside the RC is turned on, it will eventually fill up the cavity with energy until the input transmit power equals the power dissipated by the losses in the cavity [32]. Once this steady state condition is met, the energy density can be related to the steady state stored energy by [21]:

$$U = V \langle W \rangle \tag{2.2}$$

where V is the chamber volume, and $\langle \cdot \rangle$ denotes ensemble average and is defined by (A.10). A fundamental assumption that is made in RC measurements is that $\langle W \rangle$ is a constant throughout the working volume of the RC. Because of the statistical independence of the electric and magnetic fields [21][18] the average value of W can be found from:

$$\langle W(\vec{r}) \rangle = \frac{1}{2} \left[\epsilon \left\langle |\vec{E}(\vec{r})|^2 \right\rangle + \mu \left\langle |\vec{H}(\vec{r})|^2 \right\rangle \right] \tag{2.3}$$

where the statistical notation is explained in Appendix A.

An important parameter in RC characterization that is intrinsic to the cavity dimensions and wall loss is the Quality Factor, Q. A standard definition of Q is given by [43]:

$$Q = \frac{\omega U}{P_d} \tag{2.4}$$
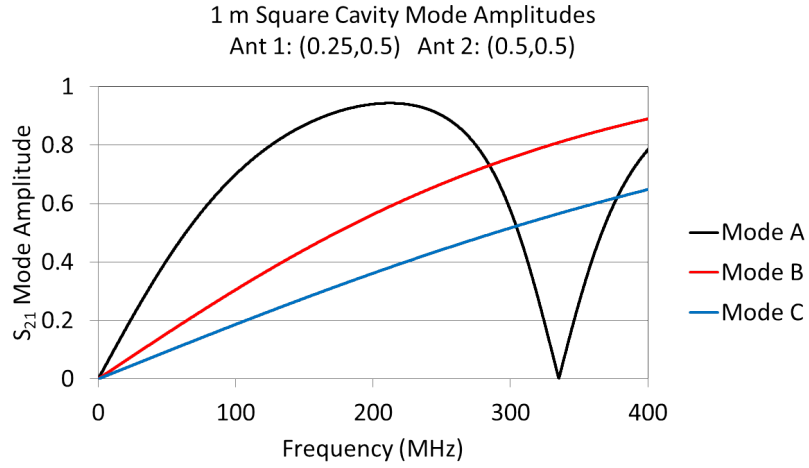
(a) Low Frequency Cavity Modes
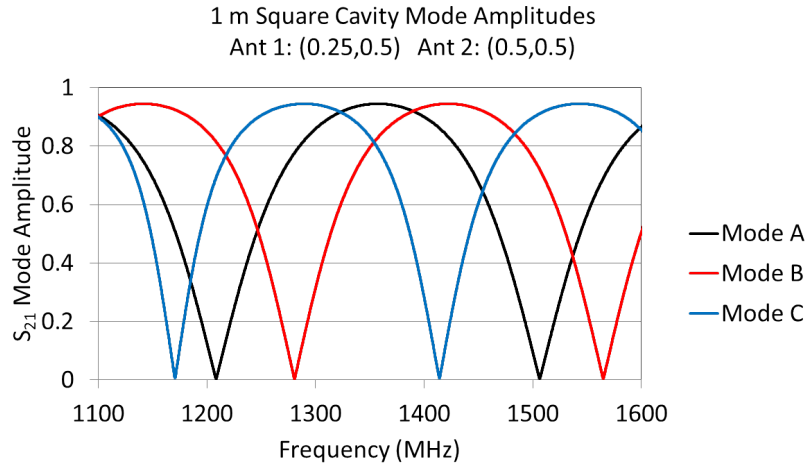
(b) Overlapping Cavity Modes

Figure 2.2: Plots of the S_{21} mode amplitudes for a 1 meter square cavity, with one source placed in the center and the other offset by 0.25 m from center. (a) Mode amplitudes from 10 kHz to 400 MHz. (b) Mode amplitudes from $1,100$ to $1,600$ MHz.

where ω is the angular frequency, and P_d is the power dissipated. For a single mode in a cavity this definition of Q is unambiguous and can be approximately related to resonant frequency f_r and the half-power bandwidth Δf by:

$$Q \approx \frac{f_r}{\Delta f} \qquad (2.5)$$

At low frequencies, where the RC cavity dimensions become small compared to a wavelength, single mode excitation dominates the response of the cavity. For example, Figure 2.2(a) shows the mode amplitudes at low frequencies for a two-dimensional 1 m square rectangular cavity. However, at higher frequencies many modes will be excited within a given bandwidth. As shown in Figure 2.2(b), losses in the chamber walls cause the modes to have overlapping half power bandwidths. The simultaneous excitation of many overlapping modes allows the stirring mechanisms to efficiently redistribute the mode amplitudes in the RC. In such a complex environment, determining the Q of the chamber based on the single mode definition is very difficult, if not impossible, because measurements over frequency result in plots of the envelope of the overlapping modes, which may constructively or destructively interfere in a complicated way. This has lead to the idea of a composite Q [8]. One method of defining a composite Q is to first relate it to the average power of the transmitter as:

$$Q = \frac{\omega U}{\langle P_T \rangle} \qquad (2.6)$$

where, as before, under steady state conditions $P_T = P_d$. Combining (2.2) and (2.6), Q becomes:

$$Q = \frac{\omega V \langle W \rangle}{\langle P_T \rangle} \qquad (2.7)$$

To write Q completely in terms of measurable and known quantities, $\langle W \rangle$ must be rewritten in terms of the average received power.

The average power at the receive antenna can be obtained by applying an infinite plane wave model of the fields inside the RC [22], described below in Section 2.3. Following this procedure with a linearly polarized antenna, the average received power obtained is:

$$\langle P_R \rangle = c \langle W \rangle \langle A_e \rangle \qquad (2.8)$$

where c is the speed of light in the cavity of the RC, and $\langle A_e \rangle$ is the effective area of the receive antenna averaged over all incident directions, given by:

$$\langle A_e \rangle = \frac{\lambda^2}{8\pi} \tag{2.9}$$

where λ is the wavelength. The average effective area is half the effective area of an isotropic radiator, the factor of $\frac{1}{2}$ coming in because of polarization mismatch. This result means that the pattern of the antenna is averaged over to give the same results as one polarization component of an isotropic radiator. Finally, combining (2.7), (2.8), and (2.9), the commonly used estimate of Q is obtained:

$$Q = \frac{\omega V}{c\lambda^2} \frac{\langle P_R \rangle}{\langle P_T \rangle} = C_{RC} \frac{\langle P_R \rangle}{\langle P_T \rangle} \tag{2.10}$$

where C_{RC} is the chamber relative size constant defined as:

$$C_{RC} = \frac{\omega V}{c\lambda^2} = \frac{16\pi^2 V}{\lambda^3} \tag{2.11}$$

The steady state assumption means this definition of Q is directly applicable for frequency domain measurements. Other formulations relate Q to the chamber's decay time constant using time domain data. It has been shown that these definitions can lead to different results [60][48][27]. The mechanisms that cause these differences is a current topic of research. The composite Q is assumed because it greatly simplifies calculations over large bandwidths. In reality, the composite Q is simply a (somehow weighted) combination of Q's that would otherwise need to be found from individual normal modes. The imprecision in defining Q in this way does in fact lead to an inherent uncertainty that is difficult to quantify in RC measurements.

2.3   Probability Density Functions

The PDF of the ensemble EM fields measured in RCs has received a considerable amount of attention over the years. A model for RC measurements that can be used to derive the EM field PDFs of an ideal RC is the infinite plane wave model defined as [13][21][30][61]:

$$\vec{E}(\vec{r}) = \lim_{N \to \infty} \frac{1}{\sqrt{N}} \sum_{n=1}^{N} \vec{A}_n e^{j\vec{k}_n \cdot \vec{r}} \tag{2.12}$$

where $\vec{A}_n$ are the vector amplitudes of the incident plane waves with various angles of incidence in the $\hat{k}$ direction, and $k = \omega\sqrt{\mu\epsilon}$. The basic idea of this model is that the field at any single point within the RC is assumed to be an infinite sum of plane waves incident from all directions and oriented with all polarization angles. This is a substantial assumption to make, but one that is shown to produce good agreement with measurements in EM and acoustics [34]. In addition, if the mode density is very high, then the mode description and the infinite plane wave description give equivalent results.

The results that can be derived from the infinite plane wave model, as reported in [18][6][63], is that the fields have the following statistical properties:

(1) The real and imaginary parts of the electric field components are statistically independent:

$$\rho_{E_x^{Re}, E_x^{Im}} = 0$$

where this property additionally applies to the y and z components of the electric field, and the definition of the correlation coefficient $\rho_{E_x^{Re}, E_x^{Im}}$ is given in Appendix A.

(2) The orthogonal components of the electric field are also statistically independent:

$$\rho_{E_x, E_y} = 0, \qquad \rho_{E_x, E_z} = 0, \qquad \rho_{E_y, E_z} = 0$$

(3) The previous two properties also apply to the real and imaginary parts, and the orthogonal components, of the magnetic field.

(4) The real and imaginary (in phase and quadrature) parts of the orthogonal field components have zero mean:

$$\mu_{E_x^{Re}} = 0, \qquad \mu_{E_x^{Im}} = 0$$

where this applies to the y and z components of the electric field as well as the components of the magnetic field.

(5) The real and imaginary parts of the field components are normally (Gaussian) distributed. For the real part of the x component of the electric field we have:

$$f_{E_x^{Re}} = \frac{1}{\sqrt{2\pi}\sigma_{E_x^{Re}}}e^{-\frac{(E_x^{Re})^2}{2\sigma_{E_x^{Re}}^2}} \tag{2.13}$$

where $\sigma_{E_x^{Re}}^2$ is the variance of E_x^{Re}, and the variance is defined in (A.11) of Appendix A. Similar expressions can be obtained for the real and imaginary parts of all orthogonal components of the electric and magnetic fields.

(6) The difference between the variance found for the real and imaginary parts of the components of the magnetic field verses that of the electric field is (shown for the real part of the x component):

$$\sigma_{H_x^{Re}}^2 = \frac{\sigma_{E_x^{Re}}^2}{\zeta^2}$$

where ζ is the intrinsic impedance of the RC cavity.
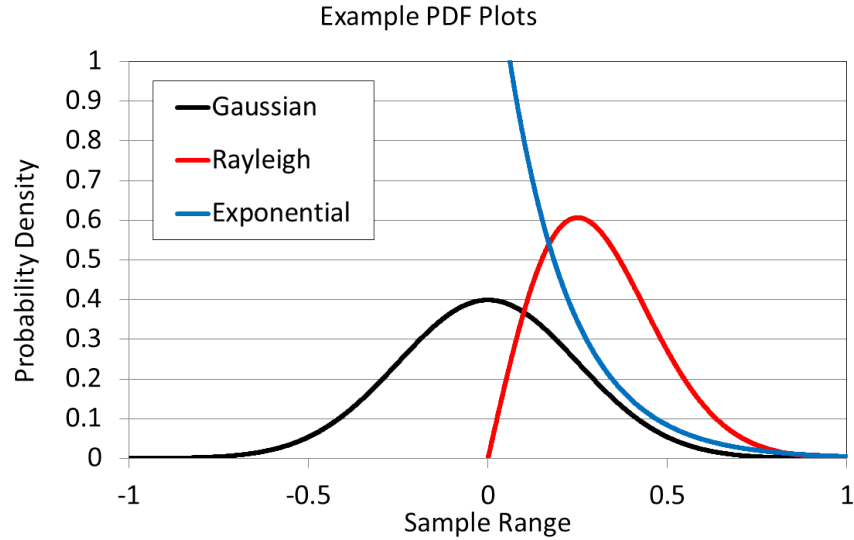
Figure 2.3: The shapes of the ideal Gaussian, Rayleigh, and Exponential PDFs.

The magnitude of a zero mean Gaussian random variable is a χ distribution with two degrees of freedom, which is a well known distribution named the Rayleigh distribution. This means that

the magnitude of any of the orthogonal field components is ideally Rayleigh distributed, so that for the x component of the electric field for example, we have:

$$f_{|E_x|} = \frac{|E_x|}{\sigma_{E_x}^2} \mathrm{e}^{-\frac{|E_x|^2}{2\sigma_{E_x}^2}} \tag{2.14}$$

where $\sigma_{E_x}^2$ is the variance of E_x, given by (A.11). The magnitude squared of a Gaussian distributed random variable is exponentially distributed given for the x component of the electric field as:

$$f_{|E_x|^2} = \frac{1}{2\sigma_{E_x}^2} \mathrm{e}^{-\frac{|E_x|^2}{2\sigma_{E_x}^2}} \tag{2.15}$$

Again, these distributions, (2.14) and (2.15), apply to all orthogonal components of the electric and magnetic fields. Plots of the ideal Gaussian, Rayleigh and Exponential probability densities are given for reference in Figure 2.3. In later chapters, these ideal PDFs will be used for comparison against measured data.

If the total mean field is required, then the combination of all six independent random variables that make up the real and imaginary parts of the three orthogonal field components, results in a χ distribution with six degrees of freedom. If the total power is required, the total mean field is squared resulting in a χ^2 distribution with six degrees of freedom. Expressions for these distributions can be found in [21].

In practice it is not usually required to measure all three orthogonal field components as long as the RC is statistically uniform [34]. Under this assumption, the statistics from the real and imaginary parts of a single field component give all of the information that is required. The total field can always be obtained by multiplying the results from a single component by 3. This reliance on the field uniformity assumption has potential for incurring large uncertainties in the computed results. Of particular concern are the effectiveness of the stirring method used and proximity of the antennas to the conducting boundaries in the RC.

2.3.1   Stirring

The various RC test cases that will be discussed and analyzed in later chapters will show how the computed results vary as different stirring methods are used. By paddle stirring, it is meant

that the method used to obtain different modal distributions between measurement samples is to turn either one or two paddles, as shown for example in Figure 1.3. If the paddle is stepped to N_1 different positions, and a measurement sample is collected at each paddle step, then the ensemble average, defined in (A.10), of S_{11} is:

$$\langle S_{11} \rangle = \frac{1}{N_1} \sum_{n=1}^{N_1} S_{11}(P_n) \tag{2.16}$$

where P_n denotes the paddle position that S_{11} was collected at. Instead of paddle positions the measured antennas could have been moved to N_2 different locations within the cavity of the RC. Now the ensemble average of S_{11} would be computed as:

$$\langle S_{11} \rangle = \frac{1}{N_2} \sum_{n=1}^{N_2} S_{11}(XY_n) \tag{2.17}$$

where XY_n is an antenna position that S_{11} was collected at. Another alternative would be that if it is determined that the measured antennas have a nearly constant response over some bandwidth of frequencies BW_1, then N_3 samples could be gathered within BW_1, this time making the ensemble average of S_{11}:

$$\langle S_{11} \rangle = \frac{1}{N_3} \sum_{n=1}^{N_3} S_{11}(f_n) \tag{2.18}$$

where f_n is a frequency at which S_{11} was collected, that lies within BW_1. It is often advantageous to mix stirring methods, which is typically done to simplify the collection of independent samples. For example, if the N_1 paddle positions were collected while sweeping the measurement device over frequency, then ensemble average computations can be performed using a double summation over the paddle, and frequency samples:

$$\langle S_{11} \rangle = \frac{1}{N_1 N_3} \sum_{n_1=1}^{N_1} \sum_{n_3=1}^{N_3} S_{11}(P_{n_1}, f_{n_3}) \tag{2.19}$$

This can similarly be applied for other combinations, which includes the combination of all three sample sets, requiring a triple sum. While there is a great deal of freedom of choice in the type of stirring method, or combination of methods, that can be employed for an RC measurement, the metrologist must ensure that samples collected meet certain criteria in order to be combined to give a single, unbiased average.

The infinite plane wave model of the chamber does little to explain the low frequency cutoff of the chamber. However, this cutoff can be obtained using the mode description of the RC. At low enough frequency, there is very little modal overlap, and the excitation of the chamber can be accurately described by considering the excitation of single modes. At higher frequencies the modes overlap and thus the excitation of the RC is a sum of multiple modes with varying contributions. This means there is a region of frequencies in which the RC transitions from being single mode resonant to being multi-mode reverberant. In acoustics this break point between a dominant single mode excitation and a multi-mode excitation is called the Schroeder frequency. Specifically, the Schroeder frequency is defined as the frequency in which the bandwidths of the modes are at least three times larger than their average frequency separation [55]. This definition gives a numerical low frequency cutoff by which to judge measured data, but it also varies depending on how the mode bandwidth is defined. This means that it can be specified to give a cutoff for a specific level of performance. In many acoustic studies, [29][53][39], the mode bandwidth is defined in the time domain to be the time it takes for the amplitude of the excited mode to drop by 60 dB. In the case of EM, the mode bandwidth is most often defined as the frequency domain 3 dB bandwidth, which is the change in frequency over which the mode amplitude is no less than 3 dB down from the center frequency amplitude.

The assumption that the fields measured at different paddle or antenna position are statistically independent is never actually true. In addition, frequency stirring samples must be collected with a large enough spacing to keep the samples from being highly correlated. An extremely useful model of the RC would be one that can take as input all of the chamber parameters: chamber dimensions, paddle dimensions, orientation and location, and material properties. At the output of this model one would obtain an upper bound on the correlation of samples taken at the different specified paddle positions and frequency points. To date this analysis has not been done, although conceptually it would be possible to do so, albeit with great computational difficulty. What has been looked at by many researchers is the correlation between measured samples in many different RC facilities [54][57][46]. For paddle and position stirring, what can be empirically concluded from

these studies is that the lowest correlation between samples is obtained when there are numerous irregularities in the geometry of the chamber. The same is also true for frequency stirring, in which the excitation of many modes within a specified bandwidth is supported by the existence of irregularities. In the absence of paddle movement, the rectangular RC has a high degree of symmetry which motivates the use of multiple stirring methods, particularly at low frequency. Irregularly shaped chambers are reported to have lower cutoff frequencies, and their potential use is currently under investigation [37][56][58].

RC measurements are based on statistical analysis and thus the uncertainties in computations made from the measurements always depend on the number of independent samples in the measured data set. The specific purpose of any stirring method used is to change the distribution of the excited fields, which is achieved by changing the boundary conditions, moving the source and/or receiver location, or switching the operating frequency. The fact that the RC is actually a deterministic system means that with nothing to force a change in the mode distribution, samples measured at different times will be highly correlated. Rotating the paddle, changing the source frequency, or moving the antennas are methods for de-correlating the measured samples. The effectiveness of the stirring method used will determine the amount of correlation between samples. A perfect stirring method would produce completely independent samples for every sample measured. Furthermore, when an RC measurement is said to be "well-stirred" it means that the correlation between samples is below some specified threshold.

2.3.2   Spatial Uniformity

Field computations made using the RC assume that the environment is statistically uniform, allowing the measured samples to be considered independent. This property is only approximately true, and then only in the region of the RC called the working volume. Thus, a simplistic definition for the working volume is the region of space in the RC which is statistically uniform within a certain degree of error. Therefore, the working volume is dependent on the intended application and the specified level of acceptable uncertainty. In terms of the fields, the working volume is the

space within the RC in which the fields can be well stirred. In addition, within the working volume the RC is said to be ergodic, termed this due to the observation that variation over space and frequency result in the same kind of field variations [54]. This means that the same PDF function will ideally be obtained if the variation is obtained over frequency, or with different spatial positions (including paddle position movement).

Inside the RC the highly conducting walls provide boundary conditions that can, for a single reflection, be modeled as perfectly conducting boundary conditions:

$$\hat{n} \times \vec{E} = 0$$

$$\hat{n} \cdot \mu \vec{H} = 0$$

Because of these boundary conditions, it is not possible to make the same assumptions if the antennas are near the walls, as are made with the antennas placed in the working volume. For example, the tangential electric field is zero at the walls but the normal electric field is not. Thus, if the antenna is near the wall, the assumption that the mean of the different orthogonal components of the EM fields are equal breaks down.
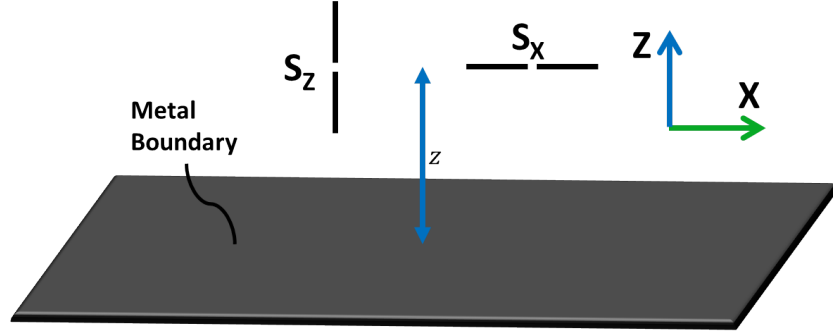
Figure 2.4: Geometry for variation of the EM fields for antennas near a conducting boundary.

One attempt to define a working volume based on the spatial correlation of a source near the RC boundaries was done by Hill in [21]. The geometry for a source placed near a single conducting boundary is shown in Figure 2.4. A source placed along the z-axis can be polarized in the $\hat{x}$ or $\hat{z}$ directions, leading to two distinct solutions. The spatial correlation functions for the $\hat{x}$ and $\hat{z}$

polarized sources are:

$$\rho_x(z) = \frac{3}{2}\left[\frac{\sin kz}{kz} - \frac{1}{(kz)^2}\left(\frac{\sin kz}{kz} - \cos kz\right)\right] \tag{2.20}$$

$$\rho_z(z) = \frac{3}{(kz)^2}\left[\frac{\sin kz}{kz} - \cos kz\right] \tag{2.21}$$

Rotational symmetry means that 2.20 is valid for any source polarized parallel to the boundary. The variation of the mean square EM fields with proximity to the conducting boundary can then be written in terms of the spatial correlation functions as:

$$\langle|E_x|^2\rangle = \langle|E_x^{WV}|^2\rangle\left(1 - \rho_x(2z)\right) \tag{2.22}$$

$$\langle|E_z|^2\rangle = \langle|E_z^{WV}|^2\rangle\left(1 + \rho_z(2z)\right) \tag{2.23}$$

$$\langle|H_x|^2\rangle = \frac{\langle|E_x^{WV}|^2\rangle}{\zeta^2}(1 + \rho_x(2z)) \tag{2.24}$$

$$\langle|H_z|^2\rangle = \frac{\langle|E_z^{WV}|^2\rangle}{\zeta^2}(1 - \rho_z(2z)) \tag{2.25}$$

where $\langle|E_x^{WV}|^2\rangle = \langle|E_z^{WV}|^2\rangle$ for large kz. Thus, it is required that $2kz \gg 1$ for the mean squared electric field to approximately equal $\langle|E_x^{WV}|^2\rangle$. The normalized variation of the mean square EM fields with proximity to the conducting boundary are shown in Figure 2.5.

The EM field variation for right angle edges and corners of the chamber also contains additional terms due to the sum of multiple images. However, the variation due to a single boundary decays the most slowly as the source is moved into the chamber volume [21]. One observation that can be made from Figure 2.5 is that the variation of the EM fields is greatly reduced when the distance from the boundary is greater than $\frac{\lambda}{2}$. In addition, these results were obtained assuming the boundary is a perfect electric conductor. The finite conductance of a real metal wall will further reduce the variation of the EM field magnitude. Based on this, the antennas placed in the chamber should be kept a minimum of $\frac{\lambda}{2}$ away from the walls. In practice, antennas are often placed further than this to additionally minimize the proximity affect of the conductive walls on the impedance of the antenna. With that said, there are techniques that take advantage of the presence of the walls by placing monopole elements on them using the wall itself as the ground plane. This was

done for measurements taken for [9] and [52] where the reference antennas were monopoles placed on the RC walls, giving more space for the DUT.
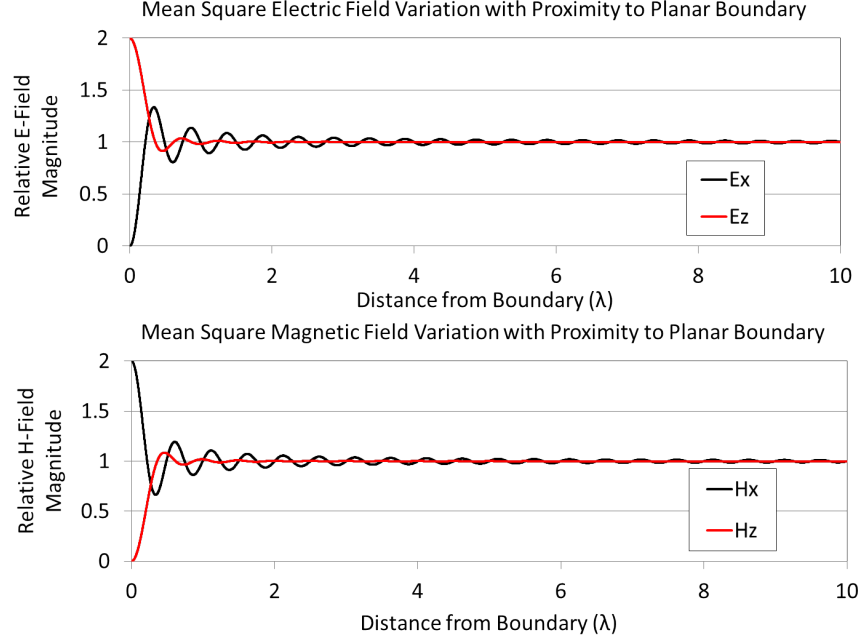
Figure 2.5: These plots show the variation of the mean square EM fields near a planar conducting boundary.

2.4   Antennas and Scattering Parameters

While there are many possibilities for how to take measurements in an RC, the data presented in following chapters were all taken using either an Agilent PNA-L or an Agilent PNA-X model VNA. Thus, in order to understand the S-parameters measured on the VNA, the power that exists inside the chamber must be related to the S-parameters that are measured on the VNA. To aid in this formulation, Figure 2.6 gives labels for the powers associated with an RC measurement in which antenna A is used as the transmitter and antenna B is the receiver. The power input to antenna A is P_1, the power reflected back to the source is P_3, and the power measured by the receiver is P_2. The power transmitted into the RC is P_{Tx}, the power reflected back to the transmit antenna is P_{rf}, and the power incident at the receiver is P_{Rx}.
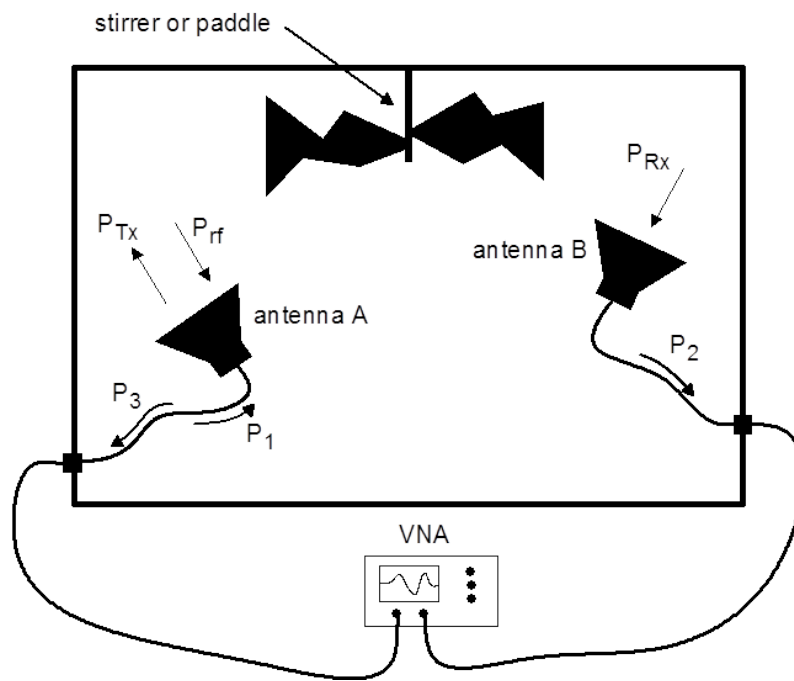
Figure 2.6: Flow of power out of and into two antennas in an RC measurement.

If statistical analysis analogous to that used for EM field and power measurements is going to be used for S-parameters, the different measurements must follow similar statistical distributions. Given a setup like that of Figure 2.6, S_{21} will be the transfer function of the component of the EM field that radiates into the RC from antenna A, and is received by antenna B [12]. The S-parameters and the EM fields are mutually dependent, but only by a non-linear functional relationship [47]. This means that in general there is no reason to expect that the electric field and the S-parameters have the exact same statistical distribution. In addition, the theoretical distributions of the EM fields in an RC have infinite bounds. However, power conservation arguments can be applied to show that the power of the EM field is bounded by the source power. Likewise, the real and imaginary parts of the S-parameters are bounded between ± 1. The differences between bounded and unbounded probability distributions are discussed in [45]. A key result from that study is that the theoretical variance, given by (A.5), and the measured variance (A.11), can give different results. The criteria for the theoretical and measured variances to be approximately equal is:

$$\sigma^2 \ll a^2 \tag{2.26}$$

where a is the upper bound of the truncated PDF. For the EM fields, a is the maximum field magnitude associated with the input power, and for S-parameters $a = 1$. Thus, the EM field and S-parameter distributions will only be analogous if the losses in the RC force two distributions to have very high probability of low values near 0. If this criteria is met, the PDF's of the EM fields and the S-parameters will be primarily concentrated around 0 and the error associated with the truncation at the upper limits will be small.

The S-parameter measurements will have low values when the wall losses of the RC dominate the overall loss observed in measurements. This may not be immediately obvious, primarily because as stated previously RCs are made from highly conductive metals. In addition, the antenna loss can still be thought of similarly to free space measurements in that it mostly appears as a single loss factor in the path of the signal. However, the loss of the RC walls only slightly decreases the signal for a single bounce. As time proceeds the signal reflects off the walls and other objects within

the RC. So, while a single wall reflection will reduce the signal amplitude by a very small amount, over many reflections the signal is significantly reduced, ideally decaying exponentially with time. It will be shown in Chapter 3 the measured S-parameter values in a well-behaved RC are primarily low, less than 0.2 in magnitude, which indicates that under certain conditions the S-parameters can be statistically analyzed in an analogous manner to the EM field components. One method to relate the EM fields in the RC to the corresponding S-parameters is to model the RC and antennas as a cascade of two port networks as done by Ladbury and Hill in [35]. A diagram of the cascaded network model for an RC with two antennas is shown in Figure 2.7.
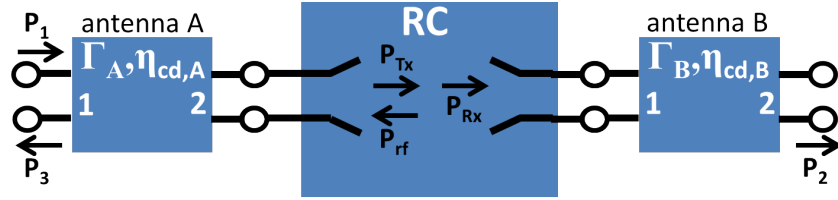
Figure 2.7: Cascade of 2-port networks used to model a two antenna RC measurement.

In a single, non-varying measurement sample (single frequency, no antenna position or paddle movement, and no time dependence) the fractional power transferred from antenna A to antenna B is given by:

$$|S_{21}|^2 = \frac{P_2}{P_1} \tag{2.27}$$

and the fractional power reflected back back from the feed of antenna A is:

$$|S_{11}|^2 = \frac{P_3}{P_1} \tag{2.28}$$

From this, the average transferred and reflected power fractions are:

$$\langle|S_{21}|^2\rangle = \frac{\langle P_2 \rangle}{\langle P_1 \rangle} \tag{2.29}$$

$$\langle|S_{11}|^2\rangle = \frac{\langle P_3 \rangle}{\langle P_1 \rangle} \tag{2.30}$$

The analysis used to formulate the statistics of an ideal RC assume that all of the power transferred to the receive antenna has been stirred. In fact, the infinite plane wave model (Sec-

tion 2.3) does not even include a transmit antenna. In real RC measurements there are line of sight (LOS) as well as specularly reflected signals that are transferred between the antennas and do not interact with the paddle. Thus, the S-parameters can be written as [25]:

$$S_{11} = S_{11,s} + S_{11,us} \tag{2.31}$$

$$S_{21} = S_{21,s} + S_{21,us} \tag{2.32}$$

where $S_{21,us}$ and $S_{11,us}$ are defined as:

$$S_{21,us} = \langle S_{21} \rangle \tag{2.33}$$

$$S_{11,us} = \langle S_{11} \rangle \tag{2.34}$$

These un-stirred components of the measured S-parameters result in a mean value that is not 0. The desired stirred component of the S-parameters for S_{21} is:

$$S_{21,s} = S_{21} - S_{21,us}$$

Given this the mean transferred power is:

$$\left\langle |S_{21,s}|^2 \right\rangle = \left\langle |S_{21} - S_{21,us}|^2 \right\rangle \triangleq \sigma_{S_{21}}^2 \tag{2.35}$$

and likewise for S_{11} we have:

$$\left\langle |S_{11,s}|^2 \right\rangle = \left\langle |S_{11} - S_{11,us}|^2 \right\rangle \triangleq \sigma_{S_{11}}^2 \tag{2.36}$$

Similar expressions can also be found when the roles of antennas A and B are reversed, but those will not be shown here. If mean un-stirred S-parameters are not zero, then the EM fields correspondingly are not zero. If the un-stirred portion of the fields does average to zero then (2.29) and (2.30) relate the S-parameters to the mean stirred power. However, if a non-zero mean un-stirred field exists, then these equations must be modified:

$$\sigma_{S_{21}}^2 = \frac{\langle P_2 \rangle}{\langle P_1 \rangle} \tag{2.37}$$

$$\sigma^2_{S_{11}} = \frac{\langle P_3 \rangle}{\langle P_1 \rangle} \tag{2.38}$$

If it can be assumed that the antennas are both perfectly matched and lossless then $P_1 = P_{Tx}$, $P_2 = P_{Rx}$, and $P_3 = P_{ref}$. Of course this is never true in reality, so additional terms must be used to relate P_1, P_2 and P_3 at the ports of the antennas to P_{Tx}, P_{Rx} and P_{rf} inside the RC. The full details of these derivations are given in Appendix B, and here only the main results will be shown.

The powers at the ports of the antennas and those inside the RC are related by the total efficiencies $\eta_{T,A}$ and $\eta_{T,B}$ of antenna A and B by:

$$\langle P_{Tx} \rangle = \eta_{T,A} \langle P_1 \rangle, \qquad \langle P_{Rx} \rangle = \frac{\langle P_2 \rangle}{\eta_{T,B}}, \qquad \langle P_{rf} \rangle = \frac{\langle P_3 \rangle}{\eta_{T,A}} \tag{2.39}$$

If the antenna is perfectly matched but has material losses we get (B.7):

$$\langle P_{Tx} \rangle = \eta_{cd,A} \langle P_1 \rangle, \qquad \langle P_{Rx} \rangle = \frac{\langle P_2 \rangle}{\eta_{cd,B}}, \qquad \langle P_{rf} \rangle = \frac{\langle P_3 \rangle}{\eta_{cd,A}}$$

If instead the antenna is made from perfect conductors and dielectrics, and noting that the reflection efficiency is expressed as $\eta_r = 1 - \Gamma^2$, then we get (B.23-B.25):

$$\langle P_{Tx} \rangle = (1 - \Gamma_A^2) \langle P_1 \rangle, \qquad \langle P_{Rx} \rangle = \frac{\langle P_2 \rangle}{1 - \Gamma_B^2}, \qquad \langle P_{rf} \rangle = \frac{\langle P_3 \rangle}{1 - \Gamma_A^2}$$

In order to compute the fractional powers inside the RC in terms of measured S-parameters, equation (2.39) is plugged into equations (2.37) and (2.38) to give:

$$\frac{\langle P_{Rx} \rangle}{\langle P_{Tx} \rangle} = \frac{\sigma^2_{S_{21}}}{\eta_{cd,A} \eta_{cd,B} (1 - |\langle S_{11} \rangle|^2)(1 - |\langle S_{22} \rangle|^2)} \tag{2.40}$$

$$\frac{\langle P_{rf} \rangle}{\langle P_{Tx} \rangle} = \frac{\sigma^2_{S_{11}}}{\eta^2_{cd,A} (1 - |\langle S_{11} \rangle|^2)^2} \tag{2.41}$$

If the direction of power flow is reversed, transmitting from Antenna B and receiving on Antenna A, the transmitted power equation (2.40) remains valid, but the reflected power measured by Antenna B is given by:

$$\frac{\langle P_{rf} \rangle}{\langle P_{Tx} \rangle} = \frac{\sigma^2_{S_{22}}}{\eta^2_{cd,B} (1 - |\langle S_{22} \rangle|^2)^2} \tag{2.42}$$

where the RC uniformity property was used when assuming that $\langle P_{rf} \rangle$ is the same for both antenna locations. This formulation was done using the S-parameters that would be measured in a 2-port
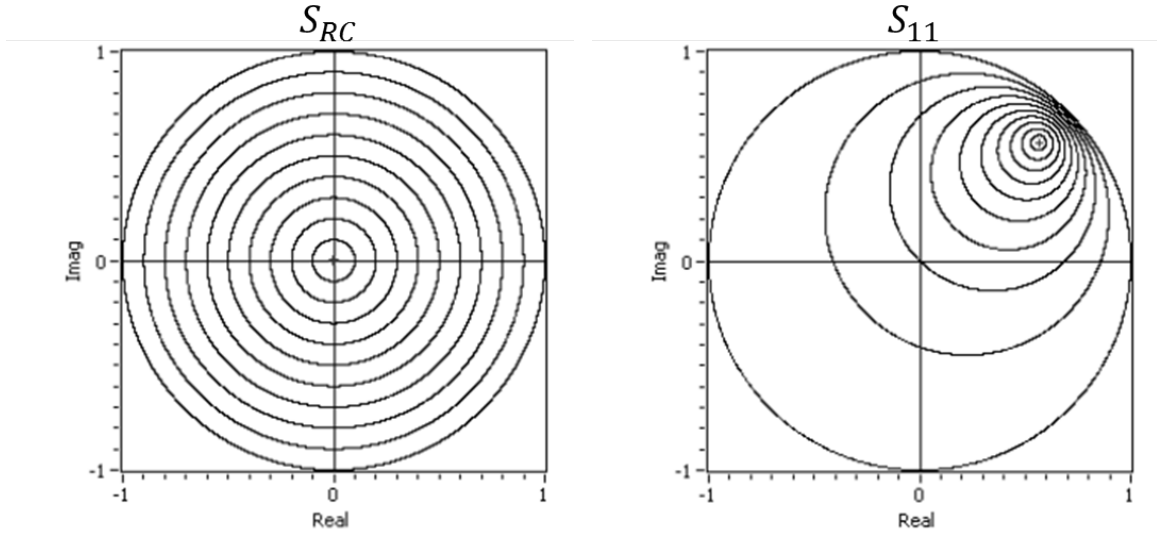
(a) Realizations of $\mathcal{S}_{RC}$, each with constant magnitude and uniform phase.

(b) Transformation of $\mathcal{S}_{RC}$ onto S_{11} plane.
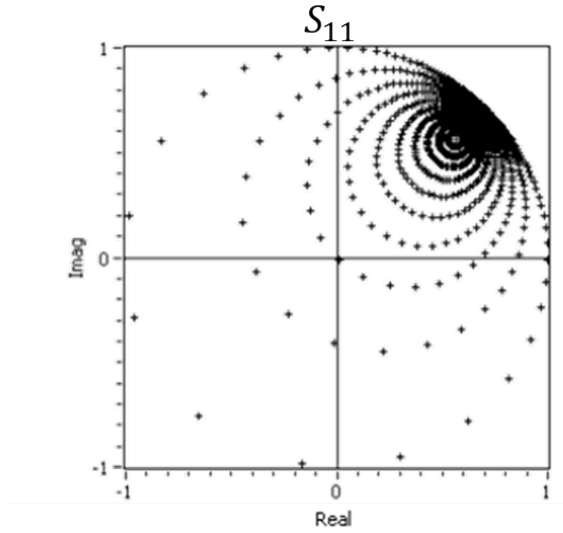
(c) Uniform samples of $\mathcal{S}_{RC}$ are distorted in the S_{11} plane.

Figure 2.8: These plots show how antenna reflection distorts the RC scattering parameter $\mathcal{S}_{RC}$.

measurement. In an N-port measurement where $N \rangle 2$ there will be N reflection measurements and the number of distinct transfer function measurements is given by $\frac{N(N-1)}{2}$. In later chapters, the designation $\sigma_{\mathcal{R}}^2$ will be used in order to discuss the variance of the reflection measurements without having to specify the port number. Also, the designation $\sigma_{\mathcal{T}}^2$ will be used to discuss the variance of the transfer function without having to specify a particular pair of ports.

It must be stressed that nearly all of the relationships in this chapter required the assumption that the measured data set contains a large number of independent samples. This is inherent in the assumption that the measured EM fields are realizations of a function of one or more random variables. As shown in (B.3), the solutions (2.40) and (2.41) require the assumption that the phase of the chamber reflection is uniformly distributed between 0 and 2π. While this is commonly done in in much of the published literature on RC measurement analysis, empirical observations are used to justify this assumption.

Limitations to the assumption of uniformly distributed phase is currently under investigation at NIST [35][11]. The plots in Figure 2.8 highlight some of the results from the work at NIST. Figure 2.8(a) is a plot of different realizations of the RC scattering parameter $\mathcal{S}_{RC}$, described at the top of Section B.3, each with a constant magnitude and uniformly distributed phase. If this reflection is measured using a real antenna that has loss, then S_{11} will be a modified version of $\mathcal{S}_{RC}$, as shown in 2.8(b). The amount of modification depends on the amount of antenna loss, and thus these measurements can be used to characterize the antenna's loss. However, if the stirring mechanism can be controlled such that $\mathcal{S}_{RC}$ is stepped uniformly, the measured reflection would look as shown in Figure 2.8(c). As shown, the majority of the points are clustered on one side of the plot, meaning that any mean values calculated using such data would be biased towards the clustered points. In real measurements the stirring mechanism is not so highly controlled as to discretely step the phase of the RC scattering parameter. As such, measured data is more randomized, but on average the clustered points in 2.8(c) are more likely to be the majority of the samples obtained in a measured data set. As a result, when chamber loss is low, and reflection is high, obtaining uncorrelated sample measurements becomes more difficult.

The issue caused by taking measurements with lossy antennas is addressed in [11]. In this work it is proposed that grouping data rather than taking the mean can be advantageous in some situations. In this context, grouping is done by plotting measured data on the complex plane, then the minimum radius bounding circle is computed from the complex data set, as is shown in Figure 2.9(c). In a typical measured data set, the center of the minimum radius bounding circle and the mean of the data will be approximately equal. This is the case with the data shown in Figure 2.9(a). If the antennas used in the RC are perfectly matched, then the mean of the reflection coefficient data, and correspondingly the center of the minimum radius bounding circle, would be zero. As reflection increases, the center of the circle approaches the $|\Gamma| = 1$ boundary. Two commonly encountered mechanisms that cause high reflection are: using poorly matched antennas, and placing the antennas too close to the chamber walls. In a case where the mean reflection coefficient is relatively high, such as that shown in Figure 2.9(c), the center of the minimum radius bounding circle and the mean of the data can be different. This difference is encountered because the minimum radius bounding circle extends outside of the unit circle of the complex plane. Correcting for mismatch with such high reflection often leads to errors because the measured values are small and precision is limited by noise. In other cases, differences between the center of the minimum radius bounding circle and the mean can be observed when the data is poorly sampled: too few samples or high correlation between samples. This issue can usually be solved by collecting more samples or using multiple stirring methods.

The other defining characteristic of the minimum radius bounding circle is the radius itself. One observation that has been made is that the radius of the circle drawn is related to the relative difference in the RC loss versus that of the antennas. The situation of Figure 2.9(b) shows the data being widely spread, which occurs when the chamber losses are relatively low, such as at low frequency. If the chamber loss dominates over the antenna loss, the measured reflection data set will tend to concentrate near the intrinsic reflection coefficient of the antenna. This method of grouping the measured S-parameter data has proven to be useful in estimating lower bound antenna efficiency using poorly matched antennas and is currently under investigation at NIST

with future publications in development.

2.5 Power Delay Profile and RMS Delay Spread

A communication channel can be modeled as a parallel combination of band limited linear filters [49]. For a multipath wireless channel, the filters would model the multiple paths taken by a signal before being added in parallel at the receiver. An impulse ideally has a flat spectrum at all frequencies, and thus the impulse response, $h(t,n)$ (where t is time and n is the stirred sample index), of the linear system provides the necessary information to characterize the frequency selective fading to which data transmitted through the channel is subjected. Fading occurs because the signals at the receiver arrive with different amplitudes and phases. This adversely affects the data transmitted through the channel, introducing symbol distortion and intersymbol interference and limiting the data rate that can be pushed through the channel [4]. One method of quantifying the frequency selective fading of a communications channel is to measure the Root Mean Squared Delay Spread τ_{RMS}. The Bit Error Rate (BER) of a DUT is the ratio of the number of received bits with error NB_e to the total number of received bits NB [17]:

$$BER = \frac{NB_e}{NB} \tag{2.43}$$

In addition to variation for channels with different τ_{RMS} values, the BER can also vary for different signal and modulation types, different antenna characteristics, and different receiver limitations [10]. Thus, the typical technique for measuring the BER is to place a DUT in its intended application environment that has a specific τ_{RMS}.

RF absorber material can be used to tune the RC to different τ_{RMS} values for purposes of measuring the BER of a DUT [19]. An RC with no RF absorber is a worst case wireless multipath channel. By adding RF absorber the RC can be tuned such that the τ_{RMS} obtained in the RC approximates the τ_{RMS} obtained in an intended environment for a wireless DUT. In doing so, the operation of the DUT can be tested in a more repeatable and controlled environment, but with similar multipath characteristics to the real world environment. Specifically, signals transmitted
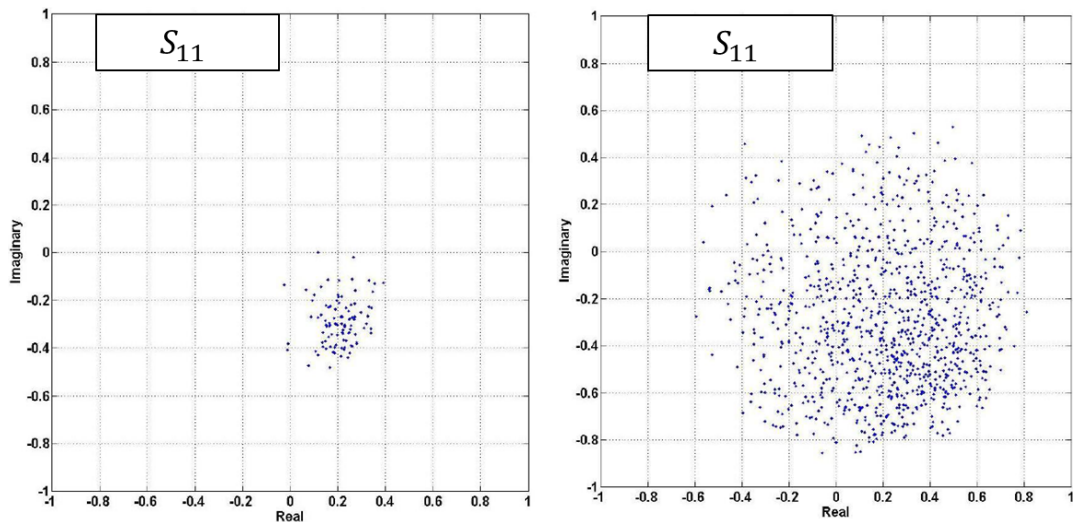
(a) Reflection from a typical RC measurement working under fairly good conditions.

(b) Reflection results from an RC being operated at low frequencies where the chamber losses are low.
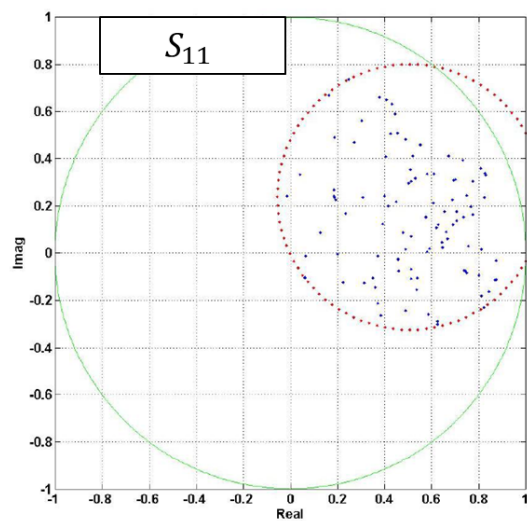
(c) Reflection results from an antenna placed near the wall of the chamber to increase the reflection seen at the input.

Figure 2.9: These plots show some different cases of RC reflection measurements.

in an RF absorber tuned RC are subjected to similar channel fading characteristics that would be experienced in the real world allowing for estimation of quantities like BER that are highly dependent on the multipath characteristics of the environment surrounding the DUT.

Formulation of τ_{RMS} begins with finding $h(t, n)$. In the following, the frequency domain method for computing $h(t, n)$ is shown, although there are also time domain methods for completing this task [49]. An ideal impulse is infinitely short in duration and contains all frequencies, which makes it impossible to ever truly measure the impulse response in either domain. However, the inverse Fourier transform of a swept sinusoidal source over a bandwidth of frequencies is equivalent to injecting a pulse with a finite time span. Impulse responses obtained in this manner are only valid over a specific frequency range and duration in time. In order to compute $h(t, n)$, the transfer function $\mathcal{T}(k, n)$, is measured in the frequency domain. The $\mathcal{T}(k, n)$ data set contains N_s measured samples, and n is the sample index ranging from 1 to N_s. Now, $h(t, n)$ is given as the Inverse Fourier Transform (IFT) of $\mathcal{T}(k, n)$:

$$h(t, n) = \frac{1}{N_f} \sum_{k=0}^{N_f - 1} \mathcal{T}(k, n) \mathrm{e}^{j \frac{2\pi k t}{N_f}} \tag{2.44}$$

where N_f is the total number of frequency points in the data set. The relative spacing of the measured frequency points will determine the duration of time, T_{total}, over which $h(t, n)$ can be computed, and the total bandwidth of the data will determine the size of the time step ΔT, where T_{total} and ΔT are given by:

$$\Delta T = \frac{1}{f_{max} - f_{min}} \tag{2.45}$$

$$T_{total} = (N_f - 1)\Delta T \tag{2.46}$$

and f_{min} and f_{max} are the minimum and maximum frequencies measured. In addition to the transfer function, $h(t, n)$ can be computed using reflection data, which will be applied to RC data in Chapters 3 and 4.

Typically, the multiple $h(t, n)$ samples are obtained by moving the DUT to different locations within a small area, around a room or building or a comparably sized outdoor space. In a changing environment, it may also be useful to take samples at different periods of time. Similarly, the RC

data may be collected with multiple DUT position and/or multiple paddle positions. A method for combining the affect of the multiple $h(t, n)$ samples collected is to compute the Power Delay Profile (PDP), given by:

$$PDP(t) = \left\langle |h(t, n)|^2 \right\rangle \tag{2.47}$$

where the ensemble average is performed over the multiple measurement samples to obtain a PDP that is just a function of time. The PDP is the average power of the multiply reflected waves that arrive at the receiver at different times. It is expected that at early times the PDP is made up of signals that took the most direct path to the receiver, and thus arrived first. Typically these initial peaks are the highest peaks obtained in the measurement. As time increases the arriving waves have traversed longer paths, reflecting and/or scattering from more objects before arriving at the receiver. Thus, after the initial peaks the PDP has a decay over time that is related to the increased path length and number of reflections undergone by the waves incident on the receiver. How the PDP decays is related to the specific environment. In environments dominated by multipath propagation, such as the RC at frequencies above cutoff, the PDP should decay exponentially [19]. A typical example of the PDP measured in the RC is shown in Figure 2.10.

Finally, τ_{RMS} is given by [19]:

$$\tau_{RMS} = \sqrt{\frac{\int_0^\infty (t - \tau_0)^2 PDP(t) dt}{\int_0^\infty PDP(t) dt}} \tag{2.48}$$

where τ_0 is the mean delay of the communications channel given by:

$$\tau_0 = \frac{\int_0^\infty t PDP(t) dt}{\int_0^\infty PDP(t) dt} \tag{2.49}$$

We can interpret τ_{RMS} as the time it takes for the PDP to decrease in power from the mean peak to $\frac{1}{e}$ down from the peak. As shown in Figure 2.10, the exponential decay of the PDP in the RC and other multipath environments typically results in a linear curve plotted on the dB scale. When the PDP decay can be approximated by a single exponential function then τ_{RMS} can be approximated by fitting a line to the linear portion of the curve obtained by plotting the PDP on a $\log_e$ scale, in which the early time peaks and late time aliasing have been removed. With this,
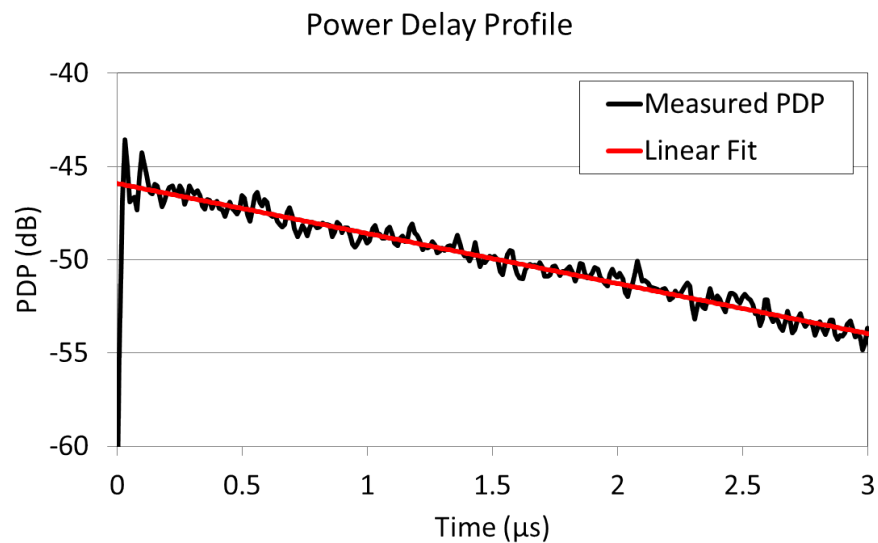
Figure 2.10: This plot shows an example of the PDP calculated from data measured in the large NIST RC with dimensions 4.28 m x 3.66 m x 2.9 m, using two antennas, a Log Periodic antenna and a Discone antenna. The data was processed over the frequency range f_{min} to f_{max} of 1.25 to 1.35 GHz.

τ_{RMS} is approximately given by [26]:

$$\tau_{RMS} \approx -\frac{1}{m} \tag{2.50}$$

where m is the slope of the curve fit line. This operation works well when the RC is well above its cutoff frequency. However, it will be shown in Chapter 3 that at low frequencies the PDP decay in the RC is not purely a single exponential, so the linear fit operation does not work as well.

2.6   Measurement Uncertainty

In Chapters 3 and 4 the relative uncertainty of the different methods will be compared. In each method many samples are obtained, either over different measurement configurations or over a bandwidth of frequencies. Following the formulation in [50], the standard deviation of different measurement samples P_n of a quantity P, gives the absolute measurement uncertainty $\hat{u}_P$ in P:

$$\hat{u}_P = \sqrt{\frac{1}{N-1} \sum_{n=1}^{N} \left[\langle P_n \rangle - \frac{1}{N} \sum_{n=1}^{N} \langle P_n \rangle \right]^2} \tag{2.51}$$

From this the relative measurement uncertainty $\hat{\tilde{u}}_P$ is defined as:

$$\hat{\tilde{u}}_P = \frac{\hat{u}_P}{\frac{1}{N} \sum_{n=1}^{N} \langle P_n \rangle} \tag{2.52}$$

This uncertainty estimation is not complete since it does not include effects due to the noise floor of the measurement system. However, with noise floor data not available for the results compared in the following chapters, (2.52) will be used to compare the different computational methods used for characterizing the RC.

The different methods used to characterize the RC will result in different values of $\hat{\tilde{u}}_P$ that are each an estimate of the relative measurement uncertainty. It is important to note that this formulation assumes that power is being measured, which is a positive real quantity making (2.52) an estimate of the relative uncertainty of positive real quantities computed from the measured data. The one-standard-deviation confidence interval of a positive real quantity, S^2 say, is computed by:

$$S_{CI}^2 = S^2 \pm \hat{\tilde{u}}_P S^2 \tag{2.53}$$

where the $+$ sign is used for the upper interval, and the $-$ sign is used for the lower interval of the computed positive real quantity. The confidence interval is an estimate of the error bounds that result from the use of statistical measurements to compute a deterministic quantity. For complete error bounds, noise and other contributions to measurement error, equipment repeatability for example, should also be included.

Chapter 3

Methods for Characterizing Spatial Uniformity of the RC

In this chapter two techniques for characterizing the spatial uniformity of the Reverberation Chamber will be presented. Characterization using comparisons of theoretical and measured Probability Density Functions will be shown first. While this technique can be useful, difficulties in processing the data and interpretation of the results make a more intuitive approach desirable. The second section presents an approach for characterizing the RC spatial uniformity which requires calculation of the variance of measured parameters at many locations throughout the RC. While the post processing of this technique is very straightforward, implementation of the measurement can be difficult at best and in some cases can be very impractical and would require unreasonable effort in order to obtain an unbiased measurement. The last section of this chapter discusses a method for tuning the RC using RF absorber foam to obtain a desired RMS delay spread.

3.1   Comparing Theoretical to Measured Probability Density Functions

If an RC is operated at high enough frequency with plenty of modal overlap and many independent samples can be obtained, the numerical PDFs found from the measured data should be very similar to those found using the infinite plane wave model. By the central limit theorem, the more independent samples that can be obtained in a measurement, the more the measured PDF will approach the analytic PDF. This simple concept can be used as a means of assessing how well the RC is operating. In other words, differences in the measured and analytic PDFs can be used as a relative indication of how well the RC is working.
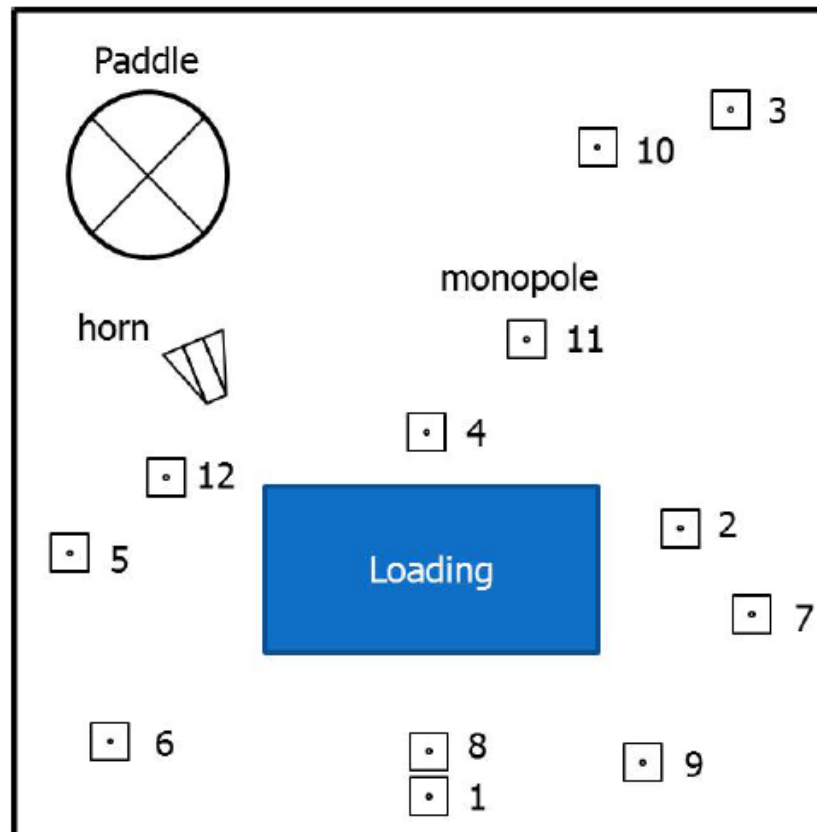
Figure 3.1: Relative placement of antennas, absorber material, and paddle stirrer used in Experiment 1 located in one of the large NIST RCs with dimensions 4.6 m x 3.1 m x 2.8 m (DxWxH).

Results from the experiment, described in the following and hereto referred as Experiment 1, will be used in this chapter and the next in order to make comparisons between the different methods for characterizing the RC. The original intent of Experiment 1 was to determine the change in spatial uniformity when relatively large devices are placed in the RC [57]. A diagram of this experiment is shown in Figure 3.1. The chamber used in Experiment 1 is one of the large NIST RCs with dimensions 4.6 m x 3.1 m x 2.8 m. This chamber has a single paddle that was stepped by 5° to 72 positions for each RC configuration. Samples were collected from 1.5 to 2.5 GHz, with 625 kHz frequency steps for a total of 1600 frequency points. As shown in Figure 3.1, 12 monopoles were placed in the RC at different positions and orientations. The first resonance of these monopoles is tuned to 1.9 GHz, and the elements are connected to a 20 cm x 20 cm ground plane. Also depicted in Figure 3.1 is a dual-ridged horn with aperture dimensions 13.5 cm x 22.5 cm. This horn antenna is used as the reference and the monopoles are each considered to be a separate AUT.
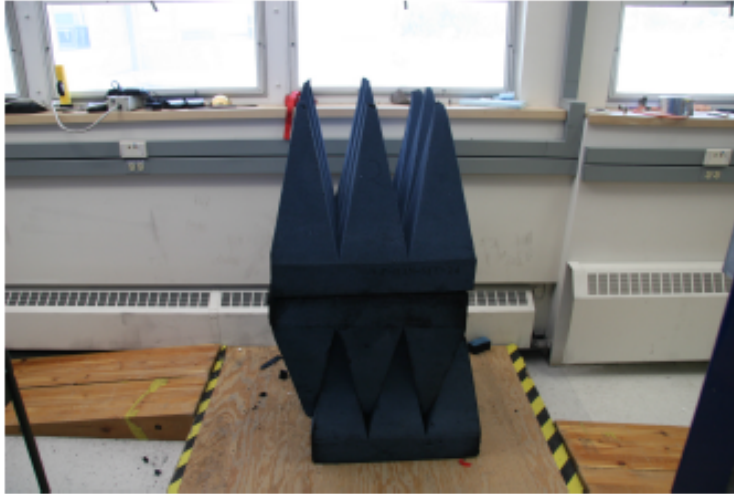
Figure 3.2: A stack of 3 RF pyramidal absorber blocks. This absorber was used to load the RC in Experiment 1.

The method used in [57] to quantify the changes in RC spatial uniformity is the standard deviation method that will be discussed in Section 3.2. The data in Experiment 1 was collected

using a 4-port Agilent PNA-L. The monopoles were measured in groups of three on ports 1, 2 and 3. The reference was measured on port 4 of the VNA for the four measurement runs needed to measure all twelve monopoles for each RC configuration. The spatial uniformity computation requires computing the variance of the measured transfer function between the AUT antennas and the reference antenna. With the reference antenna on port 4, this means that the variance of S_{14}, S_{24}, and S_{34} must be computed for each antenna group giving a total of 12 variance computations required for each unique chamber configuration. In reference to Figure 3.1 the antennas were grouped as:

- Group 1: Monopoles 1, 2, and 3

- Group 2: Monopoles 4, 5, and 6

- Group 3: Monopoles 7, 8, and 9

- Group 4: Monopoles 10, 11, and 12

The results that will be presented in this thesis used data from unloaded and absorber loaded configurations. By unloaded it is meant that the space in the RC cavity marked as "Loading" in Figure 3.1 is left empty. It can be argued that having so many antennas in the RC at once does in fact load the chamber as compared to just including one reference antenna and one AUT. However, since this configuration was maintained throughout the measurement campaign, comparisons can be made between the different configurations and different spatial uniformity computation methods, keeping in mind that the spatial uniformity may be different when fewer antennas are used. Typically, spatial uniformity measurements will consist of just two antennas that are moved to different positions and orientations for many iterations to get the different samples required. However, as stated previously the goal of Experiment 1 was to characterize the change in spatial uniformity as the chamber loading is changed, and thus it was highly desirable to leave the antennas in a fixed location for the duration of the measurement campaign. The loaded configurations results shown below consist of 2 to 4 Radio Frequency (RF) pyramidal absorber blocks. The blocks have

maximum dimensions of 0.6 m on all sides. A stack of 3 RF absorber blocks used in the measurements is shown in Figure 3.2. In the context of Experiment 1, the RF absorber blocks are used to characterize the effects of large DUTs made from lossy, non-metallic materials.

In addition to variance computations, the raw S-parameter data can also be used for other computations, such as PDF computations that will be shown below. Specifically, it is the measured transfer functions between each AUT and the reference horn that are used to compute the PDFs: S_{14}, S_{24}, and S_{34} for each monopole group 1 through 4. Before showing the measured PDF results, some of the concerns related to these computations should be discussed. As stated previously, there are several different stirring methods that can be used to conduct RC measurements. PDF computations can be made using data obtained from any valid stirring method, as well as from combinations of stirring methods. The method used for computing a PDF from RC data should be consistent with how averages are computed for the purposes of computing other quantities, such as received power or antenna reflection coefficient. This means that if paddles are used as the stirring mechanism, and averages are computed only over paddle position, then PDFs used for assessing the performance of the RC should correspondingly also be computed using samples obtained over paddle position. This means that although the data may have been collected over a range of frequencies, if frequency stirring was not used in computing averages, then the PDF computations should be made at single frequencies.

It is often highly advantageous to mix stirring methods, so one may decide that 100 frequency points will be averaged along with the 72 paddle positions. This means that 7200 measurement samples will be used to compute the PDF with. Care must be taken when doing this, especially given the resonant behavior of the monopoles. Since it is the chamber uniformity that is meant to be characterized in these measurements, computations should be made at frequencies in which the antennas have the best performance. Thus, PDF computations shown below consist of data taken at a center frequency of 1.9 GHz, the center resonant frequency of the monopoles. If it is specified that a range of frequencies was used for frequency stirring, the PDF was computed with the specified bandwidth centered at 1.9 GHz. Spatial averaging is another stirring method that
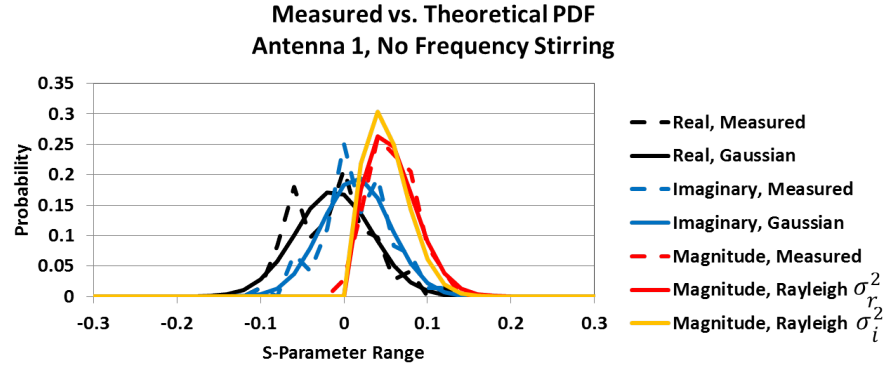
Figure 3.3: Experiment 1 measured and theoretical PDFs computed from S_{14} between antenna 1 and the reference horn, for the unloaded RC case and a single frequency at 1.9 GHz.

could potentially be used with this data set. If two positions are averaged and no frequency stirring is used, then 144 measurement samples would be used to compute the PDF. Lastly, in an attempt to see just how ideal the PDF can be made with a set of RC data as in Experiment 1, using a combination of paddle, position, and frequency stirring will be used, and hopefully give the best agreement between the measured and theoretical PDFs. In the following, comparisons will be made between the PDFs computed for these different stirring methods.

Typically an RC measurement consists of a single AUT and a reference antenna measured over many paddle positions. This is the baseline case, with the real, imaginary, and magnitude PDF results for the S-parameters shown in Figure 3.3, and theoretical curves for comparison. As shown, there is some qualitative similarity between the measured and theoretical curves. However, the quantitative deviations may be larger than what is acceptable for a specific application. Since it was observed that a single antenna position, using no frequency stirring, and 72 paddle positions gives less than desirable PDF curves, Figures 3.4(a), 3.4(b) and 3.4(c) were created to observe how different combinations of antenna positions and frequency stirring affect the PDF curves. Shown in these figures are PDF curves for the real part of the measured transfer functions, so ideally they will have a Gaussian shape.

To verify that the PDF obtained for AUT 1 is similar to that of other antennas Figure 3.4(a) shows similar PDFs calculated for all of the antennas in Group 1. In addition, the PDF computed from the transfer function data for all three antennas is also shown. This combination of data is representative of measurements consisting of 72 paddle positions with 3 spatial positions giving a total of 216 measurement samples, again keeping in mind that typically spatial averaging is done by moving a pair of antennas to 3 locations. As shown, the Group 1 PDF is improved as compared with single position PDF computations, but it still looks choppy as compared with a smooth Gaussian curve.

Considering that Group 1 was measured separately from the other groups, one may wonder if the PDF curves for one group are similar to that of other groups. The curves shown in Figure 3.4(b) are similar to those of Group 1 shown in Figure 3.4(a) for all of the groups. Similarly to what was
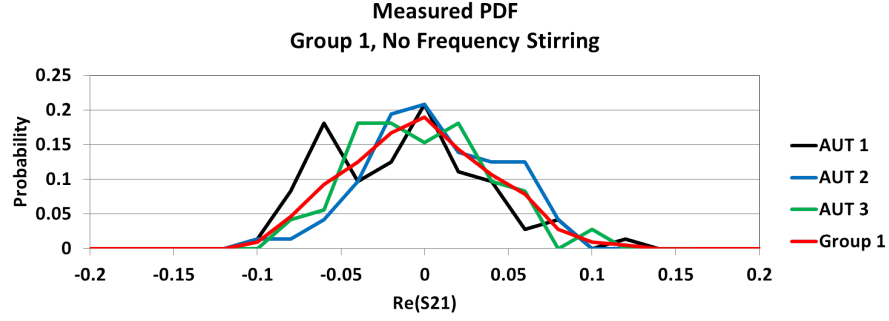
(a) Individual group 1 antennas and all of group 1 together, for a single frequency at 1.9 GHz.
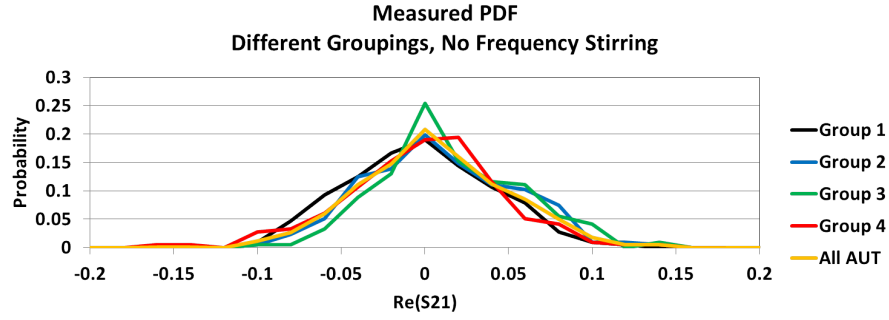
(b) Each antenna group and all AUTs together, for a single frequency at 1.9 GHz.
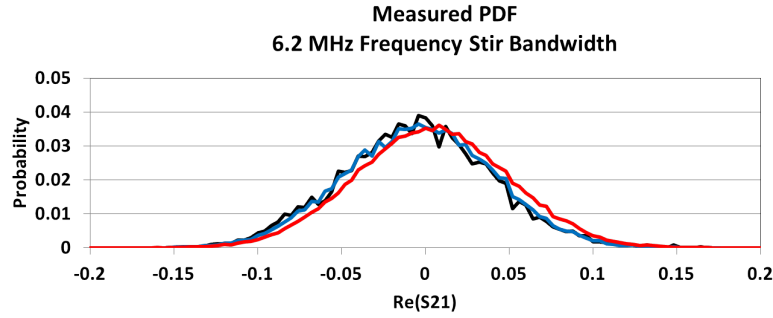
(c) Antenna 1, group 1, and all AUTs together, for a center frequency of 1.9 GHz and a 6.2 MHz frequency stirring bandwidth.

Figure 3.4: Comparison plots of PDFs computed from measured transfer functions for the Experiment 1 unloaded cases and different data groupings, with and without frequency stirring.

done in Figure 3.4(a), the combination of the data from all 12 antenna positions is also shown. With 72 paddle positions and 12 antenna positions, 864 measurement samples are used in the PDF computation. As shown, improvement is once again obtained by adding additional antenna positions to the computed PDF curve.
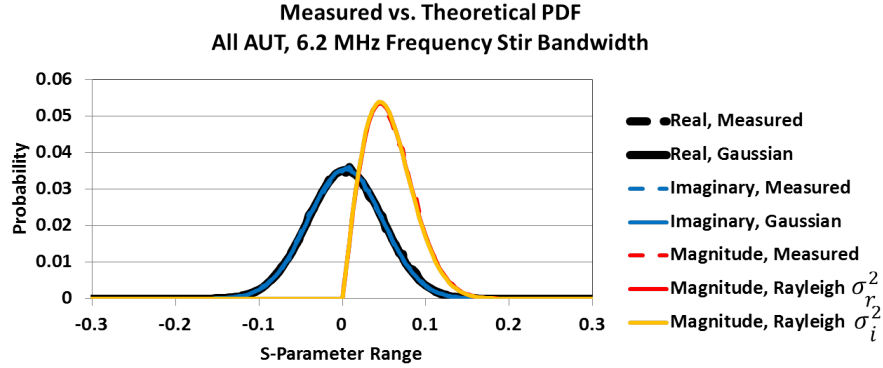
Figure 3.5: Plots from Experiment 1 comparing measured and theoretical PDF curves computed from S_{14} between antenna 1 and the reference horn, for the unloaded RC case, all AUTs together, a center frequency of 1.9 GHz and a 6.2 MHz frequency stirring bandwidth.

In addition to antenna position stirring, frequency stirring can potentially provide another means of improving the PDF curves. The curves shown in Figure 3.4(c) compare PDFs obtained using 100 frequency points, a bandwidth of 6.2 MHz. This is done for data from Antenna 1, Group 1, and all 12 of the monopoles. As shown, 100 frequency samples in combination with the 72 paddle position greatly improves the PDF computed with AUT 1 data. Adding multiple antenna positions again further improves how smooth the PDF curves are. Using the combination of 72 paddle positions, 12 antenna positions, and 100 frequency samples gives a total of 86,400 measurement samples for the PDF computation. The curves in Figure 3.5 show the measured and theoretical PDFs for this combination of stirring methods. As shown, the agreement with the measured and theoretical PDF curves is very good. What can be observed from these different plots is that the agreement between measurement and theory is highly dependent on the number of independent samples used for computations. This agrees with statements made in [50] that the uncertainty in

the RC is a function of the number of independent samples and is ideally given by:

$$u_{LB} = \frac{1}{\sqrt{N_{ind}}} \tag{3.1}$$

where N_{ind} is the number of independent samples in a data set, and u_{LB} is the lower bound uncertainty for any RC measurement (as well as any other statistical measurement). The actual uncertainty and the lower bound will be equal if all of the measurement samples have zero correlation.

Measured PDF curves give an indication of how well the RC is working. If the measured PDF curves closely match their theoretical counterparts it is said the RC is behaving as expected. Figure 3.6 shows how the measured PDF curves vary with increasing number of absorbers, for paddle, position, and frequency stirring combinations used to obtain Figure 3.5. As shown, the measured PDF becomes more concentrated near 0, which indicates that the absorber is decreasing the magnitude of the average received power. Also, the curves plotted for the absorber loaded cases appear to be less smooth than the unloaded case, indicating that the absorber has had an effect on the spatial uniformity of the RC. What would be desirable is to be able to compute the difference between the measured and theoretical PDFs and relate the difference to the uncertainty of the RC. However, it is not immediately obvious how to relate differences in the PDFs to the uncertainty of the RC. In addition, the PDFs shown for Experiment 1 were done for 3 different frequencies. A good RC characterization would require these plots to be made at many different frequency points throughout the measured band of frequencies a tedious task at best. In Section 3.2, a different method for characterizing the RC will be discussed, that is computationally more straightforward and easier to apply over large frequency bands. The effects of antenna position, frequency stirring, mismatch correction, and absorber loading will be observed in terms of the uncertainty of the RC measurement.

PDF for Different Chamber Loading
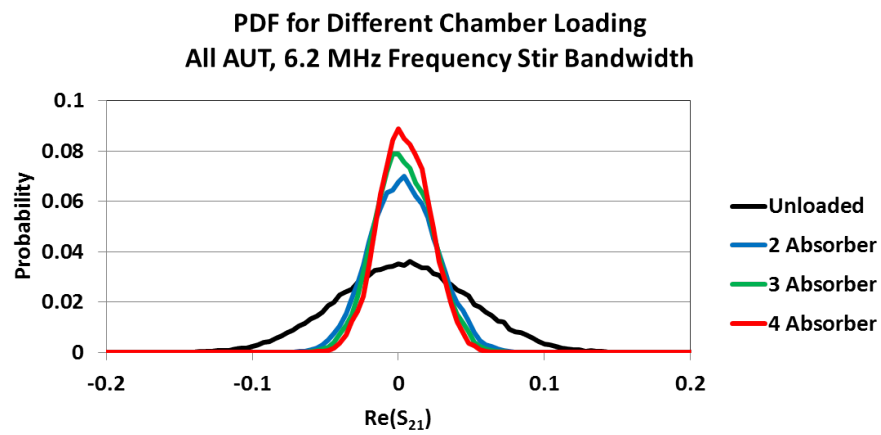**All AUT, 6.2 MHz Frequency Stir Bandwidth**

Figure 3.6: Measured PDFs for different amounts of absorber loading placed in the RC, for all AUTs together, a center frequency of 1.9 GHz, and a 6.2 MHz frequency stirring bandwidth.

3.2 Standard Deviation of Measured Data Over Many Antenna Positions

For purposes of characterizing the RC, a more computationally intuitive measurement to perform is to simply calculate the variance of the measured parameters at many different locations and orientations in the RC working volume. If a VNA is used to take measurements then it will be the measured S-parameters that will be used for uncertainty computations. However, if other devices are used for measurement then it will be the measured field or power quantities that would be used for the uncertainty computations. If the RC has perfect spatial uniformity, and an infinite number of independent samples can be taken, the variance at every location will be exactly the same. Thus, a measure of the spatial dependence in the measured data is the spread of the variances measured at multiple locations. From (2.52) the spread of the variances is the standard deviation, and presently the measured data for comparison at multiple locations is the transfer function $\sigma^2_{\mathcal{T}n}$. Later, similar analysis will be applied to the enhanced backscatter coefficient computed from the same data set for comparison.

It is important to keep clear the difference between the two measures of spread. From (2.40) we have that the variance of the transfer function, $\sigma^2_{\mathcal{T}}$, is proportional to the transmitted power. This is measured at multiple locations giving N different $\sigma^2_{\mathcal{T}n}$, where n is 1 to N and N is the number of antenna measurement positions. The relative uncertainty $\hat{\hat{u}}_{\sigma^2_{\mathcal{T}}}$ is a relative measure of the spread of the $\sigma^2_{\mathcal{T}}$ results obtained at the multiple locations, giving a measure of the spatial uniformity. A perfectly uniform RC would give a value of 0 for $\hat{\hat{u}}_{\sigma^2_{\mathcal{T}}}$. In the following, the $\sigma^2_{\mathcal{T}n}$ results from Experiment 1 will be shown. Since noise floor measurement data is not available for the Experiment 1 data set, (2.52) will be used to compare the variance and enhanced backscatter methods, shown in Chapter 4, for estimating the relative uncertainty of the RC.

For the data from Experiment 1, $\sigma^2_{\mathcal{T}n}$ is computed from S_{14}, S_{24}, and S_{34} for each measurement set and RC configuration. The $\sigma^2_{\mathcal{T}n}$ results from Experiment 1 are shown in Figure 3.7. The RC configurations shown in each plot are the unloaded, 2 absorber loaded, and 4 absorber loaded. For clarity, only the results from Group 1 are shown. The $\sigma^2_{\mathcal{T}n}$ results shown in Figure 3.7(a)

were computed using paddle stirring only, and are not corrected for mismatch. The results in Figure 3.7(b) are the same measurements as in Figure 3.7(a) with mismatch correction applied. Lastly, Figure 3.7(c) again shows the same data, but with a 6.2 MHz frequency stirring bandwidth, as well as mismatch correction, applied.

A general trend that is easily observed in the three plots shown in Figure 3.7 is that adding absorber decreases the power transmitted in the RC, which is an expected result. In addition, comparing Figures 3.7(a) and 3.7(b), shows that mismatch correction causes power to decrease linearly on a logarithmic scale, which has also been shown to be true for typical RC measurements [34]. In addition, comparing Figures 3.7(b) and 3.7(c), it can be observed that the spread of $\sigma^2_{\mathcal{T}n}$ decreases when frequency stirring is used, which should be expected as the number of independent samples used for each $\sigma^2_{\mathcal{T}n}$ computation is increased. What is also evident from Figure 3.7(c) is that frequency stirring decreased the spread of $\sigma^2_{\mathcal{T}n}$ data more for the unloaded case than the absorber loaded cases.

In order to compare the relative effects of the absorber, mismatch correction, and frequency stirring in the various cases, the data shown in Figure 3.7 can be inserted into (2.52) to obtain $\hat{\bar{u}}_{\sigma^2_{\mathcal{T}}}$, the estimated measurement uncertainty for each case. The results are shown in Figure 3.8. The slight difference between the lower frequency parts of Figures 3.8(a) and 3.8(b) shows that mismatch correction had little effect on the uncertainty estimate of the measured power for Experiment 1. This is the expected result in a typical measurement because the same two antennas are moved to different locations, meaning that the mismatch correction should ideally be the same for each position, with possible differences due to cable movement and the wall distance to each antenna. In this case however, twelve monopoles and a dual-ridged horn were used in the measurement. Variations in the construction of the monopoles have the potential for giving very different mismatch corrections for each antenna position. However, Figures 3.8(a) and 3.8(b) show that the differences between the antennas is small and most evident at low frequencies.

The variance results shown in Figure 3.7(c) suggest that frequency averaging decreases the spread of $\sigma^2_{\mathcal{T}n}$ at the different positions much more for the unloaded case than for the 2 and 4
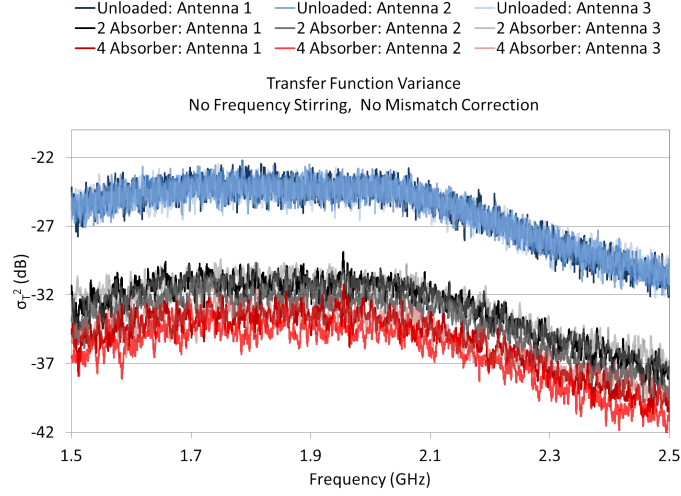
(a) No frequency stirring and no mismatch correction.
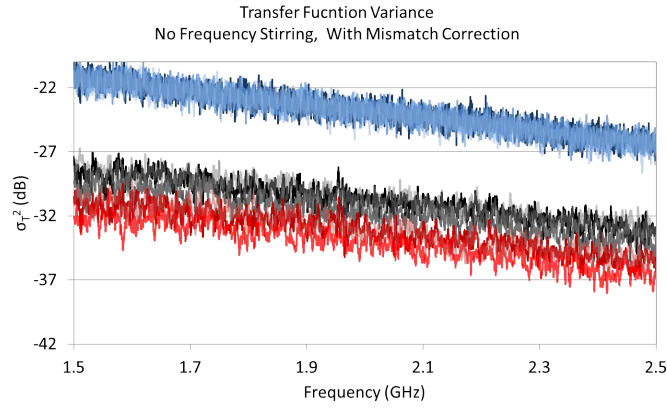
(b) No frequency stirring, with mismatch correction.
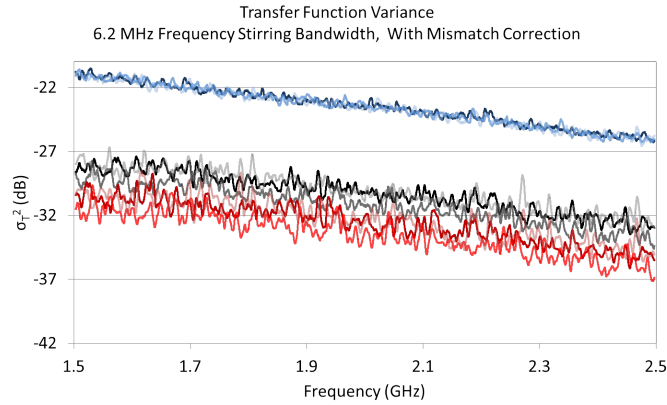
(c) Frequency stirring bandwidth 6.2 MHz, with mismatch correction.

Figure 3.7: Variance of measured transfer functions from Experiment 1. Each of the three figures contains variance curves for antennas 1, 2, and 3, as well as for the unloaded, 2 absorber, and 4 absorber loading cases.
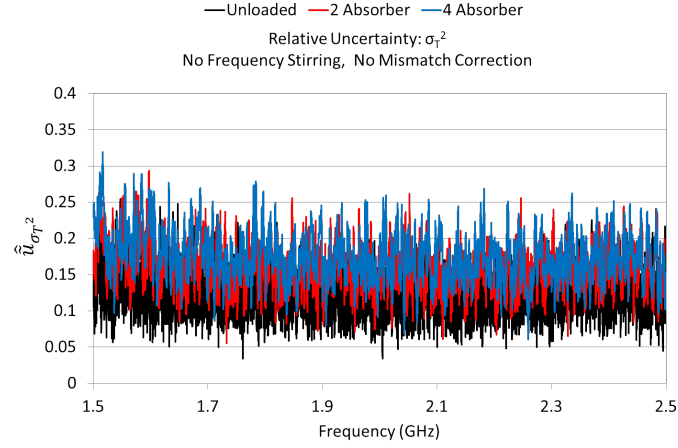
(a) No frequency stirring and no mismatch correction.
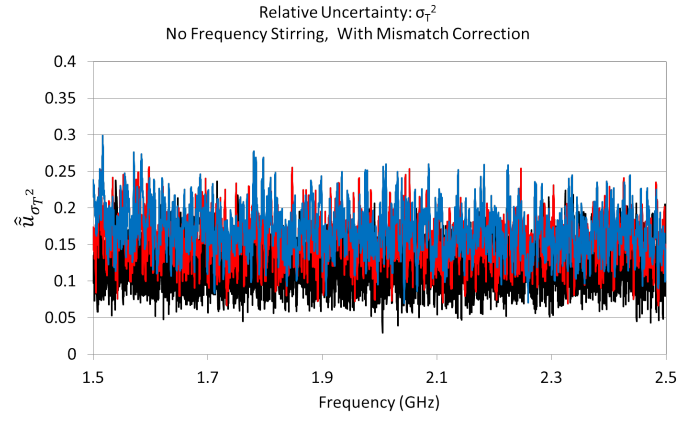
(b) No frequency stirring, with mismatch correction.
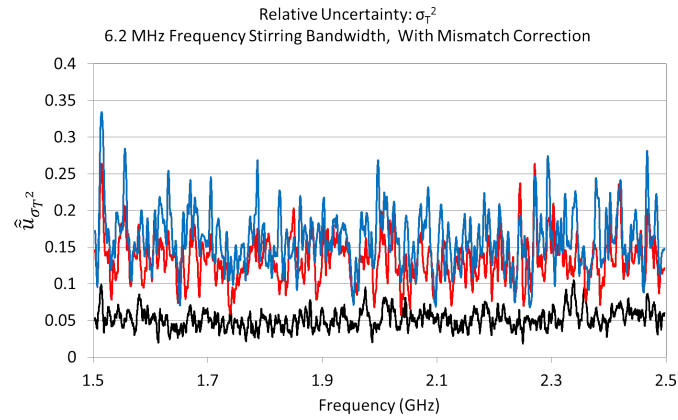
(c) Frequency stirring bandwidth 6.2 MHz, with mismatch correction.

Figure 3.8: Uncertainty estimates obtained from variance of measured transfer functions from Experiment 1. Each of the three figures contains uncertainty estimates for the unloaded, 2 absorber, and 4 absorber loading cases.

absorber loaded cases. This is confirmed by comparing Figures 3.8(b) and 3.8(c), in which it can be observed that the frequency stirring window of 6.2 MHz decreases $\hat{\hat{u}}_{\sigma^2_{\mathcal{T}}}$ of the unloaded case from roughly 0.15 to around 0.06. However, the absorber loaded cases do not show much of an average decrease in $\hat{\hat{u}}_{\sigma^2_{\mathcal{T}}}$ when frequency averaging is used. In addition, the frequency dependence of $\hat{\hat{u}}_{\sigma^2_{\mathcal{T}}}$ has a larger change in magnitude, but also changes more slowly as is made apparent by the larger gap in frequency between the peaks and nulls. The plots in Figure 3.7 do indeed show decreasing $\sigma^2_{\mathcal{T}n}$, and thus they are decreasing the mean power in the RC, which is what absorber is designed to do. On the other hand, the absorber is placed in the working volume of the RC, and thus incident waves interact with all of the absorber faces that do not lie directly on the floor of the RC. Waves incident from the sides of the absorber will not be perfectly absorbed. Instead, the side of the absorber is a lossy boundary with a different impedance than the rest of the space in the RC cavity. Thus, the absorber has a frequency dependent reflection coefficient, and averaging over this frequency dependence results in the behavior observed in Figure 3.8(c). If a wide bandwidth and physically large DUT made from lossy material is to be measured in the RC, the frequency averaged estimate of the uncertainty may be more realistic.

Another method for observing the effects of absorber loading is to plot the Power Delay Profile for different loading cases. In fact, this is used for tuning the RC so as to mimic the decay profile of some real world communications channel. This topic will be discussed in the next section.

3.3   RC Tuning Using the Power Delay Profile

The power delay profile and RMS delay spread are often used for characterizing the frequency selective fading of a multipath wireless channel used in a telecommunications system [49]. From (2.47), the PDP is obtained by averaging many samples of the squared impulse response. In wireless systems analysis, the wireless channel is modeled as a time- and space-varying linear filter, and thus the impulse response gives the channel propagation characteristics at an instance in time and space. Averaging many samples of the impulse response is intended to characterize the channel for the general use of a wireless device that may change position and orientation during operation.

Since the RC itself is a type of wireless environment, it also can be characterized using the PDP and τ_{RMS}.

Other than the RC being essentially a wireless channel, an additional motivation for the use of the PDP in characterizing the RC for wireless device measurement is the relationship between Q and τ_{RMS} [19][51]. For a single cavity mode, the time it takes for the power to decay by $\frac{1}{e}$ is related to the Q of that mode by:

$$\tau = \frac{Q}{\omega} \tag{3.2}$$

In [19] and [51] the assumption is made that the Root Mean Squared (RMS) delay spread τ_{RMS} is similarly related to the composite quality factor Q_{total} by:

$$\tau_{RMS} = \frac{Q_{total}}{\omega} \tag{3.3}$$

In practice this is used for determining a rough order of magnitude for the amount of time over which to take measurements such that the steady state criterion is met. However, it is shown in [26] that method discussed at the end of Section 2.5 is preferred over (3.3) because non-ideal properties of the antennas used lowers the value of Q obtained from the measurement. In addition, RF absorber can be used to tune the RC such that the τ_{RMS} measured in the loaded chamber is similar to that of a real world multipath environment [25]. This allows tests to be performed that have similar frequency selective fading to the target application environment of a wireless device, while maintaining a high degree of control.

In one measurement campaign, the PDP obtained from low frequency measurements in the range of 100 MHz to 2 GHz was explored. The RC used for this purpose was the large NIST RC with dimensions 4.28 m x 3.66 m x 2.9 m. It is known that this RC operates well at frequencies above 300 MHz. The antennas used for this were a log periodic antenna and a discone antenna, both of which are tuned in the range of 100 MHz to 2 GHz. Using antennas that are tuned at frequencies above and below the cutoff of the RC, the idea was to obtain results that show how the PDP and τ_{RMS} change as frequency, and correspondingly the mode density, increases. In the results shown below, the PDPs are computed using a 100 MHz Blackman-Hanning filter. Due

to the lack of resolution, the Blackman-Hanning filter reduces the bias observed in the late time results as compared with a rectangular filter. The center frequency of the filter is swept in order to obtain PDPs at different frequencies enabling the computation of τ_{RMS} as a function of frequency for a given PDP bandwidth.

As observed in previous sections of this chapter, it is often advantageous to combine stirring techniques, which can aid in obtaining less correlated samples. The 100 MHz to 6 GHz measurements were taken using 100 paddle positions. In addition to the results obtained using only paddle stirring, PDPs and τ_{RMS} were also generated using a 10 frequency point, 594 kHz frequency stirring bandwidth (f_s). The results from these computations are shown in Figure 3.9. Along with the measured PDP results for 0.150 and 1.949 GHz are traces that are computed from the assumed exponential decay of the RC. Figure 3.9(a) is obtained using only paddle stirring, so it is assumed that the PDP decays exponentially with the rate of decay governed by τ_{RMS} found using (2.50). The exponential decay is then approximated by the curve given by:

$$Y = A\mathrm{e}^{\frac{-t}{\tau_{RMS}}} \tag{3.4}$$

where A is approximately the value of the PDP at $t = 0$. Frequency stirring is operationally equivalent to applying a rectangular filter, with the specification that it is done on the raw measured data. The Fourier transform of a rectangular function of x gives a $\mathsf{sinc}(x) = \frac{\sin(x)}{x}$ function, whose effect is observed in Figure 3.9(b). In order to compute τ_{RMS}, the PDP should first be corrected for this effect by dividing out the additional $\mathsf{sinc}^2(\frac{\omega_s t}{2})$ (power is the square of the impulse response), where $\omega_s = 2\Pi f_s$. Once this is done, the same linear fit operation, (2.50), can be applied in order to get an estimate of τ_{RMS}. The frequency-stirred PDP is then approximated by the curve given by:

$$Y = A\mathrm{e}^{\frac{-t}{\tau_{RMS}}} \mathsf{sinc}^2(\frac{\omega_s t}{2}) \tag{3.5}$$

The results of the frequency-stirred curve fitting are shown in Figure 3.9(b). What is observed in both plots is that the curve fitting is very good for the PDPs computed at 1.949 GHz. However, the results obtained at 0.150 GHz have much more error. It is obvious from Figure 3.9(a) that the

the assumption of exponential decay is not valid at low frequencies.

Another way to observe the RC behavior at frequencies near the cutoff is to plot the computed τ_{RMS} values as a function of frequency for a given PDP bandwidth. For the cutoff region measurements the results are shown in Figure 3.10. Results from other measurements done with a pair of dual-ridged horns over the frequency range of 1 to 6 GHz are additionally shown. An obvious observation is the relatively higher τ_{RMS} of the measurements taken with the log periodic and discone as compared with the dual-ridged horns. One possible explanation for this is that the low frequency antennas are influencing the measurements due to their physical size. Theoretical formulations of ideal RC behavior make the assumption that the antennas are electrically small, which is definitely not true in the case of the log periodic and discone antennas. As with all wireless measurement systems, the choice of antenna has an affect on the results of the measurement. It is also possible that the deviation is simply due to measurement uncertainty because the difference is on the order of 15%. These measurements were taken at different times, and with the use of 100 paddle positions the theoretical lower bound of uncertainty is 10%. For a direct comparison, it would be best to perform the tests concurrently, and with more paddle positions.

From Figure 3.10 it can be additionally observed that the τ_{RMS} obtained from the frequency stirred data is higher at all frequencies and for all antennas used. Looking back at Figure 3.9 for the 1.949 GHz results, it can be seen that at late times the frequency stirred PDP has more aliasing than the PDP computed using only paddle stirring. This presents a problem, because the method of removing aliasing effects is to take more frequency samples at a finer resolution. However, decreasing the step size between frequency samples increases the correlation between adjacent samples [46]. As a result, it is probably best just to take the τ_{RMS} obtained from frequency stirring in addition to paddle stirring as a rough estimate. Thus, for the purpose of finding τ_{RMS} only, it is probably better not to use frequency stirring. However, if another purpose is found for performing this operation the method presented here could be a reasonable approach for obtaining τ_{RMS}.

In this chapter, some methods for characterizing the RC have been discussed and experimental results have been shown. In the following chapter, a characterization of the RC using computa-

tions of the enhanced backscatter coefficient e_b will be formulated and experimental results will be compared with those obtained in this chapter.

(a) Linear Fit

(b) sinc^2 Fit
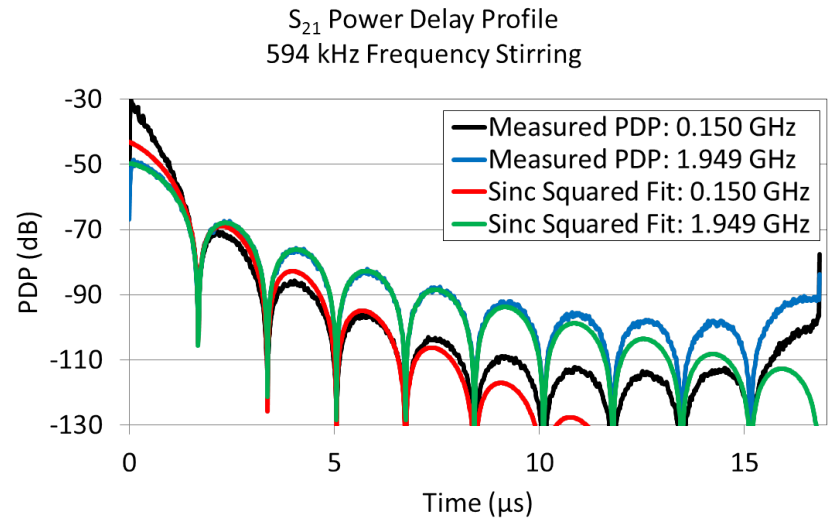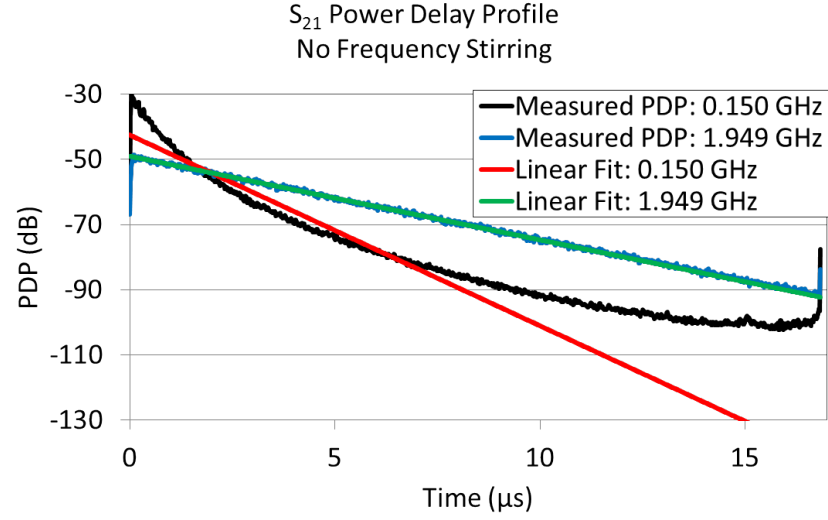
Figure 3.9: Curve-fitting results for PDPs computed from S_{21} data measured in the large NIST RC with dimensions 4.28 m x 3.66 m x 2.9 m.
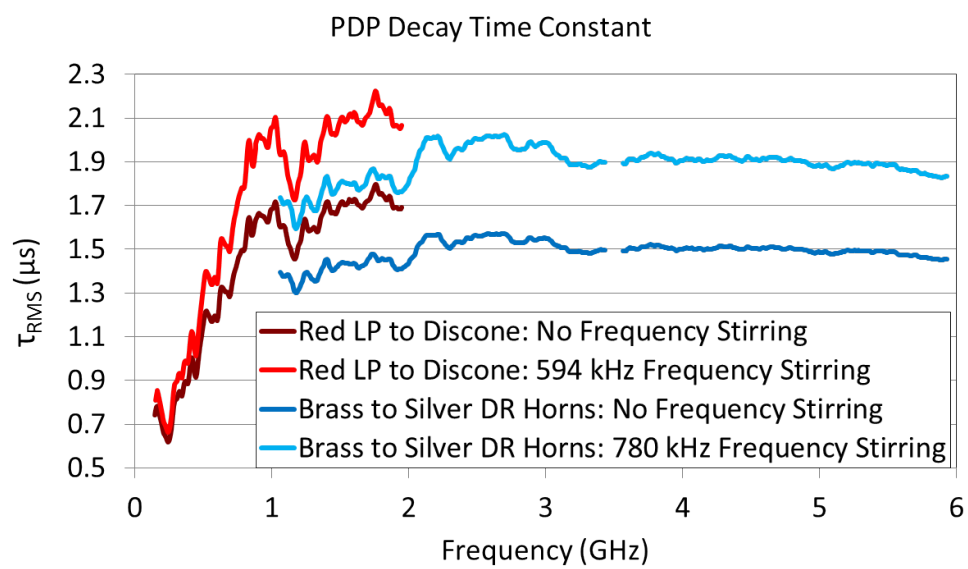
Figure 3.10: Effect of frequency stirring on τ_{RMS} results obtained from PDPs generated using a 100 MHz window, from 100 MHz to 6 GHz, in the large NIST RC with dimensions 4.28 m x 3.66 m x 2.9 m.

Chapter 4

Using Enhanced Backscatter Coefficient for Estimation of RC Measurement Uncertainty

In the previous chapter, two methods for characterizing the RC were presented. While these methods have their advantages and give users different views of how the chamber is performing, their implementation can often present difficulties that must be overcome. If characterization is desirable over wide frequency ranges, it could require the creation and comparison of many different PDF plots. Also, in small chambers or at low frequencies with large antennas, moving the antennas around to get many different samples can be impractical. Another method for characterizing the RC is based on measurements of the Enhanced Backscatter Coefficient, e_b. This method can be implemented using the same data set as is collected for the multiple position variance measurements, with the addition that the reflection data will be used for more than just mismatch correction. In addition, it will be shown in Section 4.3 that a single configuration characterization is also possible using a single position and a pair of antennas. In the following section e_b will be formulated in terms of the measured S-parameters.

4.1   Enhanced Backscatter Coefficient from Measured S-parameters

The simple diagram in Figure 1.6 is a visual aid to help in understanding why it should be expected that the average power received at the source antenna is higher than at some other random location in the RC. In order to determine what the value of e_b should be for an idealized antenna, Hill uses the infinite plane wave model [21]. In carrying out this formulation it is found

that e_b is given by:

$$\langle P_{rf} \rangle = e_b \langle P_{Rx} \rangle \tag{4.1}$$

where, as before, P_{Rx} is the power incident at the receiver and P_{rf} is the power reflected back to the transmitter. Under the limiting assumptions of the infinite plane wave model, the value obtained for e_b is 2. That is, the average power reflected back to the transmitter is twice the average power at the receiver. While this result is perhaps not very intuitive, it is consistent with what has been found in other disciplines such as scattering from rough surfaces in optics [42], and reverberant acoustical fields [30][29].

In addition to assuming that the field can be described as an infinite sum of plane waves, (4.1) also assumes that the antennas used are perfectly matched and lossless. In this limiting case, it has also been shown [33] that e_b is related to the S-parameters by:

$$\langle |S_{11}|^2 \rangle = e_b \langle |S_{21}|^2 \rangle \tag{4.2}$$

Until perfectly matched, lossless antennas are anything more than a mathematical construction, (4.2) is minimally useful for measurement purposes, but it is possible to modify this relationship to include the non-ideal characteristics of real antennas.

To start, the two-antenna RC configuration like that shown in Figure 2.6 will be used, taking note of the labeled power terms. From the power and S-parameter relationships, (2.40), (2.41) and (2.42) derived in Section 2.4 and Appendix B, and dividing $\sigma_{S_{11}}^2$ by $\sigma_{S_{21}}^2$ we obtain:

$$\frac{\sigma_{S_{11}}^2}{\sigma_{S_{21}}^2} = \frac{\eta_A^2 \frac{\langle P_{rf} \rangle}{\langle P_{Tx} \rangle}}{\eta_A \eta_B \frac{\langle P_{Rx} \rangle}{\langle P_{Tx} \rangle}} \tag{4.3}$$

$$= \frac{\eta_A \langle P_{rf} \rangle}{\eta_B \langle P_{Rx} \rangle} \tag{4.4}$$

$$= \frac{\eta_A}{\eta_B} e_b \tag{4.5}$$

Similarly, dividing $\sigma_{S_{22}}^2$ by $\sigma_{S_{21}}^2$ gives:

$$\frac{\sigma_{S_{22}}^2}{\sigma_{S_{21}}^2} = \frac{\eta_B^2 \frac{\langle P_{rf} \rangle}{\langle P_{Tx} \rangle}}{\eta_A \eta_B \frac{\langle P_{Rx} \rangle}{\langle P_{Tx} \rangle}} \tag{4.6}$$

$$= \frac{\eta_B \langle P_{rf} \rangle}{\eta_A \langle P_{Rx} \rangle} \tag{4.7}$$

$$= \frac{\eta_B}{\eta_A} e_b \tag{4.8}$$

The final result is obtained by multiplying (4.5) and (4.8), then taking the square root to give:

$$e_b = \frac{\sqrt{\sigma_{S_{11}}^2 \sigma_{S_{22}}^2}}{\sigma_{S_{21}}^2} \tag{4.9}$$

wherein the antenna efficiencies have canceled. As stated previously, the infinite plane wave model for the RC predicts $e_b = 2$ [21]. However, for the case of simple cavities, such as a rectangular cavity with no paddle, it has been found that the value of e_b depends on the number of spatial dimensions in which the fields can vary [7], and is given by:

$$e_b = \left(\frac{3}{2} \right)^d \tag{4.10}$$

where d is the number of dimensions.

The first example showing e_b for the large, 4.28 m × 3.66 m × 2.9 m, NIST RC from 100 MHz to 2 GHz is shown in Figure 4.1. This data has been frequency stirred with a 594 kHz bandwidth window, corresponding to 10 frequency points, and was taken with 100 paddle positions. As shown, e_b fluctuates more at low frequency, then settles to a tighter variation with an average value of 2.035. This chamber is considered to work well above 300 MHz, which is consistent with the example data having higher fluctuations at frequencies below 300 MHz. The prediction of a value of $e_b = 2$ seems to be fair under certain conditions, but as will be shown in Section 4.4 there are many factors that can affect the measured value of e_b.

A somewhat related method of calculating enhanced backscatter is to use the PDP obtained from the S_{11}, S_{22} and S_{21} data. From this a time domain Enhanced Backscatter Coefficient , E_b, can be defined as:

$$E_b = \frac{\sqrt{PDP^{S_{11}} PDP^{S_{22}}}}{PDP^{S_{21}}} \tag{4.11}$$

Using (4.11), it will be argued in Section 4.4.2 that variations in the value of e_b away from 2 are caused by early time reflected waves. This argument is supported with results shown in Figure 4.9, which also help to qualify E_b as a useful quantity for RC analysis. In the following section, the uncertainty of the various cases of Experiment 1 using the Enhanced Backscatter Coefficient is compared with the results from Section 3.2.
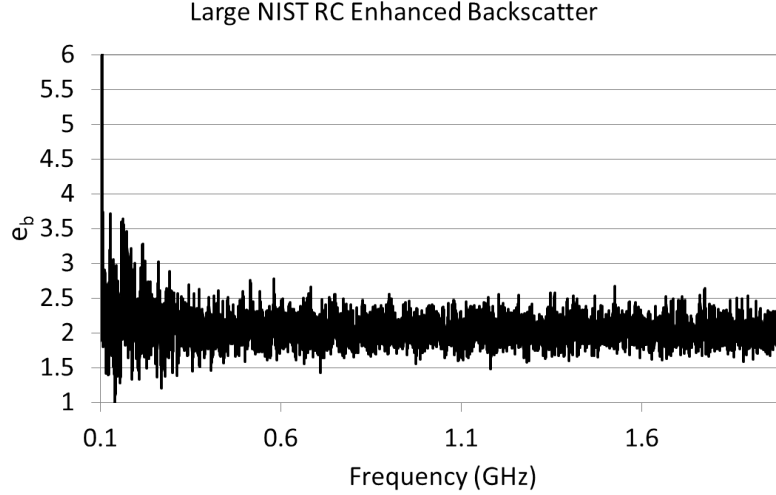
Figure 4.1: An example of e_b measured in the large NIST RC with dimensions 4.28 m x 3.66 m x 2.9 m, using two antennas (a Log Periodic and a Discone). The data has been frequency stirred with a 594 kHz bandwidth window, and was taken with 100 paddle positions.

4.2   Uncertainty Estimates from Enhanced Backscatter Coefficient

Now we come back to the example data set from Experiment 1, with the same cases that were used in Section 3.2. For this data, the measured S_{14}, S_{24}, and S_{34} provide the transmitted variances for (2.40). The monopole reflection data is given by S_{11}, S_{22}, and S_{33} for each measurement group, and S_{44} gives the reflection for the reference horn. The measured e_b results for the Group 1 antennas and for the unloaded, 2-absorber loaded, and 4-absorber loaded cases are shown in Figure 4.2. The first observation made is that Figures 4.2(a) and 4.2(b) are virtually identical. This is the expected result since the efficiency terms, including mismatch efficiency, cancel when calculating e_b using

(4.9). A change in the value of e_b caused by mismatch correction would be an unexpected result and would require further investigation to determine the cause of the error.

If we now compare Figures 4.2(b) and 4.2(c), similar observations can be made as when Figures 3.7(b) and 3.7(c) were compared. It is seen that frequency stirring greatly decreases the spread of the measured results for the unloaded case. Additionally, e_b for the loaded cases has a frequency dependence that has a larger but slower oscillation over frequency, as compared with e_b obtained with no frequency stirring, which was observed in the $\hat{\hat{u}}_{\sigma_{\mathcal{T}}^2}$ plot, Figure 3.8(c). It is interesting that the absorber loading had little effect on the value of e_b, as is made apparent by observing that the different cases lie on top of each other in Figure 4.2(a). However, averaging over the frequency dependency of the data, caused by the absorber, gives much larger variation.

In order to directly compare the $\sigma_{\mathcal{T}}^2$ and e_b results, the relative uncertainty of e_b, $\hat{\hat{u}}_{e_b}$ (found by plugging e_b into (2.52)), was computed and is shown in Figure 4.3. Comparing Figures 4.3(a) and 4.3(b) it is again observed that the two plots are virtually identical. However, some differences are observed when comparing $\hat{\hat{u}}_{e_b}$ and $\hat{\hat{u}}_{\sigma_{\mathcal{T}}^2}$ relative uncertainty estimates. Figure 4.3(a) shows little difference when absorber loading is used in the RC, while Figure 3.8(a) showed an increase in the uncertainty. Furthermore, the unloaded case shows a higher uncertainty when it is estimated with e_b instead of $\sigma_{\mathcal{T}}^2$. This difference is due to the uncertainty of the reflected power that is included in the computation for e_b, but not in the computation for the transfer function $\sigma_{\mathcal{T}}^2$.

Other observations that can be made with the $\hat{\hat{u}}_{e_b}$ results are similar to those made with the $\hat{\hat{u}}_{\sigma_{\mathcal{T}}^2}$ results. Frequency stirring decreases the uncertainty for the unloaded case, as shown in Figure 4.3(c), but has larger and slower frequency variation for the absorber loaded cases. Comparing Figures 4.3(c) and 3.8(c), the inclusion of reflected power variations resulted in $\hat{\hat{u}}_{e_b}$ to be slightly higher than $\hat{\hat{u}}_{\sigma_{\mathcal{T}}^2}$. In addition, the relative uncertainty results shown in Figure 4.3(c) seem less periodic than those shown in Figure 3.8(c), the term periodic being used loosely to refer to the more regular spacing between peaks and nulls. This occurs because the frequency dependence introduced into the transmitted and reflected signals is different due to the difference in signal paths. It is important to note that the frequency dependence of the absorber does not change
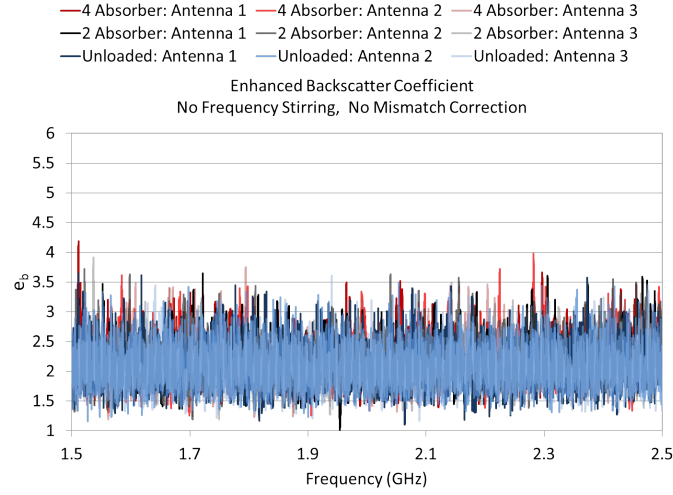
(a) No frequency stirring and no mismatch correction.
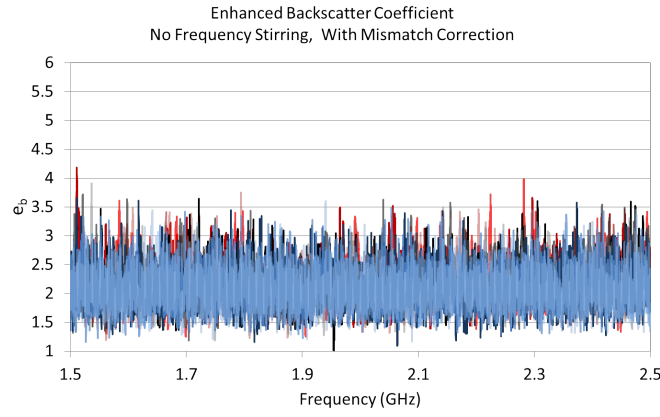
(b) No frequency stirring, with mismatch correction.
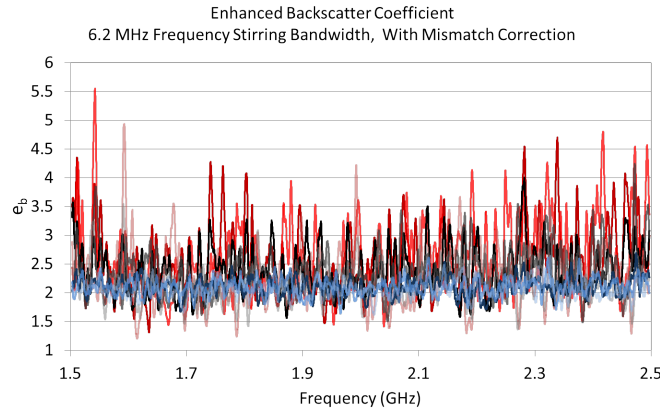
(c) Frequency stirring bandwidth 6.2 MHz, with mismatch correction.

Figure 4.2: Enhanced Backscatter Coefficient for Experiment 1 cases. Each of the three figures contains e_b plotted for AUT 1, 2, and 3, as well as for the unloaded, 2-absorber, and 4-absorber loading cases.

over paddle position, which is why the uncertainty increases when frequency averaging is used. Essentially, the frequency samples become more correlated, making frequency stirring less useful.

These uncertainty comparisons have shown that measurements of the Enhanced Backscatter Coefficient can be used as a method for characterizing the uncertainties of the RC. The uncertainty, $\hat{\hat{u}}_{e_b}$, is different from $\hat{\hat{u}}_{\sigma_\mathcal{T}^2}$ in that it includes the effects of the transmitted and reflected powers in the RC measurement. The drawback is that it has to be done with a VNA to obtain the reflection data, and it still requires measurements at many locations within the RC. In the next section, it will be shown that the uncertainty can be estimated using the results from a single pair of antennas. For measurement involving two or more antennas, this technique allows the RC to be characterized with a single measurement configuration, meaning the same data set used to obtain antenna parameters for some AUT can also be used to estimate the uncertainty of that measurement.

4.3   Single Configuration Uncertainty Estimation

In the previous section it was shown that $\sigma_\mathcal{T}^2$ and e_b data, computed from the 12 AUT positions measured in Experiment 1, give similar uncertainty estimates. The agreement between the uncertainty estimates was shown to be best for the unloaded RC case, while absorber loading and/or frequency stirring the data both resulted in larger differences between the two estimates. These multiple antenna position measurements can be considered to be a multiple configuration RC uncertainty characterization. In the following it will be shown that the variation of e_b over frequency, for a single antenna configuration, can also be used to estimate the uncertainty of the measurement. In this case, the single configuration is considered to be the measurements between a single monopole and the reference horn.

It was observed in Section 4.1 that at high enough frequencies the value of e_b approaches 2. In the frequency range that e_b is close to 2, there is variation over frequency about this mean value. This property can be capitalized on by relating the variation of e_b, within a small bandwidth of frequencies, to the uncertainties of the RC measurement. That is, the variation of e_b over frequency is directly related to the spatial dependence of the RC. Rather than measuring at multiple positions,
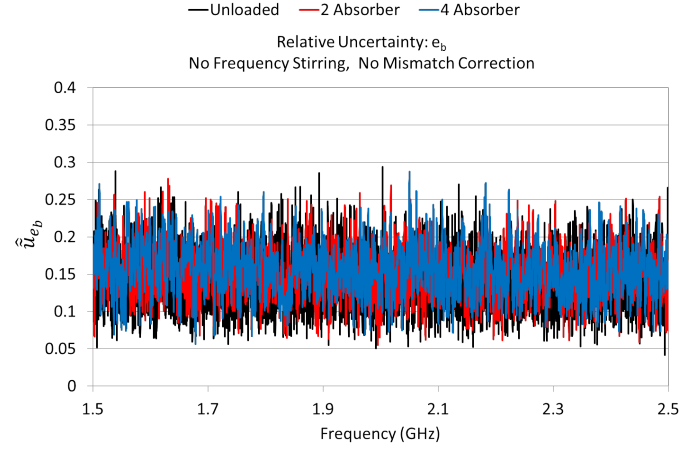
(a) No frequency stirring and no mismatch correction.
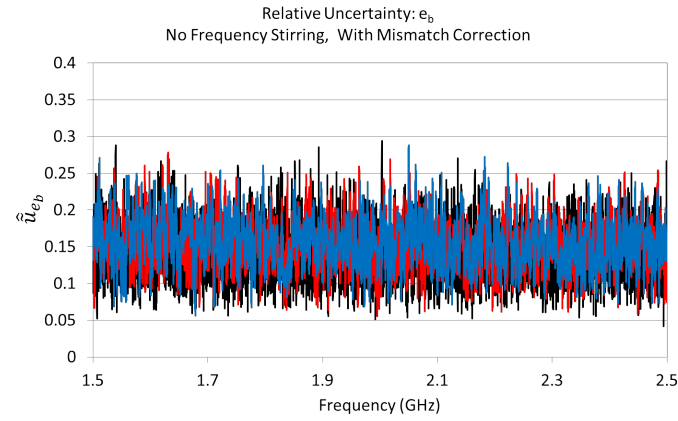
(b) No frequency stirring, with mismatch correction.
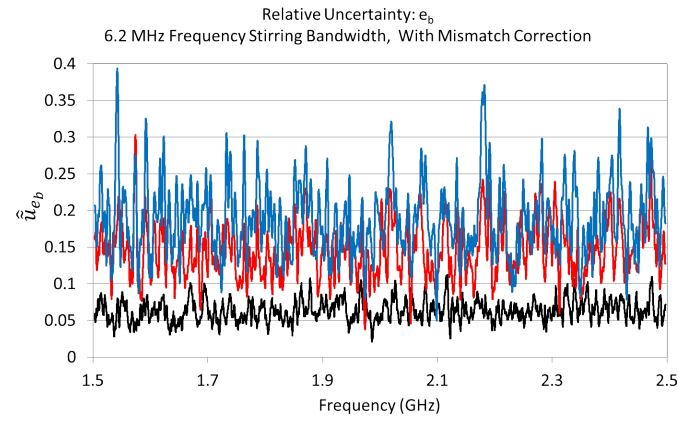
(c) Frequency stirring bandwidth 6.2 MHz, with mismatch correction.

Figure 4.3: Uncertainty estimates obtained from e_b results from Experiment 1 cases. Each of the three figures contains uncertainty estimates for the unloaded, 2-absorber, and 4-absorber loading cases.

samples are collected at multiple frequencies within the small bandwidth and then the computed e_b values are plugged into (2.52) to obtain the uncertainty estimate based on frequency variation of e_b. This operation of computing the standard deviation of e_b over frequency is referred to as the single configuration uncertainty estimation method, and is compared with results from the previous sections in which multiple antenna positions/configurations were used to obtain the standard deviation. Since e_b is expected to be much flatter over a much larger frequency range than the individual $\sigma_{\mathcal{T}}^2$ terms themselves, this leads to the potential for being able to use fairly large bandwidths for computing the uncertainty as compared with the relatively narrower bandwidth over which frequency stirring is a valid operation. Once again, care must be taken because this operation requires averaging over frequency, which under certain conditions has the potential for adverse affects on the computed results as was shown in Sections 3.1, 3.2, and 4.2.

The pair of antennas used for the single configuration RC uncertainty estimation are the reference horn and AUT 1. The results presented in Figure 4.4 compare the uncertainty estimated for the unloaded case for Experiment 1, with no frequency stirring applied, using the single and multiple configuration techniques. The multiple configuration approach takes averages over the 12 antenna positions, while the single configuration approach averages a specified number of consecutive frequencies. Figure 4.4 shows single configuration uncertainty estimates for 12 and 384 frequency samples. As can be observed, the uncertainty estimated from 12 frequency samples is roughly 0.1, while that from the 12 antenna positions is roughly 0.14. If the number of frequency samples is then increased to 384 samples, the new uncertainty estimate for the single configuration technique is also close to 0.14. These plots seem to hint that the number of samples required in the single configuration approach must be much larger than for the multiple configuration to arrive at close to the same uncertainty estimation.

Rather than comparing more plots like that of Figure 4.4 with varying numbers of frequency samples, it is useful to instead plot the average uncertainty over the entire frequency span as a function of the number of frequency samples used to obtain the uncertainty estimate. This is shown in Figure 4.5 for the unloaded and 4-absorber loaded cases, as well as with and without frequency

Figure 4.4: Comparison of single and multiple configuration uncertainty results. The multiple configuration uncertainty estimate is obtained using the 12 antenna measurements from Experiment 1, while the single configuration uses the results from just Antenna 1.

Relative Uncertainty: Single and Multiple Configuration

-- Multi, Unloaded, No Freq. Stirring	Single, Unloaded, No Freq. Stirring
-- Multi, 4 Absorber, No Freq. Stirring	Single, 4 Absorber, No Freq. Stirring
-- Multi, Unloaded, 6.2 MHz Freq. Stirring	Single, Unloaded, 6.2 MHz Freq. Stirring
-- Multi, 4 Absorber, 6.2 MHz Freq. Stirring	Single, 4 Absorber, 6.2 MHz Freq. Stirring

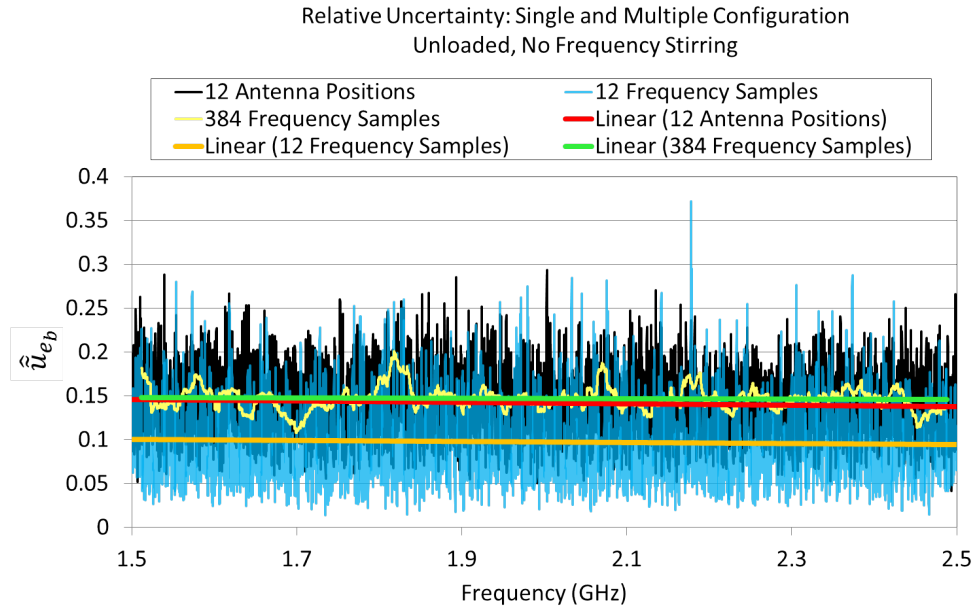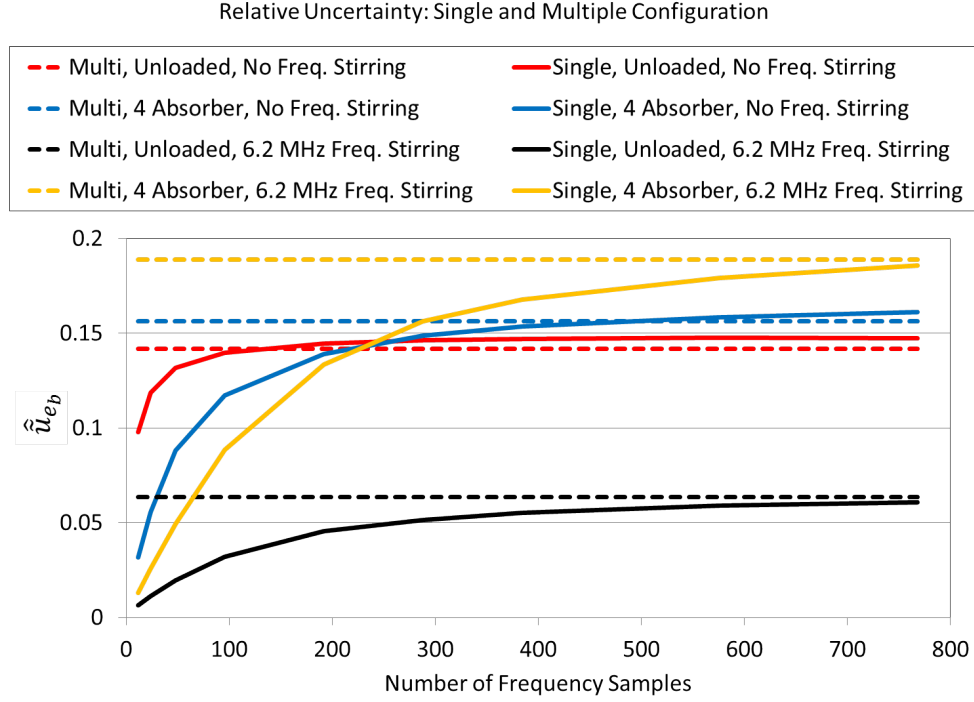Figure 4.5: Comparisons of the single and multiple configuration average uncertainty results. The multiple configuration uncertainty estimate is obtained using the 12 antenna measurements from Experiment 1 and is averaged over the 1.5 to 2.5 GHz frequency range. The single configuration uses the results from just Antenna 1, averaged over the same frequency range, using an increasing number of frequency samples from 12 to 768.

stirring. The number of frequency samples ranges from 12 to 768, and the step size between frequency samples was roughly 166 kHz. This means that the sample windows range roughly from 2 to 128 MHz. It can be observed that for each case, the wider the sample window used to estimate the uncertainty, the more the average uncertainty estimated from the single configuration data approaches a constant value. In addition, for each case shown this constant value is close to the uncertainty estimated from the multiple configuration data.

From these test cases that represent some of the typical RC measurement configurations, the single configuration uncertainty estimation method agrees very well the results from the multiple configuration method. It is noted that the single configuration method requires more frequency samples as compared with spatial samples to obtain good agreement with the multiple configuration method. From Figure 4.5, it is apparent that the minimum bandwidth and number of frequency samples needed to obtain this agreement changes depending on the measurement configuration and stirring method. It is likely that the wider bandwidths used, around 100 MHz, could give similar results with fewer, evenly-spaced samples. If this is true, then it is highly probable that the required spacing between frequency samples can be correlated with the relative distance between the antennas in the multiple configuration uncertainty estimation method. This analysis is left for future development. In the following section different measurement examples will be presented that resulted in e_b values different from 2, with a discussion about the probable cause in each case.

4.4   Enhanced Backscatter Coefficient Conditional Variations

It has been shown experimentally and theoretically that the value of e_b is dependent on many factors [21][62][31][7]. These factors include things like the dimension of the RC cavity, the number of interacting modes and how well mixed the fields are, not to mention a number of others. In the following, different measurement examples will be presented to give an idea of how much variation is caused by irregularities in the transmission medium used to get power to and from the antennas in the RC, as well as the effect of antenna pattern at different frequencies.

4.4.1   Transmission Line and Waveguide Irregularity Effects

It is true in general for measurements involving transmission lines that defects in the transmission line can cause adverse effects on the measured results. In one example, the defects of a coaxial cable that fed a test antenna did not result in unusual transmission or reflection results observed in the frequency domain. The cable did not show any issues when performing pre-test calibration and system checks. After calibration the cable was connected to a 9.5 cm standard gain horn and measured along with a dual-ridged horn reference antenna. The reflection coefficient measured for the 9.5 cm standard gain horn is shown in Figure 4.6 for the initial test (1) and for a repeat test (2). The only difference between Test 1 and Test 2 is in the cable used to feed the AUT. While the two measurements are slightly different, the results from Test 1 do not seem unusual in themselves, and without having done the second measurement the results look fairly typical.

Figure 4.6: Effect of a coaxial cable defect on the measured reflection coefficient. The data was taken with a 26.2 cm (aperture cross width) dual-ridged horn, and a 9.5 cm X-band standard gain horn, inside the NIST large chamber with dimensions 4.28 m x 3.66 m x 2.9 m. Test 1 has a cable that was subsequently determined to have a flaw. Test 2 is a repeat test with a different cable.

From the reflection coefficient results shown in Figure 4.6, it was not particularly clear that there was anything wrong with the data collected from Test 1. However, as shown in Figure 4.7, Test 1 performed with the flawed cable resulted in a value of e_b greater than 4 that also exhibits

large scale changes with frequency. Repeat tests with better cables resulted in a much lower e_b, but still not quite equal to 2, and there is a linearly increasing trend with frequency. This has been observed to be linked to the use of high gain antennas, and will be discussed further in Section 4.4.2. In another measurement, the standard gain horn was replaced by a monopole and placed in the same location. As shown in Figure 4.7, doing this resulted in a lower e_b, with an average value of about 2.2 that is flatter over frequency. Given these different results, it is apparent that in each case the cable with a defect alters the values computed from the measurements. However, the reflection coefficient results from Figure 4.6 are only marginally different, and only from duplicate tests with different cables is the defect detected. Conversely, the e_b results show very large differences between the test cases. More importantly, the e_b results from just Test 1 are unusually high, and seem to oscillate over frequency, allowing one to detect such a defect on a singular basis without the need for subsequent measurements. This technique provides a quick method for determining calibration issues that arise from changes that occur after the calibration is completed and the cables are connected to the test antennas.

In another example, the non-ideal properties of a waveguide 90° bend were observed to have an adverse effect on the resultant e_b value. This test was done in the NIST small RC with dimensions 1.02 m × 0.673 m × 0.572 m, that is used for high frequency measurements. The experiment was done at a frequency range of 40 to 50 GHz, using WR-19 waveguide standard gain horns and sections of WR-19 waveguide to connect the antennas to the VNA. Multiple measurements were taken using the high frequency RC with the WR-19 antennas, and while doing so it was noticed that some results had unusually high e_b values that oscillate with frequency. In a test to verify the cause, the antennas were connected in two configurations that used a WR-19 90° E-plane bend on the AUT to face the antennas away from each other. The first configuration had the AUT connected directly to the WR-19 90° E-plane bend. The second configuration had an additional straight section of WR-19 waveguide to go between the 90° E bend and the AUT. The results from this test are shown in Figure 4.8.

It is thought that the larger magnitude and frequency variation of e_b for the first configuration,
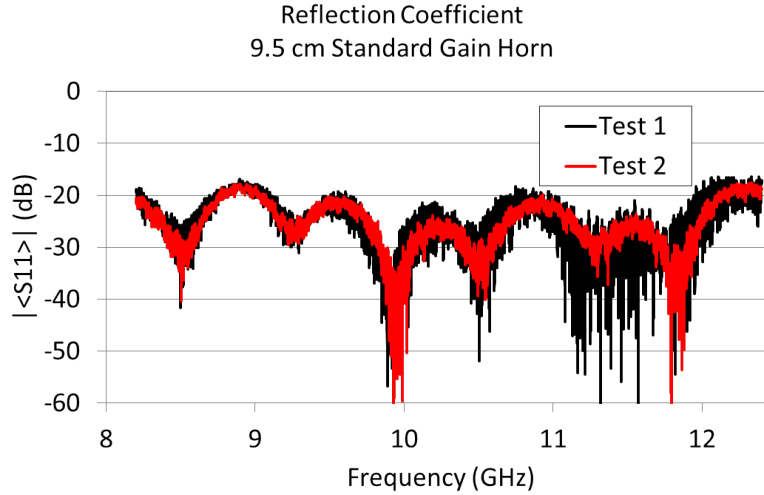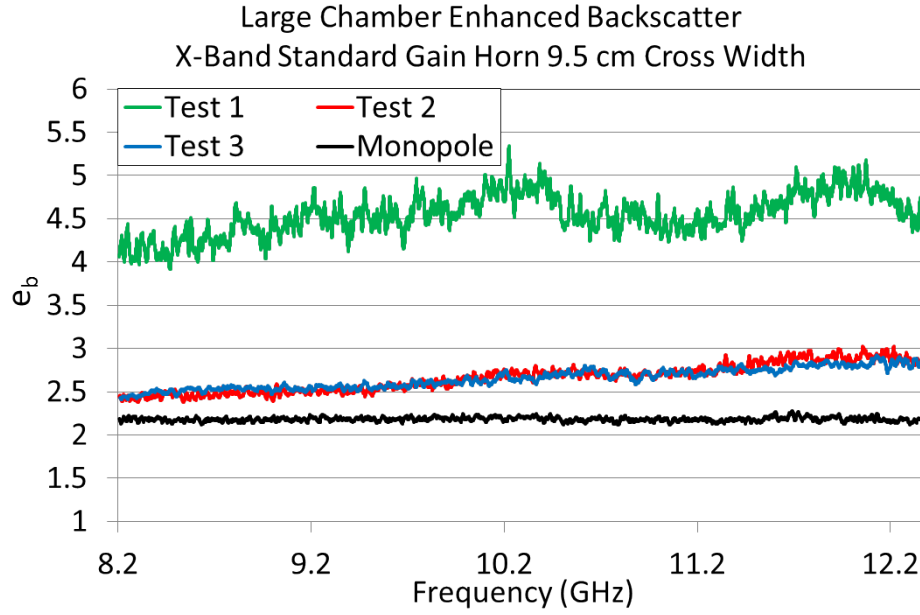
Figure 4.7: Effect of a coaxial cable defect on the resultant e_b value. The data was taken with a 26.2 cm (aperture cross width) dual-ridged horn, and a 9.5 cm X-band standard gain horn, inside the NIST large chamber with dimensions 4.28 m x 3.66 m x 2.9 m. The flawed cable results were obtained in Test 1, while repeat tests with a new cable are shown as Test 2 and 3. Also shown for reference are the results from the dual-ridged horn and a monopole used at its second resonance with center frequency around 11 GHz.

shown in Figure 4.8, is caused by high order modes in the waveguide that are excited by the input signal traveling through the 90° bend. The justification for this is that the distance from the bend to the interface between the bend and the AUT is roughly 2.54 cm. The half period of oscillation shown in Figure 4.8 is roughly 6 GHz, which is a full wavelength of 2.5 cm. Adding the extra waveguide section increases the path length of the input signal which allows the high order modes to attenuate to insignificant levels before reaching the interface connecting the waveguide and AUT. The effect on the value of e_b is that it flattens out, but it can still be observed that its value is in the range of around 3.5 to 4. Although the value is higher than expected, this range of e_b values can be consistently measured in the high frequency RC when using high gain antennas, while lower e_b values are achieved with wide beam antennas.

It was observed in these two cases that the value of e_b can be affected by defects, or even just non-ideal characteristics that are neglected, in the transmission medium that connects the antennas placed inside the RC to the external VNA. It was also observed that high gain antennas can also result in values of e_b higher than 2, which will be discussed further in the following section.

4.4.2 Paddle and High Gain Antenna Interaction

The e_b value of around 3.75 in the high frequency measurement was an unexpected result. It was previously thought that the value of e_b would just be tighter around 2, given that the mode density at 45 GHz, even with the smaller chamber size, is very high in the RC. However, there was a major difference between the measurements that had been done in the large RC and those done in the small RC: the relative electrical size of the two RCs. The small RC was being operated around 45 GHz, while the larger RC was being operated at less than 6 GHz and more often in the neighborhood of 1 GHz. The small chamber has dimensions of 1.02 m x 0.673 m x 0.572 m, and was being measured at a center frequency of 45 GHz, a wavelength of 6.67 mm. The larger chamber dimensions are 4.28 m x 3.66 m x 2.9 m. To perform measurements with a similar electrical size to the measurements performed in the small RC, the larger chamber should be operated at around 9 GHz. The full list of dimensional parameters used for scaling from the small RC to the large RC

Figure 4.8: Effect of high order waveguide modes on the resultant e_b value. This data was taken with two WR-19 standard gain horns in the NIST high frequency RC with dimensions 1.02 m x 0.673 m x 0.572 m. Both configurations use waveguide sections to feed the antennas, and both have 90° bends to point the antennas away from each other. The red trace has the standard gain horns connected directly to the 90° bend, while the black trace includes an additional 4 inch straight section of WR-19 waveguide between the bend and the antenna.

are shown in Table 4.1. As shown, 9 GHz is a compromise with respect to the electrical length of the different compared dimensional parameters.

Table 4.1: This table shows the electrical length for the small RC operated at 45 GHz and the large RC operated at 9 GHz.

Scale Small Chamber to Large Chamber				
	Small RC		Large RC	
	Initial Frequency / Wavelength 45 GHz / 6.67 mm		Scaled Frequency / Wavelength 9 GHz / 33.3 mm	
Chamber	Dimension (m)	Dimension (λ)	Dimension (m)	Dimension (λ)
Width	1.02	152.9	4.28	128.5
Depth	0.673	100.9	3.66	109.9
Height	0.572	85.8	2.9	87.1
Paddle				
Distance from Wall	0.127	19.0	1.07	32.1
Panel Length	0.292	43.8	0.94	28.2
Panel Width	0.152	22.8	0.787	23.6
Total Length	0.546	81.9	2.46	73.9

In addition to operating at a higher frequency, it was noticed that the orientation of the main lobe of the antennas with respect to the paddle also played a role in the increased value of e_b. Thus, it was desirable to use standard gain horns for the large chamber measurements as well. Standard gain horns that operate at 9 GHz are X-band waveguide horns that range from 8.2 to 12.4 GHz. The full measurement campaign consisted of several types of standard gain horns with directivities ranging from around 14.5 to 22 dB. The WR-19 horns used for the high frequency measurements have an average gain of around 20 dB. It was hoped that the lower frequency equivalent measurements could be correlated with the gains of the antennas. Unfortunately, the cable issue mentioned in the previous section affected the first batch of data collected for this study, and the two highest directivity horns had been borrowed and had to be returned. Fortunately, subsequent measurements between the 9.5 cm X-band standard gain horn and a second resonance monopole produced useful results.

Time Domain Enhanced Backscatter Coefficient
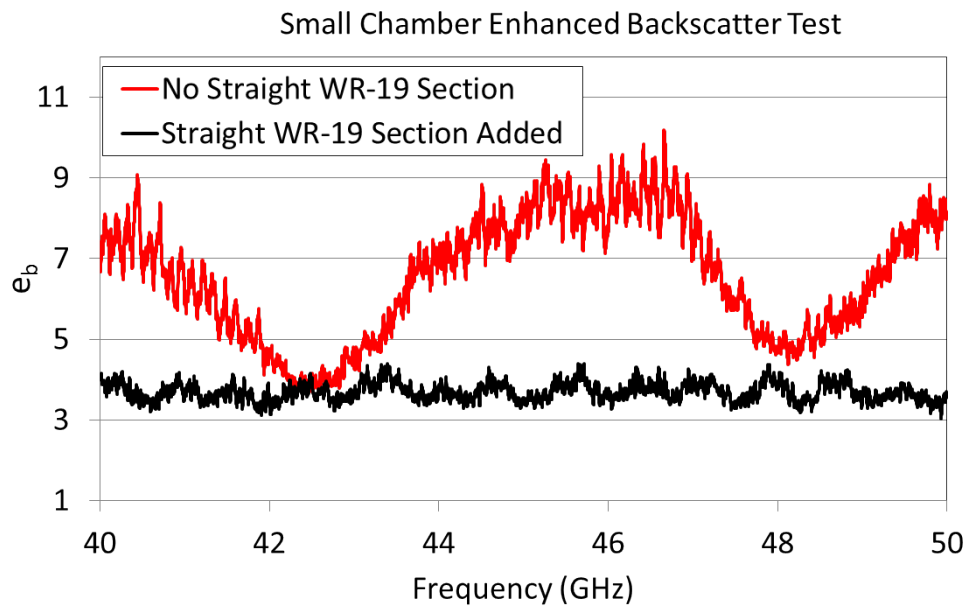**Small High Frequency RC**
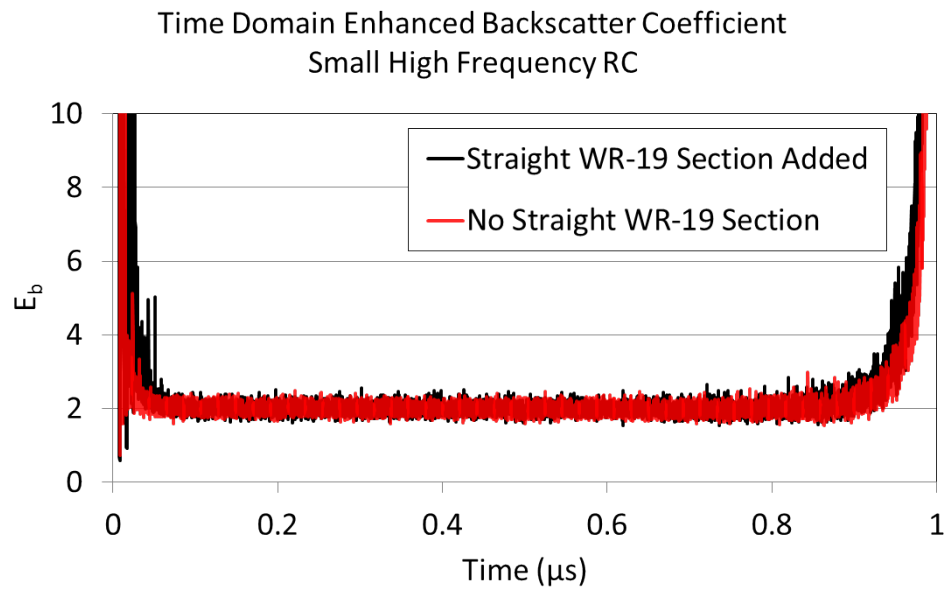
Figure 4.9: Effect of high order waveguide modes on the resultant E_b value in the time domain. This data was taken with two WR-19 standard gain horns in the NIST high frequency RC with dimensions 1.02 m x 0.673 m x 0.572 m. Both configurations use waveguide sections to feed the antennas, and both have 90° bends to point the antennas away from each other. The red trace has the standard gain horns connected directly to the 90° bend, while the black trace includes an additional 4 inch straight section of WR-19 waveguide between the bend and the antenna.

One idea that was explored was that the increase in the value of e_b might be related to how much of solid beam angle of the antenna directly illuminates the paddle. This was motivated by the difference in E_b (4.11) observed in the time domain as shown in Figure 4.9, which was obtained from the same data set used for the frequency domain e_b shown in Figure 4.8. The large E_b value observed at early times is due to waves that undergo fewer reflections and add coherently at the source. As time increases, the value of E_b flattens and centers around 2, as would be expected for a well-stirred RC. The late time response behavior is due to aliasing, so the data is only valid to around 0.8 μs. As shown, the response for both test configurations settles to roughly the same value after the early time transient response decays. From these observations it was apparent that the increased value of e_b was a result of early time interactions between the directive antenna and the paddle. Because of the dependence of e_b on the antennas' pointing directions with respect to the paddle, it was thought that possibly the change in e_b could be related to the amount of direct radiation that illuminates the paddle.

If a standard gain horn is placed close to and directed at the paddle, almost all of the antenna's radiation will interact with the paddle before reflecting to other parts of the RC. As the horn is moved further away from the paddle, less of the antenna's radiation will directly illuminate the paddle, and more of the direct radiation will instead reflect off the walls. This experiment was done using a 9.5 cm X-band waveguide horn, with the horn pointed directly at the paddle, and was moved from 0.75 m to 1.75 m linearly away from the paddle. Additionally, a second resonant monopole with a center frequency of about 11 GHz was measured at the 1.25 m position, along the same line as the standard gain horn. The reference antenna for this experiment was a dual-ridged horn that operates from 1 to 18 GHz. This horn was faced at the other paddle about 1 m away. This configuration was chosen to mimic some of the tests done in the small high frequency RC, in which the standard gain horns face opposite paddles, roughly 22 cm away. At 45 GHz, 22 cm is the same number of wavelengths as 1.1 m at 9 GHz. Some of the results from these tests are shown in Figure 4.10.

It can be observed from Figure 4.10 that the e_b results for the standard gain horn and the
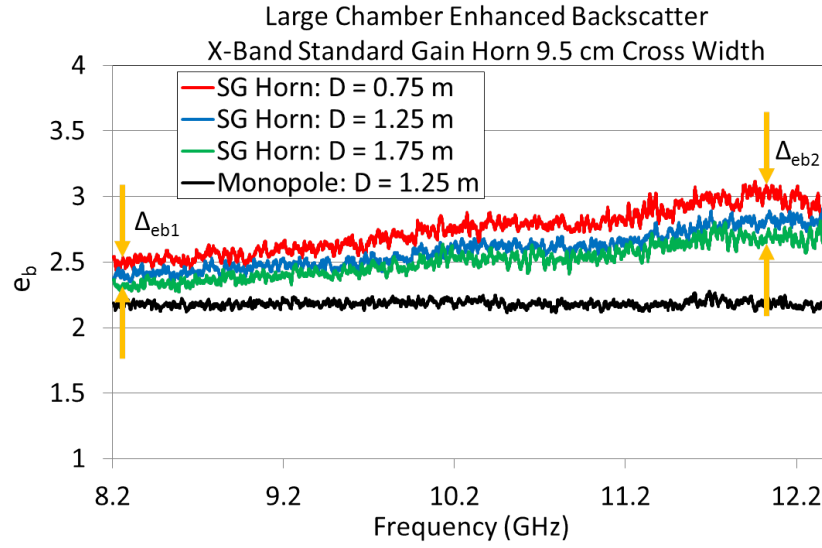
Figure 4.10: Variation of e_b with the distance of the 9.5 cm X-band standard gain horn to the paddle. The horn is pointed directly at the center of the vertical paddle, is polarized vertically, and is displaced linearly away from the paddle from 0.75 m to 1.75 m. The second resonance monopole is also placed at 1.25 m for comparison. Both antennas are measured against a dual-ridged horn that was left in a fixed position during the measurements.

monopole, both measured at 1.25 m away from the paddle, differ by roughly 0.2 to 0.7. This range of differences is caused by the increasing slope of e_b as a function of frequency observed from the standard gain horn results, while the monopole results are relatively much flatter. In addition to the difference between the standard gain horn and the monopole, there is also a difference in the value of e_b of the standard gain horn measured at the different locations. As the horn is moved closer to the paddle, keeping the horn pointed at the center of the paddle, the value of e_b correspondingly increases. This difference between e_b for different measurement positions also appears to have a frequency dependence, increasing slightly at higher frequency. As can be observed in Figure 4.10, this effect is less pronounced than the overall frequency dependence of the horn, with $\Delta_{eb1} \approx 0.2$ and $\Delta_{eb2} \approx 0.4$.

One attempt to quantify the change in e_b due to the amount of radiated power that directly illuminates the paddle was to compute what will be called the paddle coverage factor (CF), given by:

$$CF = \frac{P_{rad}^{\theta_{max}}}{P_{rad}^{Total}} \tag{4.12}$$

where P_{rad}^{Total} is the total radiated power computed from the full radiation pattern, and $P_{rad}^{\theta_{max}}$ is the part of the radiated power that directly illuminates the paddle. Figure 4.11 illustrates what is meant by θ_{max} with a monopole antenna shown in the diagram. Presumably, using the three-dimensional antenna pattern in this calculation would produce the most accurate results. However, it is unclear at this point if this is the correct method for defining a paddle coverage factor. As a first attempt to determine if CF follows similar trends as e_b does in Figure 4.10, the theoretical horizontal, two dimensional, pattern of a vertically polarized 9.5 cm standard gain horn was used to compute CF. The paddle width used for the CF computation was 0.787 m, which is the maximum width of the paddle (of course, CF will be different for different paddle positions). The distances used were 0.75 m to 1.75 m in steps of 0.25 m, similar to the AUT measurement positions relative to the paddle. The results of the CF computation with the given conditions are shown in Figure 4.12. The results are plotted as the $\sqrt{CF}$ because the paddle and horn antenna interaction effects only

$\sigma^2_{S_{11}}$ which enters the e_b computation under the square root in (4.9).
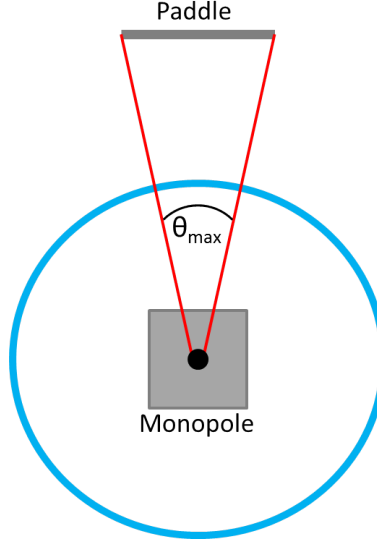
Figure 4.11: Geometry illustrating the meaning of θ_{max} for calculating CF (4.12) for a circular pattern from a monopole.

Comparing the results shown in Figures 4.10 and 4.12, CF does have some of the same overall trends as e_b, but there are also significant differences. The percent change computed from Δ_{eb1} and Δ_{eb2}, shown in Figure 4.10, is roughly 8.2% and 12.2%, respectively. The percent change computed from Δ_{CF1} and Δ_{CF2}, shown in Figure 4.12, is roughly 14.4% and 7.8%, respectively. While the percent differences of e_b and $\sqrt{CF}$ with the antenna's distance to the paddle have similar values, the trends go in different directions as frequency increases: Δ_{CF} decreases, Δ_{eb} increases. Both results do however, show an overall increasing trend as frequency increases.

It is apparent from Figure 4.10 that the paddle and AUT can interact adversely, causing the value of e_b to increase. However, the the paddle coverage factor as defined by (4.12) does not fully explain the measured results obtained in the RC. It is not shown here, but plots of the different variance components reveal that the change in e_b observed in Figure 4.10 is due to an increase in $\sigma^2_{\mathcal{R}}$ that is measured on the standard gain horn, while $\sigma^2_{\mathcal{T}}$ remains relatively unchanged between the measurements. In order to characterize the interaction between the paddle and the AUT, a model paddle was built from aluminum foil lined foam panels and a foam column, with similar

Figure 4.12: Variation of $\sqrt{CF}$ for different antenna placement distances away from the paddle. The antenna pattern used for the calculation is a 2 dimensional cross section of a 9.5 cm standard gain horn polarized along the length of the paddle. The paddle is 0.787 m wide.
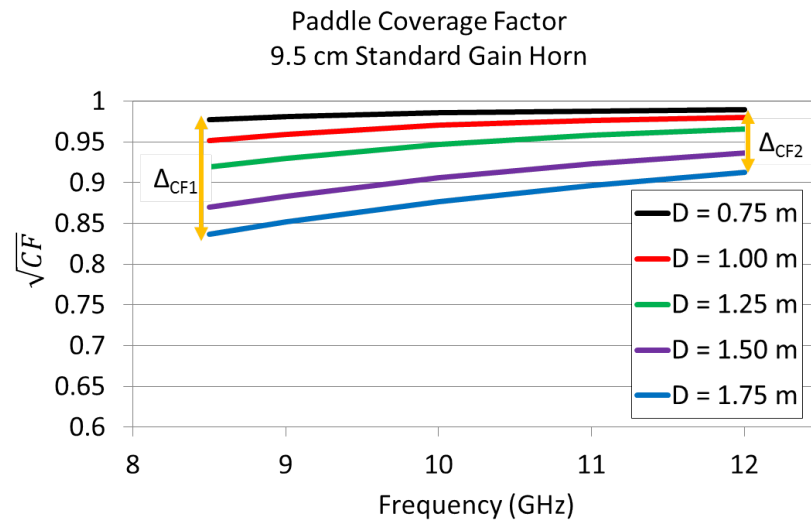
overall shape and dimensions as the large NIST RC paddles. The model paddle was then placed in an anechoic room as well as in the RC, and in each environment the reflection coefficient, S_{11}, was measured and used to compute $\sigma_{\mathcal{R}}^2$. These reflection measurements consisted of a single antenna placed in each environment, at a distance of 229 cm from the center rotation point of the paddle, with the paddle rotated horizontally to 360 positions at $1°$ increments. For both environments, the second-resonance monopole, the 9.5 cm standard gain horn, and the dual-ridged horn were measured at close to the same location, with all of them polarized vertically. The distance was chosen based on constraints from the space available in the anechoic room, and in both environments the paddle illumination was changed by rotating the antenna rather than displacing it. The second-resonance monopole has an omni-directional pattern about the horizontal rotation plane, so it was measured only in a single position. The two horn-type antennas were pointed directly at the paddle, this position being designated as the $0°$ direction, and then rotated $20°$ and $40°$ about the vertical axis. Figure 4.13 shows the model paddle in the anechoic and reverb environments.

The results from the reflection measurements conducted in the anechoic and RC environments using the model paddle are shown in Figure 4.14. It can be observed that the relative power levels measured in the RC are much higher than in the anechoic room, as should be expected. In addition, in both environments $\sigma_{\mathcal{R}}^2$ decreases as the antenna is pointed away from the paddle. This is obviously expected in the anechoic room because the paddle is the only object that can produce a measurable reflection. In the RC this decreasing trend in $\sigma_{\mathcal{R}}^2$ is what is under investigation, but from the proximity results shown above these results were also expected. Unfortunately, the low power measured in the anechoic room with the antenna pointed at $40°$ was corrupted by the noise floor of the VNA, and in the upper half of the frequency range, noise is the dominant response. The low frequency portion of the $40°$ pointing direction seems to have low enough noise levels to make reasonable comparisons, as does the full frequency range for the $0°$ and $20°$ directions. As shown, the reflected, stirred power measured in the anechoic room, as compared to the RC, decreases by a much larger margin when the antenna is rotated. Using the same conditions, a distance of 229 cm and pointing directions $0°$, $20°$ and $40°$, CF was once again computed with the results shown
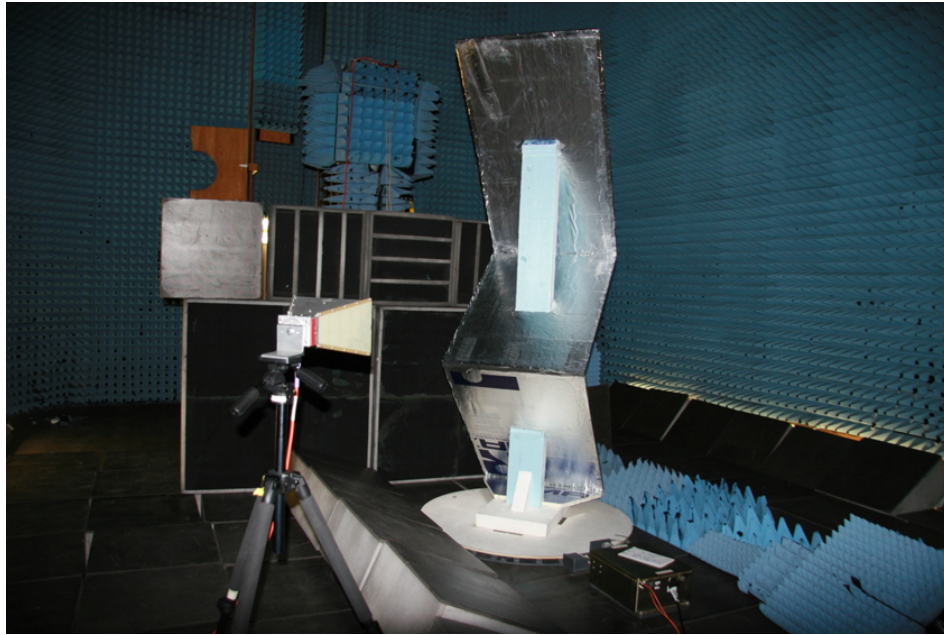
(a) Model Paddle Placed in the Anechoic Room.
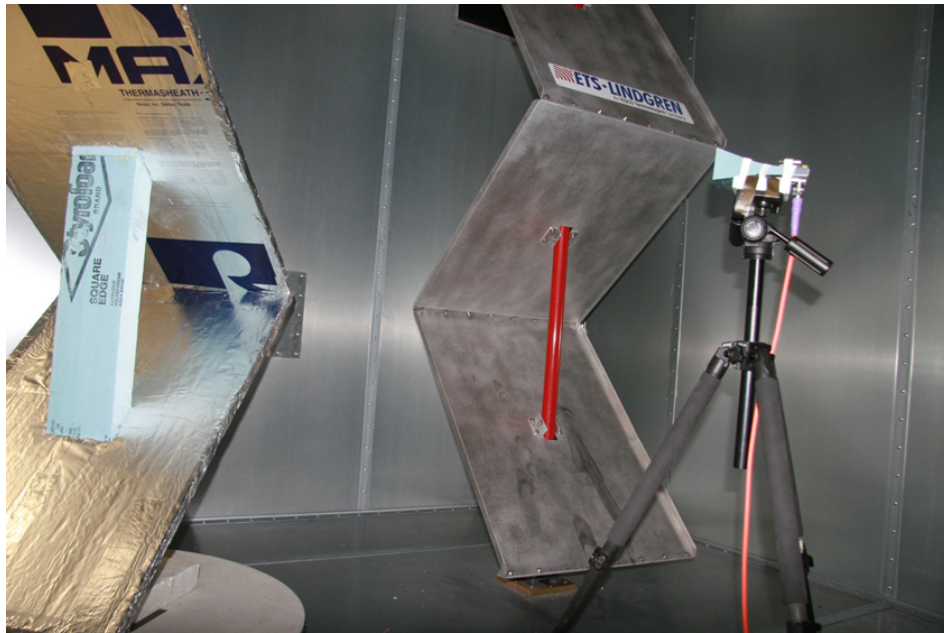
(b) Model Paddle Placed in the Reverberation Chamber.

Figure 4.13: The Model paddle in the RC and an anechoic room. The anechoic room is the NIST spherical near field range that was modified for the purposes of this experiment. The RC is the NIST 4.28 m x 3.66 m x 2.9 m chamber.

in Figure 4.15. This time, CF is plotted on the dB scale for direct comparison with the $\sigma_{\mathcal{R}}^2$ plot.

In comparing Figure 4.14 and 4.15, it can be observed that CF has a trend that is much more like that of the anechoic $\sigma_{\mathcal{R}}^2$ measurement results. This observation is aided with the percent variations shown in Table 4.2 computed from $\Delta_{Var,RC}^n$ and $\Delta_{Var,An}^n$ shown in Figure 4.14, and Δ_{CF}^n shown in Figure 4.15, where $n = 1$ to 4. As shown in the table, the trends are all similar, but the magnitudes between the anechoic and CF results are much more comparable, while the e_b variation is much smaller. As frequency increases, noise makes it difficult to distinguish the anechoic results accurately, but it appears that for the $0°$ and $20°$ cases the results are fairly flat. On the other hand, CF increases for the $0°$ case and decreases for the $20°$ case. This is possibly due to the use of the two dimensional antenna pattern to approximate the radiated powers for computing CF. It is again observed that the RC results decrease in $\sigma_{\mathcal{R}}^2$ value as the antenna is pointed away from the paddle, but not by the same order of magnitude as the anechoic $\sigma_{\mathcal{R}}^2$ and CF. From these results it is apparent that the average power of a single reflected EM wave from the paddle back to the source antenna does follow CF as formulated in (4.12). However, what is also clear is that the paddle enhancement observed in the RC does not follow the same magnitude of variation as CF. The multiple reflections from the RC reduces this variation, but the fact that the variation exists shows that the gain of the antenna can have an effect on the spatial uniformity of the RC. The data from Figure 4.9 indicated that early time reflections cause the spatial non-uniformity. However, the multiple peaks in the early time data also indicate that there are multiple reflections, rather than a single reflection. Thus, the coverage factor that predicts the correct magnitude of variation observed in the RC data would likely need to be averaged over the multiple reflections that occur at early times.

In this chapter, the use of e_b as a quantity for characterizing the uncertainty of measurements conducted in the RC was discussed and compared against using the transfer function for this purpose. It was additionally shown that the response of e_b is flat, on average, over frequency under certain ideal conditions, and that this property can be taken advantage of in order to estimate the uncertainty of RC measurements using a single two-port measurement configuration. Lastly,
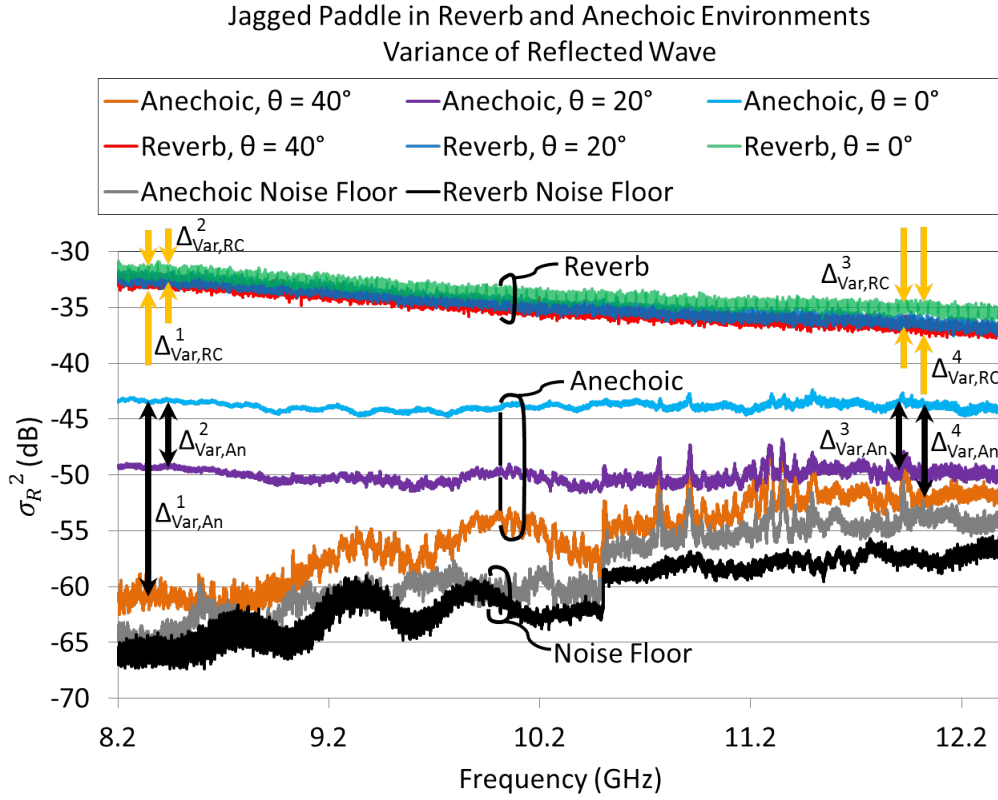
Figure 4.14: Variation of $\sigma_{\mathcal{R}}^2$ for different antenna pointing directions with respect to the paddle, as measured in the anechoic room and RC. A 9.5 cm X-band standard gain horn was placed a distance of 229 cm from the center of the paddle's rotation axis to the horns aperture face. As shown, the anechoic results exhibit distortion due to the noise floor, thus a plot of the noise floor for each environment is also included. The step observed at 10.5 GHz is caused by a change in the amplifier used by the VNA.
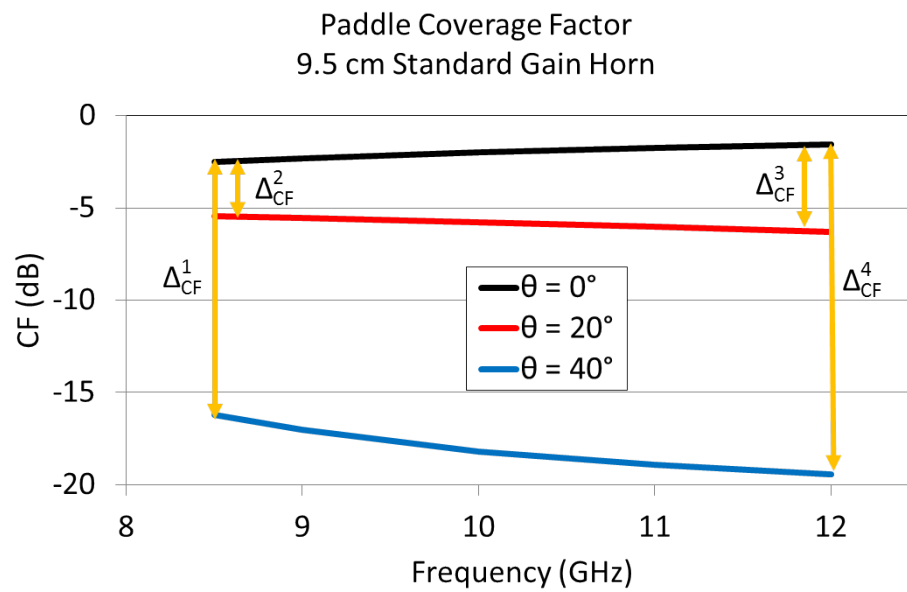
Figure 4.15: Variation of CF for different antenna pointing directions with respect to the paddle. The antenna pattern used for the calculation is a two-dimensional cross section of a 9.5 cm standard gain horn polarized along the length of the paddle. The paddle is 0.787 m wide, and the antenna is placed 229 cm from the center of the paddle's rotation axis.

Table 4.2: Percent variation of $\sigma_{\mathcal{R}}^2$ in the anechoic (An) and RC environments for data shown in Figure 4.14, as well as CF shown in Figure 4.15.

Paddle Coverage % Variation				
	8.5 GHz		12 GHz	
	Δ^1: 0° - 20°	Δ^2: 0° - 40°	Δ^3: 0° - 20°	Δ^4: 0° - 40°
$\Delta_{Var,RC}$	16.9	20.6	25.8	30.8
$\Delta_{Var,An}$	73.7	98.2	71.1	82.6
Δ_{CF}	49.3	95.7	66.3	98.4

the variation of e_b for different measurement conditions was discussed. In the following chapter the value of e_b obtained from a one-dimensional and a two-dimensional bounded cavity Green's function model will be shown and compared with measured results.

<center>**Chapter 5**</center>

<center>**Semi-Analytic and Numerical RC Models**</center>

There are three kinds of models that are often used for describing the statistical behavior of the RC: plane wave, modal, and ray. The plane wave and ray models are most accurate in the limit of short wavelengths. The modal technique is required to efficiently describe the low frequency behavior of the RC and to explore the statistics of an RC used in less than ideal conditions. One method that is used to obtain the modal behavior of the RC is to use the Green's function of a bounded cavity. The Green's function models for one- and two-dimensional cavities are used in the following sections to explore the variation of e_b and other parameters under different limiting conditions.

5.1 One- and Two-Dimensional Bounded Cavity Green's Functions

The one-dimensional bounded cavity consists of two perfect electric conductor (PEC) boundaries separated by a distance a. Inside of this cavity an ideal current source, given by $\vec{J} = J_0 \sin(\omega t)\hat{\mathbf{z}}$ is placed at location x_0. The geometry of this model is shown in Figure 5.1. With a sinusoidal source and no other active components, the assumption of $e^{j\omega t}$ time dependence is valid and the electric field is found from:

$$\nabla \times \nabla \times \vec{E} + k^2 \vec{E} = j\omega\mu\vec{J} \tag{5.1}$$

With no source variation in the $\hat{\mathbf{z}}$ direction we have $\nabla \cdot \vec{E} = 0$, which simplifies (5.1) to:

$$\frac{\partial^2 E_z}{\partial x^2} + k^2 E_z = j\omega\mu J_0 \tag{5.2}$$

In a general time harmonic EM field problem, the electric field and the Lorenz vector potential, using the Lorenz gauge, are related by:

$$\vec{E} = -j\omega\vec{A} + \frac{\nabla\nabla \cdot \vec{A}}{j\omega\mu\epsilon} \tag{5.3}$$

Plugging (5.3) into (5.2) and simplifying we arrive at:

$$\frac{\partial^2 A_z}{\partial x^2} + k^2 A_z = -\mu J_0 \tag{5.4}$$

Using the Green's function method, the one-dimensional wave equation for a delta source $\delta(x - x_0)$ is given by:

$$\frac{\partial^2 g}{\partial x^2} + k^2 g = -\delta(x - x_0) \tag{5.5}$$

where g is the one-dimensional scalar Green's function. Additionally, in the general case the dyadic Green's function $\vec{G}$ and the Lorenz vector potential $\vec{A}$ are related by:

$$\vec{A}(x_1) = \mu \int_V \vec{J}(x_0)\vec{G}(x_1, x_0) dV_0 \tag{5.6}$$

where V is the volume of the general source centered at x_0. Using (5.6), A_z is given in terms of g by:

$$A_z = \mu J_0 g(x_1, x_0) \tag{5.7}$$

Lastly, (5.7) is plugged into (5.3) to give the electric field in terms of the one-dimensional scalar Green's function as:

$$E_z = -j\omega\mu J_0 g(x_1, x_0) \tag{5.8}$$

Following the formulation given in [14], the Green's function for the one-dimensional bounded cavity with perfectly conducting walls is:

$$g(x_1, x_0) = \frac{1}{k\sin(ka)} \begin{cases} \sin k(a - x_0)\sin(kx_1), & \text{for } x_1 < x_0 \\ \sin k(a - x_1)\sin(kx_0), & \text{for } x_1 > x_0 \end{cases} \tag{5.9}$$

which is plugged into (5.8) to give the electric field.

(a) Source, observation point, and boundary axis labels.
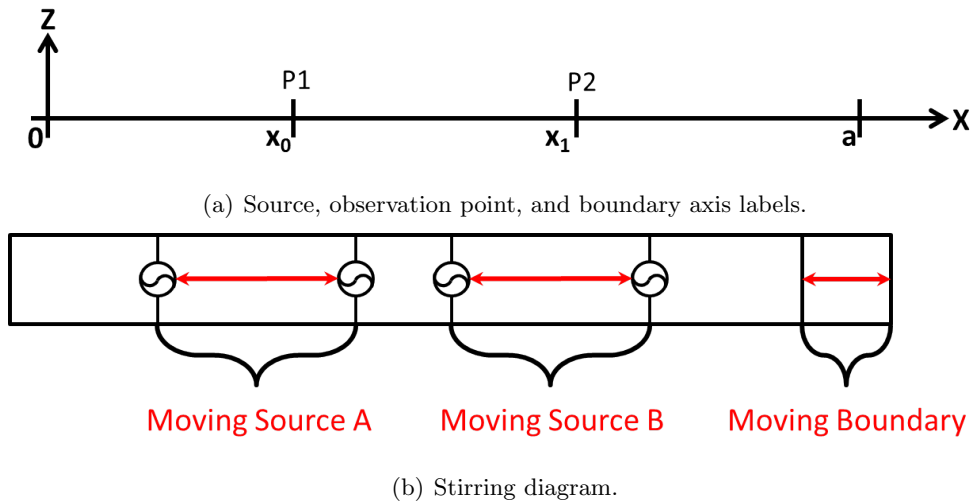

(b) Stirring diagram.

Figure 5.1: Geometry of the one-dimensional bounded cavity model. As shown, the cavity boundaries are at 0 and a along the x-axis. The source and observation point used in the model are labeled as x_0 and x_1, respectively. Changing the position of either or both sources, as well as the boundary at a can be used as stirring mechanisms in this model.

In order to compute e_b from the electric field found using the Green's function model two sources must be placed in the one-dimensional cavity. To stay consistent with S-parameter terminology, the sources are denoted by port numbers P1 and P2. In order to obtain the data needed to compute S_{21}, the source position x_0 is placed at P1 and the observation point x_1 is placed at P2. For the reflection at each port, the source and observation point are set to the same location: both at P1 for S_{11} and both at P2 for S_{22}. Thus, it takes three separate computations to obtain the electric field data needed for the full two port model. The electric fields from these three computations are designated as E_{21}, E_{11} and E_{22}. To compute the S-parameters from the electric field, the impedance matrix must first be computed. The impedance of the current source to the electric field is defined as:

$$Z = \frac{E}{J_0} \tag{5.10}$$

If the computed electric fields E_{21}, E_{11} and E_{22} are plugged into (5.10) we get Z_{21}, Z_{11} and Z_{22}. The impedance matrix to S-parameter transformation formulas are given as [47]:

$$S_{11} = \frac{(Z_{11} - Z_0)(Z_{22} + Z_0) - Z_{21}Z_{12}}{\Delta Z} \tag{5.11}$$

$$S_{21} = \frac{2Z_{21}Z_0}{\Delta Z} \tag{5.12}$$

$$S_{22} = \frac{(Z_{11} + Z_0)(Z_{22} - Z_0) - Z_{21}Z_{12}}{\Delta Z} \tag{5.13}$$

where

$$\Delta Z = (Z_{11} + Z_0)(Z_{22} + Z_0) - Z_{21}Z_{12} \tag{5.14}$$

and the characteristic impedance is taken to be the intrinsic impedance of free space $Z_0 = 377\Omega$. For this reciprocal system, $Z_{12} = Z_{21}$. From this point onwards, the S-parameters obtained from the Green's function model will be treated in the same way as those obtained from measurement.

Similarly to the one-dimensional RC model, a two-dimensional model is obtained from the two-dimensional Green's function of a bounded cavity containing a line source. A diagram of the two-dimensional bounded cavity model is shown in Figure 5.2. In the z direction the geometry of the model extends to infinity so that the fields only vary in the x and y directions. Given the geometry

of this problem, only TE modes are excited. The electric field resulting from the two-dimensional bounded cavity Green's function, formulated in [21], is given by:

$$E_z = \frac{2j\omega\mu J_0}{a} \sum_{m=1}^{\infty} \frac{\sin(\frac{m\pi x_0}{a})\sin(\frac{m\pi x}{a})}{k_m \sin(k_m b)} \begin{cases} \sin(k_m y_0)\sin k_m(b-y), & \text{for } y > y_0 \\ \sin k_m(b-y_0)\sin(k_m y), & \text{for } y < y_0 \end{cases} \tag{5.15}$$

If the wall conductivity is finite, resulting in a finite Q, the modal wave number k_m can be expressed as:

$$k_m = \sqrt{k^2(1 + \frac{j}{2Q})^2 - (\frac{m\pi}{a})^2} \tag{5.16}$$

As shown in [21], a solution for the Q of the two-dimensional model can be obtained by assuming the source is in the working volume of the RC, and the steady state condition has been met (power transmitted into the RC is equal to the power dissipated by the walls). The result of these assumptions is that Q is given by:

$$Q = \frac{2A}{\mu_r \delta L} \tag{5.17}$$

where $A = ab$, and $L = 2(a+b)$, and δ is the skin depth of the metal boundary given by:

$$\delta = \sqrt{\frac{2\rho}{\omega\mu}} \tag{5.18}$$

and ρ is the resistivity of the cavity walls. By estimating ρ as the inverse of the conductivity of aluminum, roughly 28 nΩ·m, the resulting Q for the frequency range of 100 MHz to 6 GHz is on the order of 10^5. However, as discussed in [63], for the two-dimensional bounded Green's function model, a Q on the order of 10^4 gives results that are more comparable with three-dimensional RC measurements. It was found that this was also the case for the present modeling efforts. The results shown in Section 5.3 use $\rho = 9.22 \times 10^{-4}$ Ω·m, which results in $Q = 10^4$ at 6 GHz.

With the one- and two-dimensional RC models formulated, the following sections explore the value of e_b obtained for varying model parameters within the limitations imposed by the models. Variation of the wall positions is used to mimic paddle stirring. While this does have the effect of changing the boundary conditions, the walls in the model can only move in a line, which is expected to be less effective than turning an irregularly shaped paddle. Source position variation is used
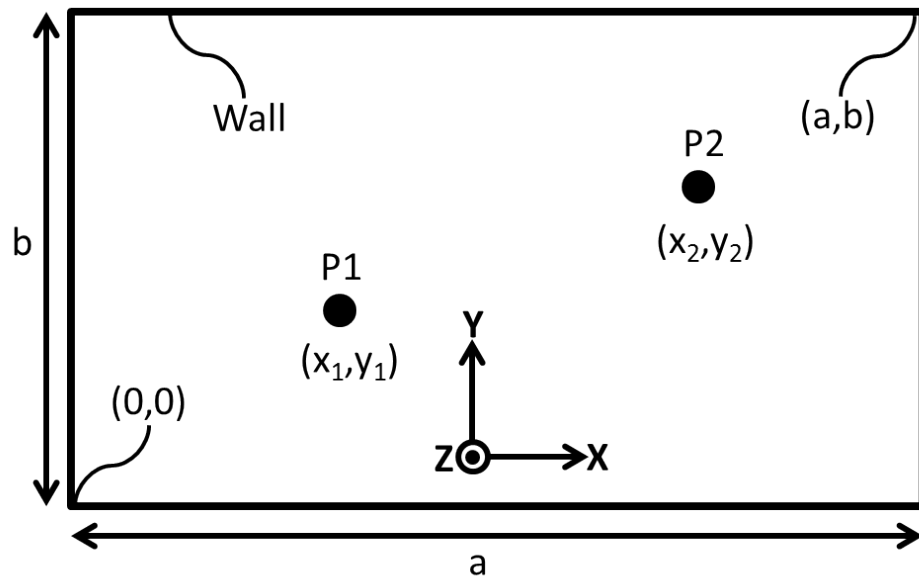
Figure 5.2: Geometry of the two-dimensional bounded cavity containing a source.

to mimic antenna position stirring, but the ideal sources in the models cannot be reoriented and movement is restricted by the dimension of the particular model. How wall and position stirring are accomplished for the one-dimensional model are shown in Figure 5.1(b). Frequency stirring is implemented using the same methods as when using measured data. However, a three-dimensional cavity (particularly one that contains a paddle) has many more modes that can be excited within a specific frequency range as compared to the one- and two-dimensional cavities. Thus, all of these stirring methods are expected to be less effective in the one- and two-dimensional models versus when similar methods are used in measurements. Within these limitations, the value of e_b obtained from the models can be explored for specific types of variation.

5.2 One-Dimensional Enhanced Backscatter Coefficient

The single space dimension model represents the limit of the RC in which only the TEM mode exists. In this limit the amplitude variation with frequency is characterized by distinct peaks [23]. These peaks occur at regular intervals with a constant frequency step between adjacent peaks, and the step size is given by:

$$\Delta f = \frac{c}{2a} \tag{5.19}$$

where a is the width of the cavity as shown in Figure 5.1. As will be shown below, the regular spacing of the peak field amplitudes in frequency is a cause of the different stirring mechanisms to produce different results. This means that the single dimensional model, as well as the low frequency RC, are not completely ergodic, i.e., changes in frequency, paddle positions, and antenna position do not lead to equivalent statistical response curves.

In order to observe changes in the fields in the same frequency range that is typically used in the large NIST RC, with a similar cavity electrical length, the base width of the model is set to 4.28 m, corresponding to the largest cavity dimension in the large NIST RC. The frequency range used in the model is 100 MHz to 6 GHz, a range typically used in the large NIST RC. With this one-dimensional model of the RC, a series of simulations were run to observe how the fields, and other

computed results, vary as different parameters are changed. One set of simulations left the source positions fixed while the wall position was varied by pseudo randomly selecting the parameter a at 100 positions between a minimum of 4.28 m up to 0.3 m longer at 4.58 m. Another simulation set has the wall position fixed, and the source positions pseudo randomly chosen. The choice of source position maintains a distance of 0.3 m from either wall, positions are not repeated, and the two sources never share the same location. Lastly, a simulation set was run with fixed wall and source positions, with additional frequency points collected. The extra frequency points were used in post processing to frequency stir the raw data.

The variations of S_{21} for these different simulation sets are shown in Figure 5.3. It is important to note that each plot in Figure 5.3 is on a different scale. It is apparent just from this difference in scale that the fields are not ergodic as they should be for a truly reverberant environment. This is additionally supported by the differences between the source position simulation set and the other simulation sets. From Figure 5.3(c), it can be observed that there is no specific spacing between resonant peaks. However, from Figure 5.3(b) the observable resonant peaks from the frequency varied data are separated by roughly 35 MHz steps, corresponding to $a = 4.28$ in equation (5.19). Also, from Figure 5.3(a) the wall position movement resulted in peaks that correspond to half wavelength of the frequency, making the peaks 15 cm apart for the 1 GHz data and 2.5 cm apart for the 6 GHz data.

The one-dimensional Green's function RC model was used to explore the value of e_b that is obtained within the limitations discussed above. The results of e_b computed from the wall movement, source location movement, and frequency stirred simulation data sets are shown in Figure 5.4. As can be seen, the value of e_b obtained is very different for each data set. The wall movement case has an e_b that is 1 at all frequencies, which shows that the received and reflected power is varying by the same amount as the wall moves. Conversely, the source position movement case has an e_b that is close to 0.5 but has some small amount of oscillation about this value. Additionally, the frequency-stirred case has an e_b that is minimally 1 and consists of a series of regularly spaced resonant peaks of varying amplitude. Recalling the results from Figure 4.1 that
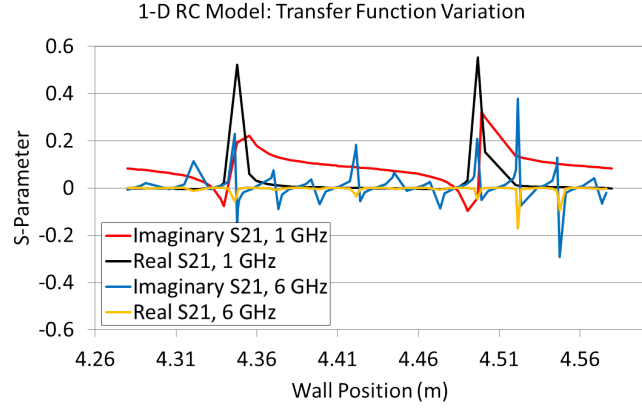
(a) Moving Wall: wall moved between 4.28 m and 4.58 m at 100 pseudo randomly chosen positions, (P1,P2) = (1.111,2.384) m, at 1 and 6 GHz.
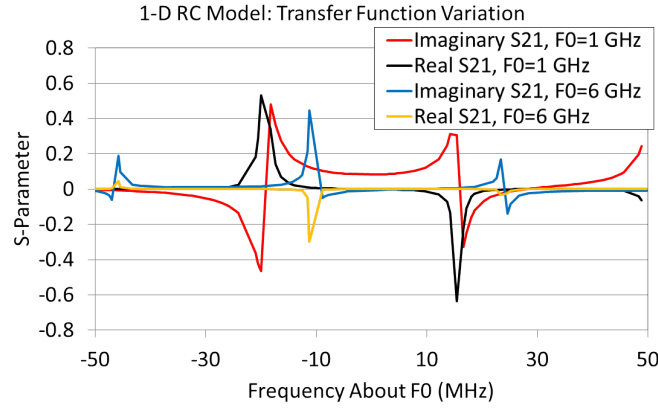
(b) Frequency Variation: 100 frequency points pseudo randomly chosen over a 100 MHz span about center frequencies 1 and 6 GHz, and (P1,P2) = (1.928,2.411) m.
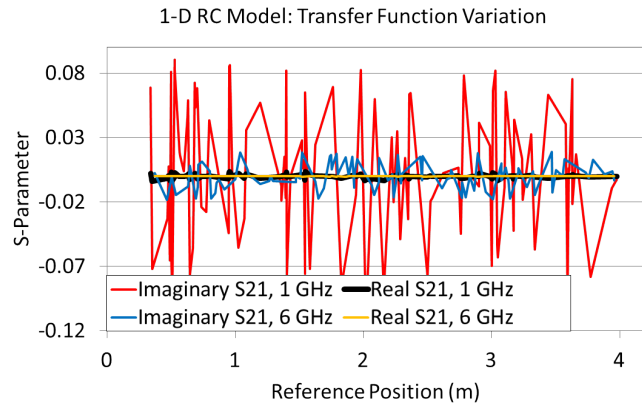
(c) Moving Source Position: 100 pseudo randomly chosen (P1,P2) positions, with no repeating or overlapping positions, at 1 and 6 GHz.

Figure 5.3: Variation of S_{21} for different varying parameters in the one-dimensional Green's function RC model with a 4.28 m width.

were measured in the large NIST RC from 100 MHz to 2 GHz, the low frequency range of e_b varies more and has sharp resonant peaks as compared with the higher frequency portion of the data. The resonant peak structure is similar to the results of the frequency stirred simulation data set, but there is not enough measured low frequency data to determine if the peaks are regularly spaced. If frequency stirring, wall movement stirring, and source movement stirring are used together, the trace marked "All Stirring" is the result. As shown, the value is slightly over 1.5 across most of the frequency span. This agrees well with (4.10), which predicts a value of 1.5 for a one-dimensional cavity.
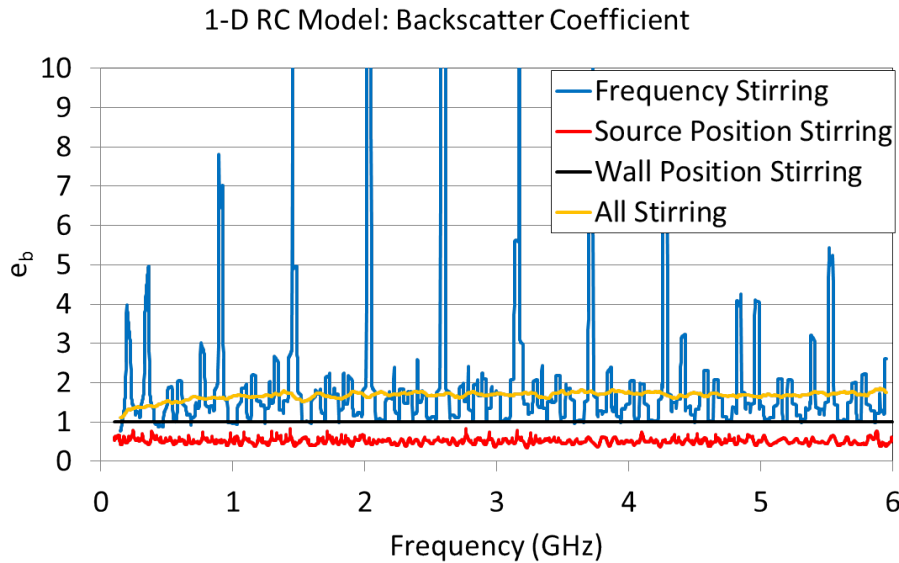
Figure 5.4: Enhanced backscatter from the one-dimensional Green's function RC model for the simulation sets described for Figure 5.3.

In Chapters 3 and 4, the PDP and E_b were shown to be useful in characterizing the response of a wireless channel. For the one-dimensional Green's function RC model, the PDP and E_b resulting from the wall movement and source position movement simulation sets are shown in Figure 5.5. Discussion of these results will be carried out in the following section and compared with corresponding results from the two-dimensional Green's function RC model.

(a) Power Delay Profile

(b) Time Domain Enhanced Backscatter Coefficient
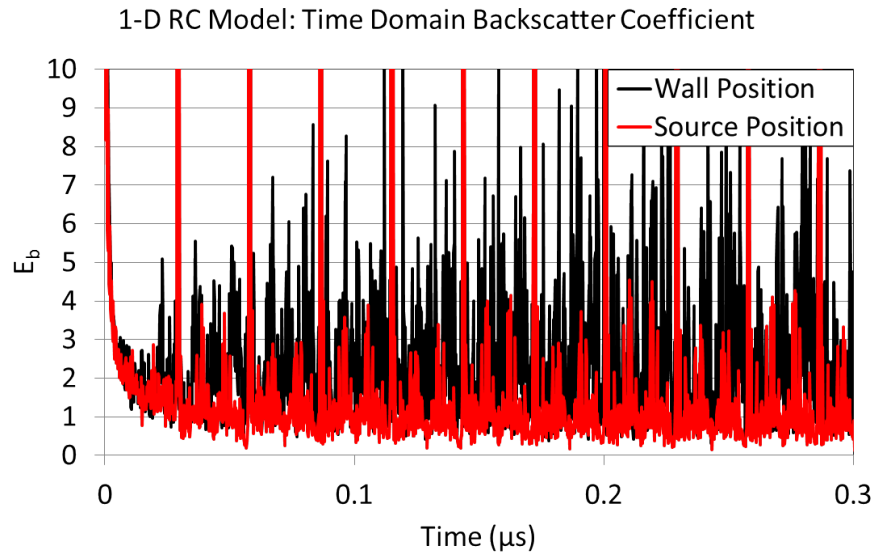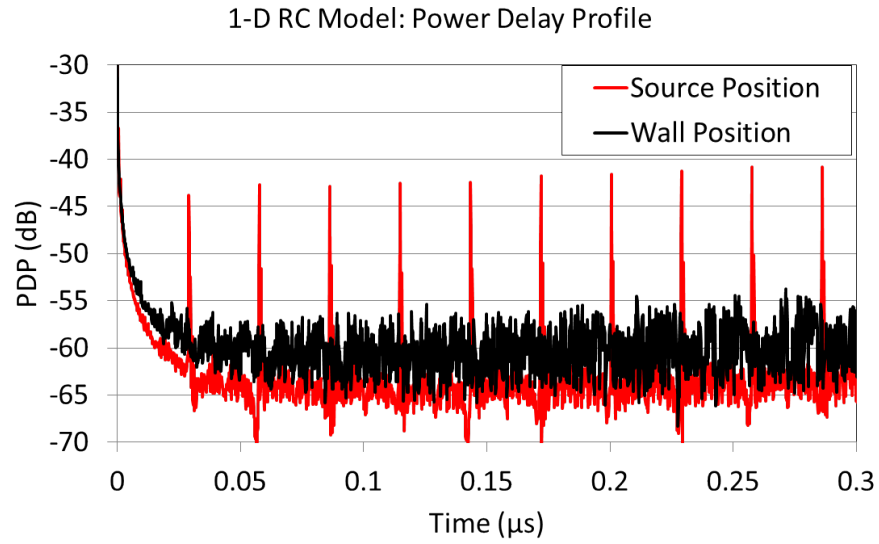
Figure 5.5: These plots show the PDP and E_b from the one-dimensional Green's function RC model for the wall movement and source position movement simulation sets described for Figure 5.3.

5.3   Two-Dimensional Enhanced Backscatter Coefficient

The two-dimensional Green's function RC model adds an additional spatial dimension for wall and source position variation. Electric fields in the two-dimensional RC model with the source along the z-axis as in Figure 5.2, are a sum of TE modes given by (5.15). It is thus expected that responses obtained with the two-dimensional model will have contributions due to multiple modes and will better approximate measured three-dimensional RC behavior than the one-dimensional model. It is hoped that the added dimensional variation and the modal solution to the fields will result in e_b values that are more comparable with measured results than what was observed with the one-dimensional RC model.

The base dimensions for the two-dimensional model are 4.28 m × 3.66 m, which are roughly the width and depth of the large NIST RC. As was done with the one-dimensional model, these dimensions are the minimum chamber width and depth. When wall position stirring is used, the position of the wall is pseudo randomly chosen between the base dimension and 0.3 m larger for each sample, and is repeated for a given number of samples. Wall stirring is implemented by changing the value of the a and b parameters shown in Figure 5.2. Source position stirring is also implemented similarly to the one-dimensional model except that the positions are chosen with pseudo-random x and y coordinates, and are again maintained at a minimum distance of 0.3 m away from the boundaries.

Due to computational limits, only a finite number of modes can be included. The number of modes used in the RC model was chosen by computing the fields for an incrementally increasing number of modes. At each increment the computed fields were compared with those found on the previous run to get a percentage difference between each run. A 1% criterion was set over the frequency range of 100 MHz to 6 GHz, and a pseudo random selection of 100 sample source points were used. This was run several times, resulting in a high number of 280 modes that was then set as the number of modes used in all subsequent two-dimensional RC model runs. There was a difficulty in using this number of modes, in that for low frequencies the contribution of the high

order modes is very small and causes MatLab to give a NaN (Not a Number) character that ruins the computations at those frequencies. To get around this all values that came out as NaN were set to 0. This approximation increases the error of the low frequency data by the sum of the zeroed modes, but this error is expected, and assumed, to be negligibly small.

For the two-dimensional Green's function RC model, two separate simulation sets were run to get the initial S-parameter data. In order to randomize the stirring processes as much as possible, the wall movement and source positions are given in pairs with no repetitions. That is, each sample collected with wall stirring is made with a unique pair of wall positions that are pseudo randomly selected. Likewise, the samples collected by moving the source positions is done with unique pairs of source positions. No wall or source positions were repeated. Data Set 1 was collected with 2996 frequency points, 100 source position pairs, and 100 wall position pairs. Data Set 2 was collected with 59901 frequency points, 20 source position pairs, and 20 wall position pairs. In addition to source position and wall stirring, the data sets were also frequency stirred. The e_b results from these simulations are shown in Figure 5.6.

Comparing the plots of e_b given in Figures 4.1, 5.4, and 5.6 obtained from measurement, the one-dimensional model, and the two-dimensional model, respectively, it is apparent that e_b found using the two-dimensional model looks qualitatively more like the measured results than does the one-dimensional model results. A key difference is that the largest variation in e_b for the two-dimensional model is throughout the middle of the frequency range, while the measured results have more variation at low frequencies. Frequency stirring helps to smooth out the large peaks, and at the upper frequencies the value of e_b is much less variable and averages at around 2.3. For the simple shaped two-dimensional cavity, (4.10) gives $e_b = 2.25$. The maximum number of samples stirred for both simulation sets is 200,000. Simulation set 1 uses 20 frequency points, 100 wall position pairs, and 100 source position pairs, while simulation set 2 uses 500 frequency points, 20 wall position pairs, and 20 source position pairs. Comparing the two simulation sets, it is apparent that the smoothest response is obtained with frequency stirring using a relatively wide bandwidth with many points. With 20 frequency samples for stirring, the results in Figure 5.6(a)
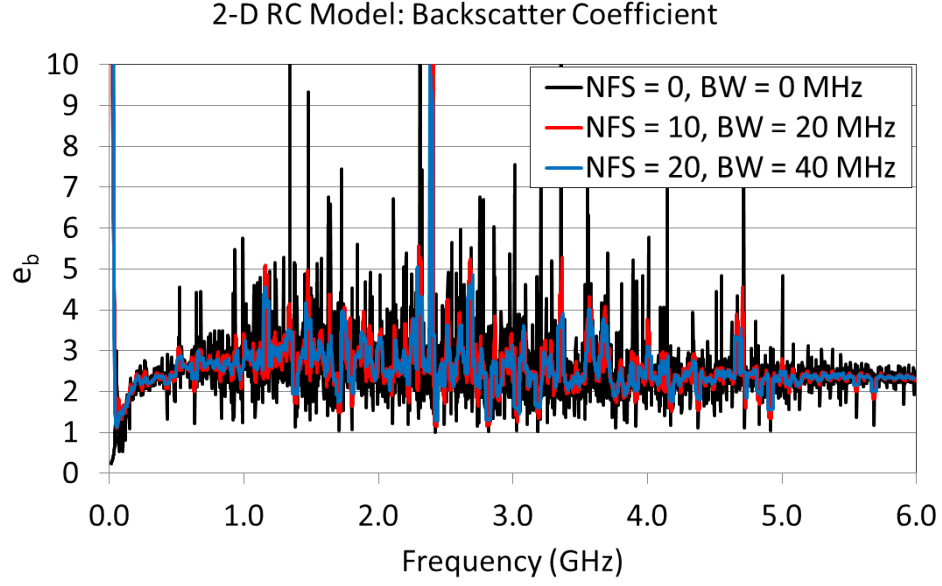
(a) Data Set 1
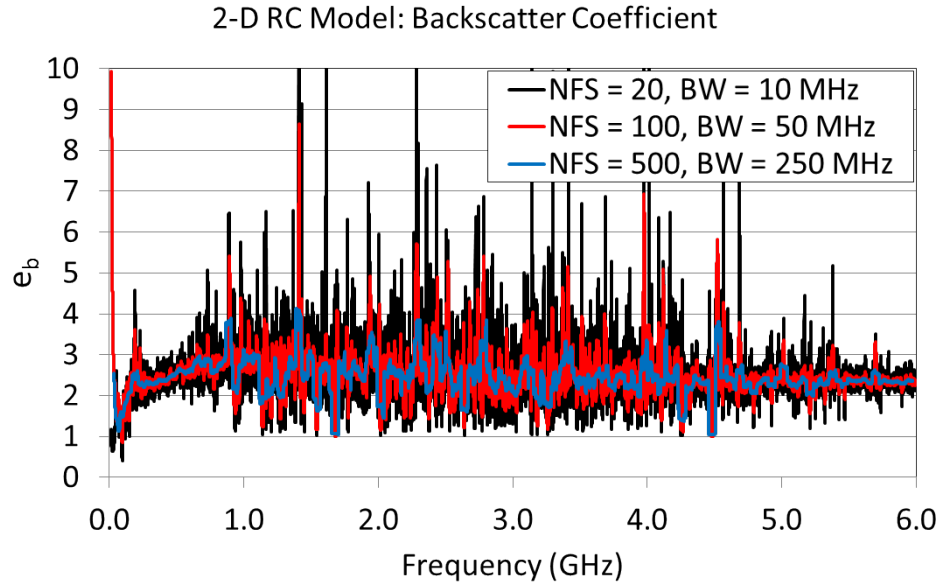
(b) Data Set 2

Figure 5.6: Enhanced backscatter from the two-dimensional Green's function RC model for the two simulation sets. The base dimensions of the model RC were set to 4.28 m x 3.66 m. The frequency range is 10 MHz to 6 GHz. Data Set 1 was collected with 2996 frequency points, 100 source position pairs, and 100 wall position pairs. Data Set 2 was collected with 59901 frequency points, 20 source position pairs, and 20 wall position pairs.

still have sharp peaks, while 500 frequency samples and fewer source and wall positions gives a smoother e_b as shown in Figure 5.6(b).

The PDP results obtained from the one- and two-dimensional models are shown in Figures 5.5(a) and 5.7, respectively. The results from the two-dimensional model do not have the large peaks that occur in the one-dimensional source movement case. Interestingly, all of the modeled PDP results decay at early times, and then reach a minimum and stay relatively constant at that minimum until late times when deviations due to aliasing occur. Given the differences observed in the modeled e_b results versus measurement results, it is not surprising that the PDP also have differences. The simplified geometry of the one- and two-dimensional models do not accurately model the decay profile of a three-dimensional environment. It was thought that potentially the inclusion of wall loss in the two-dimensional model might result in a decay profile more closely matching that of a real world environment, but the results from the current modeling efforts show that this is not the case. From the PDP's obtained in the one- and two-dimensional models, the time-domain enhanced backscatter coefficient was also computed. The results for the one-dimensional model are shown in Figure 5.5(b), and for the two-dimensional model in Figure 5.8. The E_b results for the one-dimensional model have large variations, and a lower limit of around 0.5. For the two-dimensional models, E_b flattens out at a fairly constant value, at around 3 for data set 1 and around 2 for data set 2. In comparing the one- and two-dimensional results it is apparent that the wall loss is necessary for the value of E_b to settle rather than wildly oscillate. It also seems likely that the value of e_b and E_b obtained are related to the correlation between the samples obtained in the various data sets. This analysis is beyond the scope of this thesis and will be left for future investigations.

In the next chapter, the concepts discussed in the previous chapters will be used to characterize a Log-Periodic antenna, and ultimately compute the antenna's total efficiency and provide an estimate for the uncertainty of the measurement.
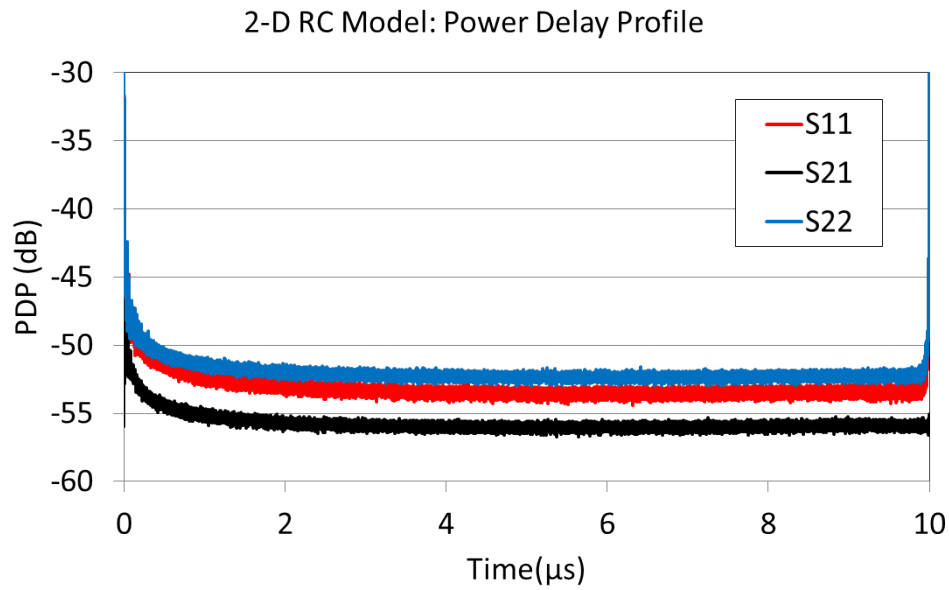
(a) Data Set 1

(b) Data Set 2
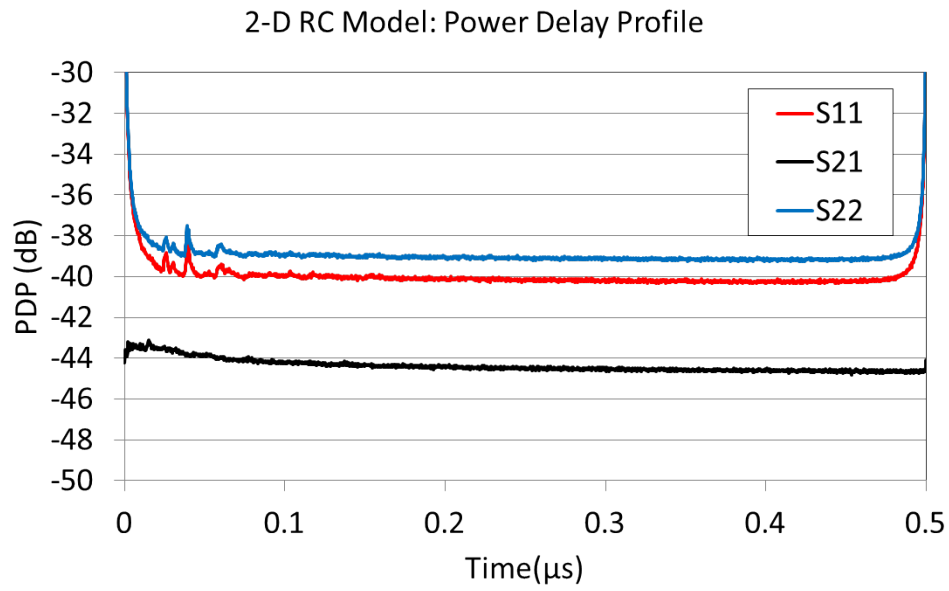
Figure 5.7: PDP from the two-dimensional Green's function RC model for the simulation sets described for Figure 5.6.
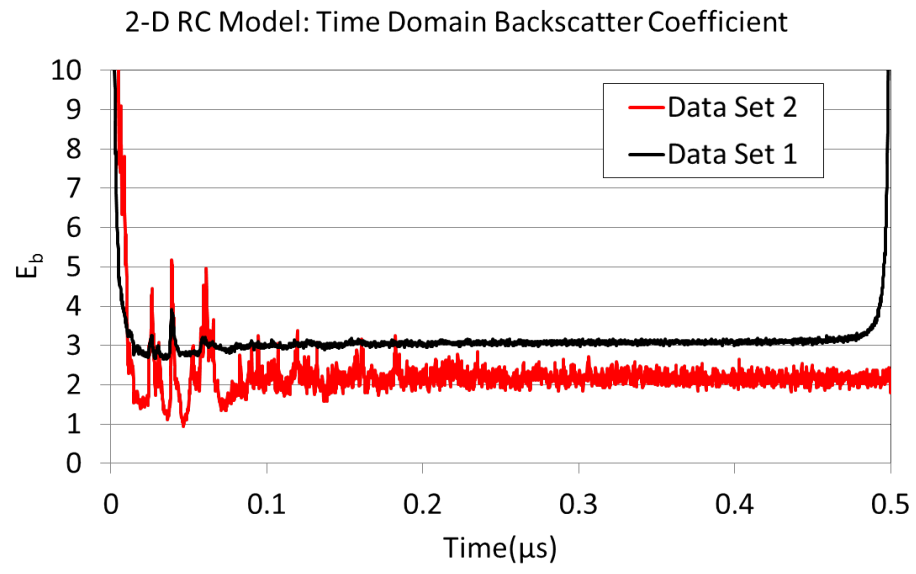
Figure 5.8: Time-domain E_b from the two-dimensional Green's function RC model for the simulation sets described for Figure 5.6.

<center>Chapter 6</center>

<center>Antenna Efficiency Measurements in the Reverberation Chamber</center>

Using many of the various concepts discussed in previous chapters, the total efficiency, $\eta_{T,LP}$, of a Log Periodic (LP) antenna was computed from a two antenna RC test done in the large NIST RC with dimensions 4.28 m x 3.66 m x 2.9 m. The reference antenna is a wire discone antenna, and the measurement was conducted over a frequency range of 100 MHz to 2 GHz, with 32001 frequency samples, and 100 paddle positions. Measurement results are processed using no frequency stirring as well as with 100 frequency sample stirring, corresponding to a 6 MHz bandwidth. A photo of the LP, the wire discone reference, and one other discone type antenna is shown in Figure 6.1. The following shows the computations performed from the measured data that ultimately lead to an estimate of $\eta_{T,LP}$.

The LP antenna was connected to port 1 of the VNA. Using the raw S_{11} data, the reflection coefficient is computed using (B.44) which gives $\langle S_{11} \rangle = \Gamma_{LP}$. The results with and without frequency stirring are shown in Figure 6.2. This data is needed to determine the antenna's reflection efficiency $\eta_{r,LP}$, given by (B.21), to be applied to the total efficiency computation.

The transfer function, S_{21}, between the LP and the reference antenna is required for computing $\sigma^2_{S_{21}}$ which is needed for the e_b computation. The variance of S_{21}, $\sigma^2_{S_{21}}$, is given by (2.35) and the results with and without frequency stirring for the LP to discone antenna data set are shown in Figure 6.3. Included in this plot are also mismatch corrected $\sigma^2_{S_{21}}$ traces given by:

$$\sigma^2_{S_{21},c} = \frac{\sigma^2_{S_{21}}}{1 - |\langle S_{11} \rangle|^2}$$

Figure 6.1: The LP antenna inside the large NIST RC, along with the wire discone reference antenna, and one other discone type antenna.

Figure 6.2: Reflection coefficient of the LP antenna. The Frequency Sample Number (FSN) specifies the amount of frequency stirring done. 100 FSN corresponds to a 6 MHz frequency stirring bandwidth.
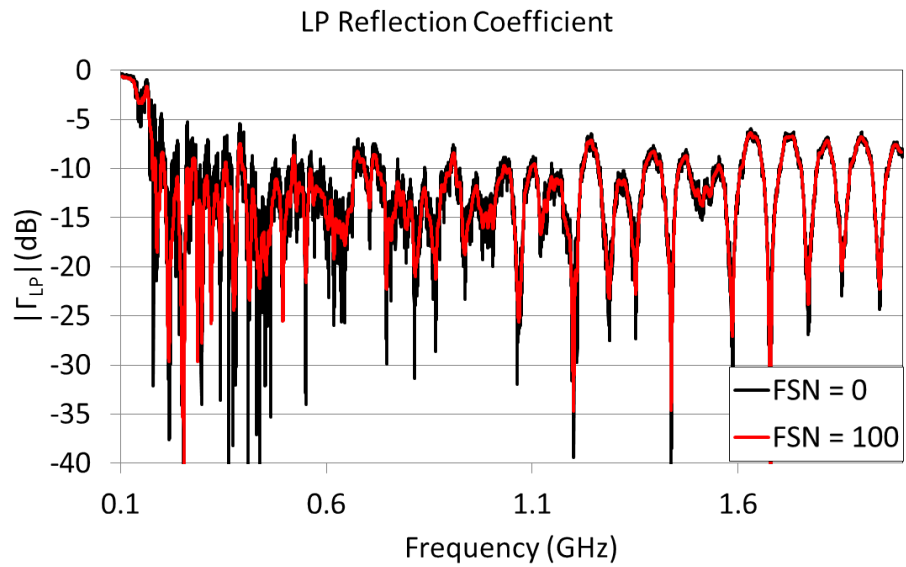
As shown the mismatch corrected traces are more linear on the dB scale at the upper frequencies, corresponding to an exponential decrease in the stirred power with frequency. This exponential decrease with frequency is an expected result, and checking the linearity is a good method of determining the valid frequency range of the measurement. This particular RC is known to work well above 300 MHz. As can be seen from Figure 6.3, there is still some amount of variation above 300 MHz that deviates from a completely linear decrease, although this variation is much smaller than the variation shown at frequencies less than 300 MHz. Another interesting observation to be made from this data is that there is a change in the linear slope at around 1.1 GHz. This change in slope can also be observed in plots of $|\langle S_{21} \rangle|$ which suggests a change in the chamber loss. The cause of this is at low frequencies the dominant loss mechanism is the antenna, but at high frequencies the RC walls take over as the dominant loss mechanism [34]. From the data shown in Figure 6.3(a) the change over from antenna dominant loss to RC dominant loss occurs around 1.1 GHz. Visualization of the different frequency regions of the measured RC data can be enhanced by plotting the data on a logarithmic frequency scale, which has been done with the data shown in Figure 6.3(b).

In addition to $\sigma^2_{S_{21}}$, the reflection variances $\sigma^2_{S_{11}}$ and $\sigma^2_{S_{22}}$ must also be computed in order to compute e_b using (4.9). This computation of e_b was also performed with and without frequency stirring, and the results are shown in Figure 6.4. Using the procedure discussed in Section 4.3, the relative uncertainty of the measurement computed from e_b, $\hat{\tilde{u}}_{e_b}$, is shown in Figure 6.5. From the plots of e_b and $\hat{\tilde{u}}_{e_b}$ it is apparent that frequency stirring gives mixed results. At frequencies less than roughly 300 MHz, frequency stirring greatly increases the error to the point of making any results completely useless. However, at frequencies greater than 300 MHz frequency stirring effectively reduces the error. At 300 MHz $\hat{\tilde{u}}_{e_b}$ is roughly 0.088 while at 2 GHz $\hat{\tilde{u}}_{e_b}$ reduces to roughly 0.027. This decrease in uncertainty is related to the amount of correlation between the collected samples, both in frequency and over different paddle positions [50]. With 100 frequency points and 100 paddle positions the minimum uncertainty is 0.01, which requires all collected samples to be uncorrelated.

(a) Linear Frequency
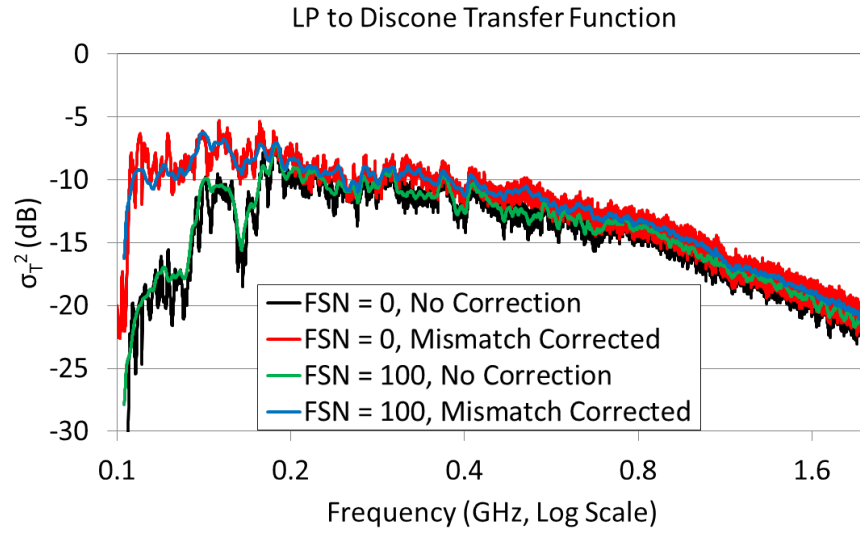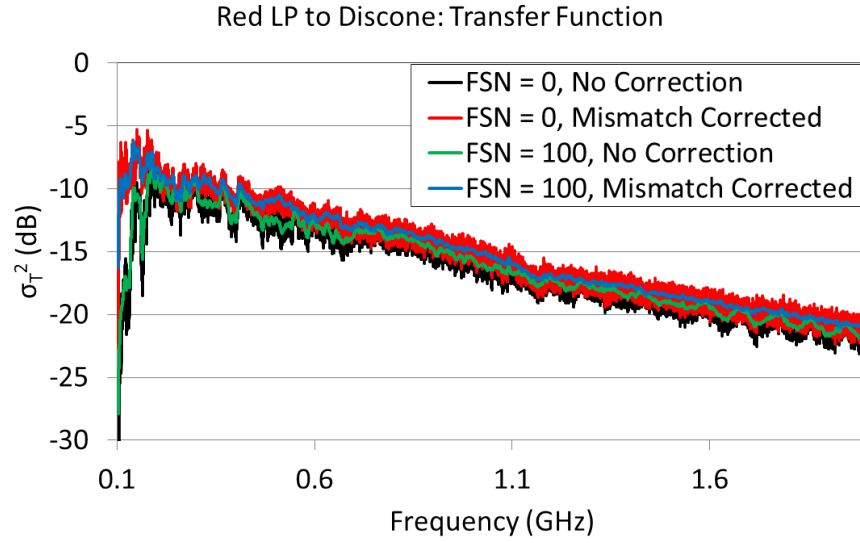
(b) Log Frequency

Figure 6.3: Variance of the transfer function between the LP AUT and the wire discone reference antenna.
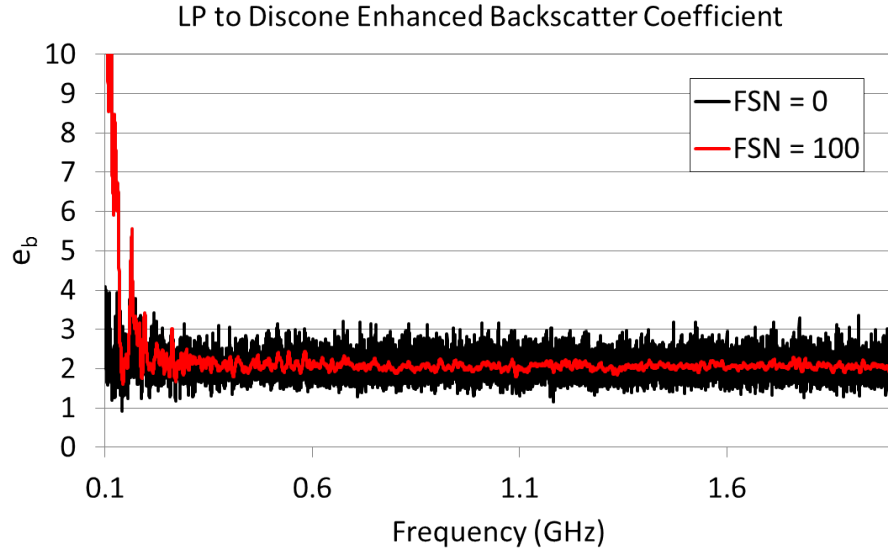
Figure 6.4: e_b computed from the LP AUT and wire discone reference antenna measurement. The Frequency Sample Number (FSN) specifies the amount of frequency stirring done. 100 FSN corresponds to a 6 MHz frequency stirring bandwidth.
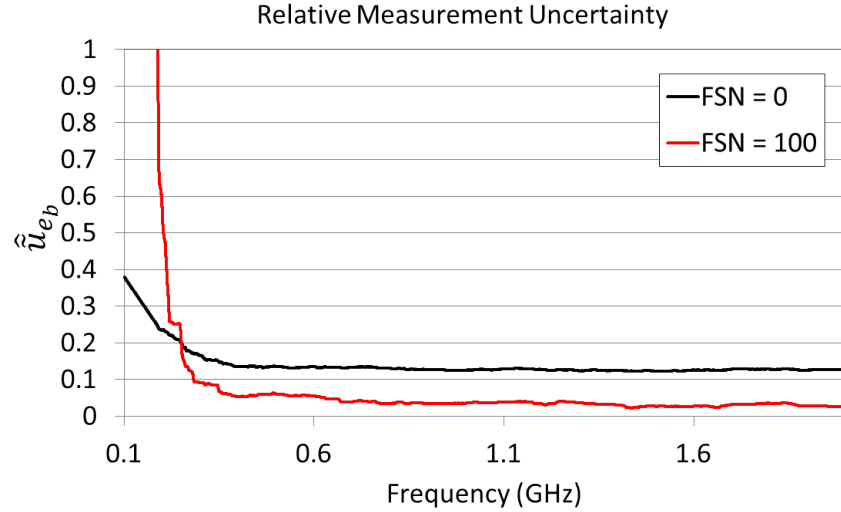
Figure 6.5: Relative uncertainty computed from e_b of the LP AUT and wire discone reference antenna measurement. The Frequency Sample Number (FSN) specifies the amount of frequency stirring done. 100 FSN corresponds to a 6 MHz frequency stirring bandwidth.

The last quantity needed before computing the total efficiency is the radiation efficiency, $\eta_{cd,LP}$, of the LP. There are two methods, currently under investigation at NIST, that can be used to obtain this quantity and will be referred to as the frequency-domain (FD) technique and the time-domain (TD) technique.

6.1 Antenna Radiation Efficiency: Frequency Domain Technique

Following the formulation discussed in [27] for the FD technique, we start with (2.41), $\eta_{cd,LP}$ is given by:

$$\eta_{cd,LP} = \sqrt{\frac{\langle P_{Tx}\rangle}{\langle P_{rf}\rangle}\frac{\sigma^2_{S_{11}}}{(1-|\langle S_{11}\rangle|^2)^2}} \tag{6.1}$$

From (4.1) we have that $\langle P_{rf}\rangle = e_b\langle P_{Rx}\rangle$, and from (2.10) we have that:

$$\frac{\langle P_T\rangle}{\langle P_R\rangle} = \frac{C_{RC}}{Q}$$

In addition, the assumption given by (3.3) gives $Q(\omega) = \tau_{RMS}\omega$, where the procedure for finding τ_{RMS} is discussed in Section 3.3. Recall that finding τ_{RMS} requires computing the PDP over a sliding window of a specified bandwidth in order to obtain τ_{RMS} as a function of frequency. From these various relationships, (6.1) can be re-written as:

$$\eta_{cd,LP} = \sqrt{\frac{C_{RC}}{\omega e_b \tau_{RMS}}\frac{\sigma^2_{S_{11}}}{(1-|\langle S_{11}\rangle|^2)^2}} \tag{6.2}$$

As was done in [27], two methods can be defined from (6.2): a 1 antenna method, and a 2 antenna method. Using the 1 antenna method, the assumption is made that $e_b = 2$. All other terms in (6.2) can be obtained from a single antenna, one port RC reflection measurement using a VNA, and hence is called the 1 antenna method. The computation of e_b from the two port measurement is the only difference between the 2 antenna method and the 1 antenna method.

For the LP and discone antennas, the PDP at several frequencies across the full measurement bandwidth are shown in Figure 6.6(a). Along with the measured PDP data are lines corresponding to the linear fit operation performed to obtain τ_{RMS}. It is once again observed that at low
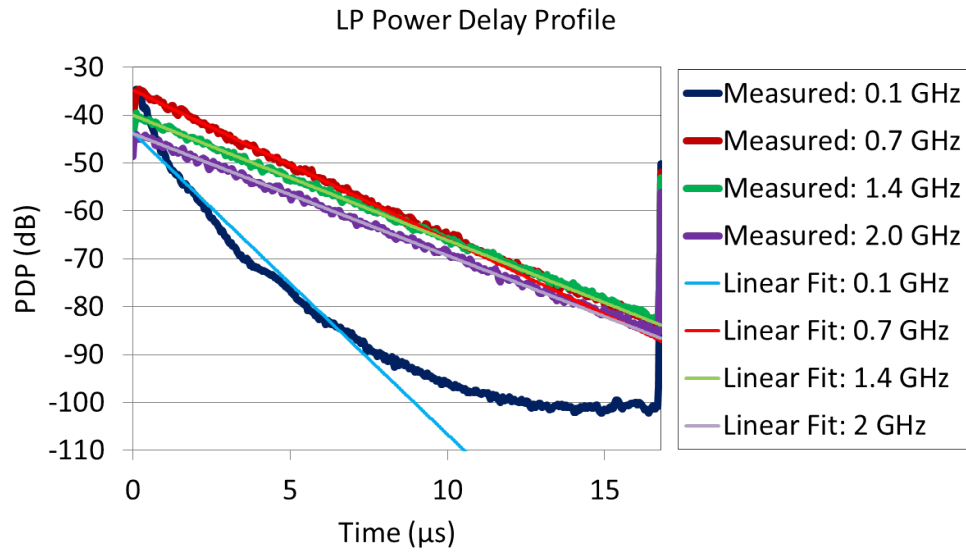
(a) PDP
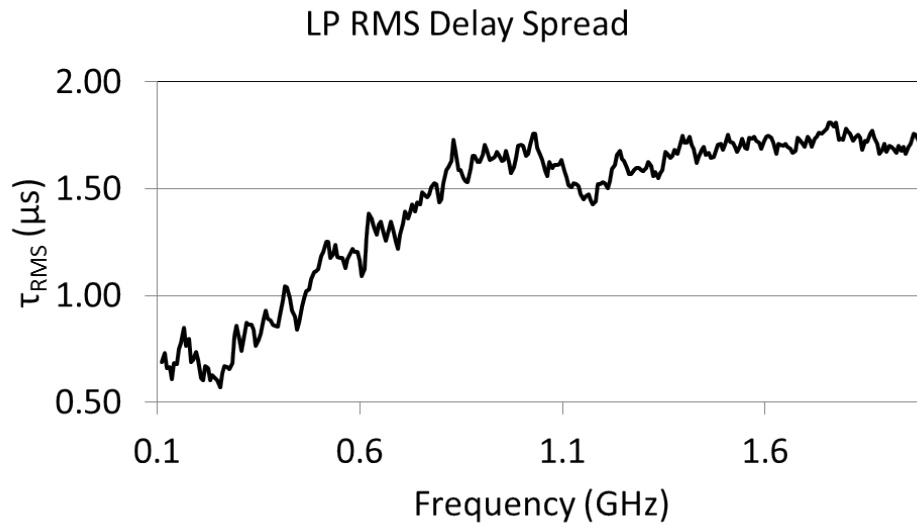
(b) τ_{RMS}

Figure 6.6: Power delay profile and RMS delay spread between the LP AUT and the wire discone reference antenna. The PDP results are computed using 25 MHz bandwidths and are shown at the center frequencies 0.1, 0.7, 1.4, and 2 GHz.

frequencies, the linear approximation does not match the measured data, while at higher frequencies the linear approximation fits the measured data very well. The resulting τ_{RMS} over the full measurement bandwidth is shown in Figure 6.6(b).

6.2 Antenna Radiation Efficiency: Time Domain Technique

The time-domain technique for estimating the radiation efficiency of an antenna is done by making use of the relationship between the $PDP(\tau)$ and the power spectral density $R(\Delta f)$, where Δf and τ denote relative frequency and delay, respectively. In terms of VNA measurements in an RC, $PDP_{RC}(\tau)$ is given by (2.47) and the normalized autocorrelation $\hat{R}_{RC}(\Delta f)$ could be found exactly with multiple infinite-bandwidth realizations of $S_{21}(f)$, measured between antennas 1 and 2, by:

$$\hat{R}_{RC}(\Delta f) = \left\langle \frac{\int_0^\infty S_{21}(f)S_{21}^*(f + \Delta f)df}{\int_0^\infty |S_{21}(f)|^2 df} \right\rangle \tag{6.3}$$

Strictly speaking, (6.3) must be evaluated in the limit as the measurement bandwidth becomes infinite so as to ensure that $\hat{R}_{RC}(0) = 1$.

For a set of $S_{21}(f)$ measurements spanning some finite bandwidth over $f_l \leq f \leq f_u$, the frequency-domain autocorrelation is given by:

$$R_{21}(\Delta f) = \left\langle \int_{f_l}^{f_u} S_{21}(f)S_{21}^*(f + \Delta f)df \right\rangle \tag{6.4}$$

Equation 6.4 defines the autocorrelation of $S_{21}(f)$ multiplied by a rectangular window function spanning the measurement bandwidth. It may be shown that [44]:

$$R_{21}(\Delta f) = P_{BW}\Lambda\left(\frac{\Delta f}{2[f_u - f_l]}\right)\hat{R}_{RC}(\Delta f) \tag{6.5}$$

where

$$\Lambda(x) = \begin{cases} 1 - |x|, & \text{for } |x| \leq 1 \\ 0, & \text{otherwise} \end{cases} \tag{6.6}$$

is the autocorrelation of the implicit rectangular window and $P_{BW} = R_{21}(0)$ is the total power

within the measurement bandwidth as given by:

$$P_{BW} = \int_{f_l}^{f_u} \langle |S_{21}(f)|^2 \rangle \, df \tag{6.7}$$

For a "well-stirred" RC, $\langle |S_{21}(f)|^2 \rangle$ is related to the chamber's quality factor Q by:

$$\langle |S_{21}(f)|^2 \rangle = \frac{Q\lambda^3}{16\pi^2 V} \eta_{cd,1}\eta_{cd,2} \tag{6.8}$$

where V is the chamber's volume, λ is the measurement wavelength, and $\eta_{cd,1}$ and $\eta_{cd,2}$ are the radiation efficiencies of the two antennas. The chamber's quality factor has been shown to be related to the decay constant τ_{RMS} of the chamber's intrinsic power delay spectrum in (6.13) according to (3.2):

$$Q = 2\pi f \tau_{RMS} \tag{6.9}$$

Substituting (6.8) and (6.9) into (6.7) and carrying out the integration yields:

$$P_{BW} = \frac{\tau_{RMS} c^3 \eta_{cd,1}\eta_{cd,2}}{8\pi V} \left[\frac{1}{f_l} - \frac{1}{f_u} \right] \tag{6.10}$$

where c is the speed of light.

It can be observed from Figures 2.10 and 6.6(a) that the PDP measured in the RC decays exponentially at late times after the early time build up. In the following we assume that the decay of the PDP is dominated by a single time constant τ_{RMS} that is related to the composite Q as in (6.9). In addition, it is assumed that this model holds for all time. In making these assumptions, the PDP can be modeled by the decay of a steady state source that is suddenly switched off, given by [21] [26]:

$$PDP_{RC}(\tau) = \begin{cases} P_0 e^{\frac{-\tau}{\tau_{RMS}}}, & \text{for } \tau \geq 0 \\ 0, & \text{otherwise} \end{cases} \tag{6.11}$$

where P_0 is the received power before the source is switched off. A normalized power delay profile $\widehat{PDP}$ can be defined as the ratio of the PDP and the time integral of the PDP as:

$$\widehat{PDP} = \frac{PDP}{\int_0^\infty PDP d\tau} \tag{6.12}$$

Normalizing (6.11) we get:

$$\widehat{PDP}_{RC}(\tau) = \begin{cases} \frac{1}{\tau_{RMS}} e^{\frac{-\tau}{\tau_{RMS}}}, & \text{for } \tau \geq 0 \\ \\ 0, & \text{otherwise} \end{cases} \tag{6.13}$$

Making use of the Wiener-Khinchin theorem, (A.17) and (A.18), $\hat{R}_{RC}(\Delta f)$ is found by taking the Fourier transform of (6.13) to give:

$$\hat{R}_{RC}(\Delta f) = \frac{1}{1 + j2\pi\Delta f \tau_{RMS}} \tag{6.14}$$

Again, using the Wiener-Khinchin and convolution theorems, we can relate the power delay profile $PDP_{21}(\tau)$ of a set of band-limited $S_{21}(f)$ measurements to the Fourier transform of the band-limited frequency domain autocorrelation given by (6.5):

$$PDP_{21}(\tau) = \mathcal{F}\{R_{21}(\Delta f)\} = P_{BW}(2[f_u - f_l])^2 \text{sinc}^2(2\pi[f_u - f_l]\tau) \otimes \widehat{PDP}_{RC}(\tau) \tag{6.15}$$

where $\text{sinc}^2(\pi x)$ corresponds to the Fourier transform of $\Lambda(\xi)$, and $\otimes$ denotes convolution. Provided that the measurement bandwidth given by $f_u - f_l$ is sufficiently large, we expect that:

$$PDP_{21}(\tau) \approx P_{BW}\widehat{PDP}_{RC}(\tau) \tag{6.16}$$

More precisely, provided that $[f_u - f_l]\tau_{RMS} \gg 1$, then for $\tau \gg \frac{1}{[f_u - f_l]}$, $PDP_{21}(\tau)$ is asymptotically given by:

$$PDP_{21}(\tau) \sim P_{BW}\widehat{PDP}_{RC}(\tau) \tag{6.17}$$

By defining

$$PDP_{RC}(\tau) = \frac{c^3}{8\pi V}\left[\frac{1}{f_l} - \frac{1}{f_u}\right] e^{\frac{-\tau}{\tau_{RMS}}} \tag{6.18}$$

as the bandwidth-dependent PDP corresponding to an RC measurement using ideal lossless antennas, we may use (6.17) to express the asymptotic behavior of the observed delay spectrum for $S_{21}(f)$ as:

$$PDP_{21}(\tau) \sim \eta_{cd,1}\eta_{cd,2}PDP_{RC}(\tau) \tag{6.19}$$

The formulation may also be applied to the power delay profile, $PDP_{11}(\tau)$, observed for a set of $S_{11}(f)$ measurements on antenna 1, by noting that $PDP_{11}(\tau)$ only involves antenna 1 as both transmitter and receiver. To use the formulation of (6.19), the product $\eta_{cd,1}\eta_{cd,2}$ must be replaced by $\eta_{cd,1}^2$. Additionally, PDP_{RC} in (6.19) must be scaled by a factor of E_b so as to account for the RC's enhanced backscatter effect. Making these adjustments to (6.19) to accommodate the differences between PDP_{21} and PDP_{11} result in:

$$PDP_{11}(\tau) \sim E_b \eta_{cd,1}^2 PDP_{RC}(\tau) \tag{6.20}$$

The asymptotic behavior of the PDP given in (6.19) and (6.20) provides a means for determining the efficiencies of the measurement antennas via linear regression. Consider the logarithm of (6.20), given by:

$$\ln PDP_{11}(\tau) \sim -\frac{\tau}{\tau_{RMS}} + \ln\left(E_b \eta_{cd,1}^2 \frac{c^3}{8\pi V}\left[\frac{1}{f_l} - \frac{1}{f_u}\right]\right) = -\frac{\tau}{\tau_{RMS}} + \ln(P_0) \tag{6.21}$$

where (6.18) has been substituted for $PDP_{RC}(\tau)$. From inspection of (6.21), it can be observed that fitting a linear equation to $\ln PDP_{11}(\tau)$ allows $\eta_{cd,1}$ to be determined from the constant term $\ln(P_0)$. Taking the exponential of $\ln(P_0)$ we get:

$$P_0 = E_b \eta_{cd,1}^2 \frac{c^3}{8\pi V}\left[\frac{1}{f_l} - \frac{1}{f_u}\right] \tag{6.22}$$

Finally, by solving (6.22) for $\eta_{cd,1}$ we get:

$$\eta_{cd,1}^{TD} = \sqrt{\frac{8\pi V}{c^3}\frac{P_0}{E_b}\frac{f_l f_u}{f_l - f_u}} \tag{6.23}$$

Since the LP antenna was measured on port 1, we have that $\eta_{cd,LP} = \eta_{cd,1}$. The radiation efficiency found using the time domain technique also has 1 and 2 antenna versions. Again, the 1 antenna version is performed by simply assuming that $E_b = 2$, while the two antenna method requires the computation of E_b.

6.3 Log Periodic Efficiency Results

Multiplying $\eta_{cd,LP}$ and $\eta_{r,LP}$ gives the total efficiency $\eta_{T,LP}$. The radiation and total efficiencies of the LP, using the frequency-domain and time-domain techniques, and 1 antenna and

2 antenna methods for each technique, are shown in Figure 6.7. It is expected that the radiation efficiency changes slowly with frequency over the specified operating range of the LP, 0.1 to 2 GHz. The observed relatively sharp decrease in radiation efficiency at low frequencies is an indication that all of the RC techniques fail to accurately estimate the radiation efficiency at those frequencies. The under-estimated efficiency is attributed to the poor performance of the RC at frequencies less than the cutoff. Furthermore, this decrease in the radiation efficiency occurs at a lower frequency for the frequency-domain technique, than does the time-domain technique. However, above 500 MHz all of the methods result in similar predicted values of the radiation efficiency. The total efficiency of the LP was presented in [28], and was compared against results from an anechoic chamber facility. The results from the anechoic chamber total efficiency measurements are also included in Figure 6.7(b) along with the RC measurement results. For the total efficiency, the RC and anechoic results have good agreement above roughly 650 MHz. At low frequencies, the RC results once again under-estimate the total efficiency, while the anechoic chamber measurements produce an over-estimation of the total efficiency. In the case of the anechoic chamber, the low frequency cutoff is governed by the reflection from the RF absorber lined walls. As frequency decreases, the reflection from the absorber increases.

The RC and anechoic chamber results shown in Figure 6.7(b) were also given in Figure 8 of [28]. However, one may notice that the RC results presented in [28] are different than those shown in Figure 6.7(b). While both plots were obtained from the same data set the two results were computed using different sliding window bandwidths for the τ_{RMS} computation. The bandwidth chosen for the results in [28] was 100 MHz. In addition, it can be observed that Γ_{LP} in Figure 6.2 has large oscillations at the upper frequencies with sharp nulls that are roughly 100 MHz apart. Including too much of this oscillation due to antenna mismatch adversely affects the exponential decay of the PDP, which in turn changes the value of τ_{RMS} obtained. As a result, a frequency span of 25 MHz was chosen as a compromise between reducing the inclusion of Γ_{LP} oscillation, and having a wide enough bandwidth to give meaningful results since narrower frequency bandwidths increase the time step of the PDP. By reducing the computation bandwidth, the results in Figures 6.7(b)

LP Radiation Efficiency

(a) Radiation Efficiency
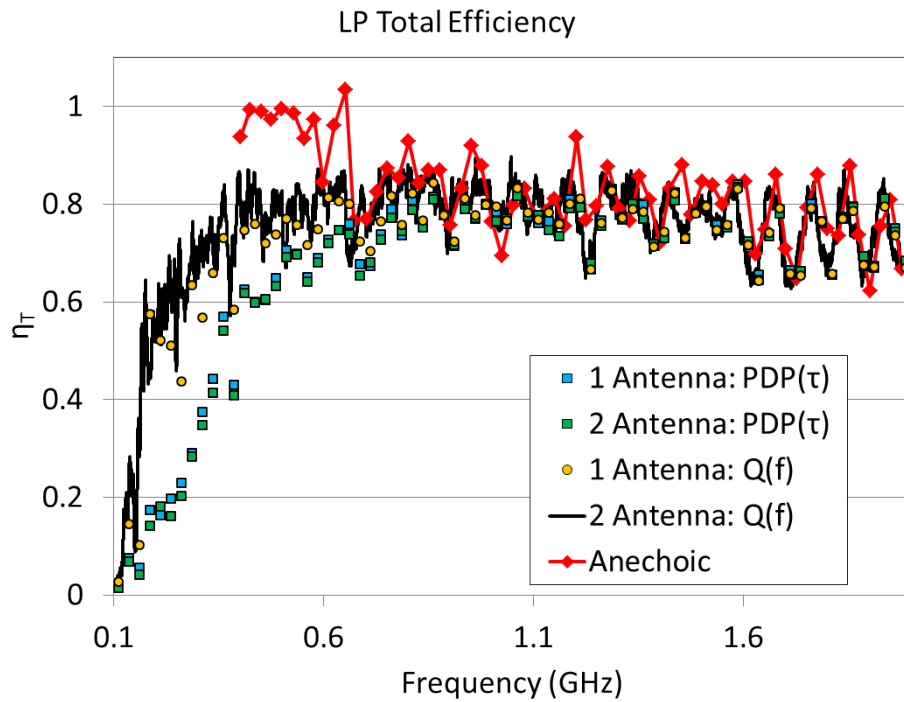
LP Total Efficiency
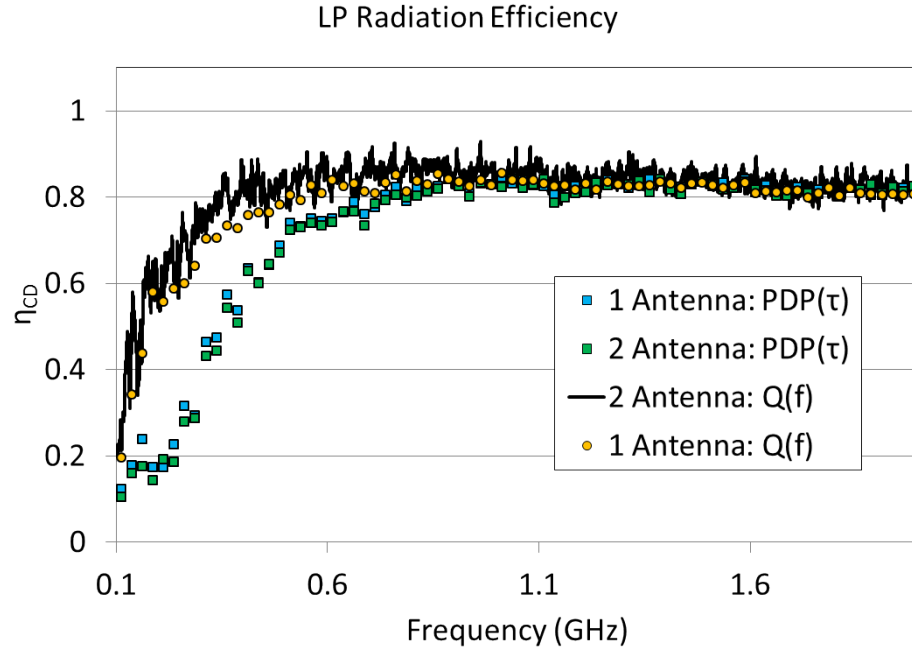
(b) Total Efficiency

Figure 6.7: Total and radiation efficiency of the LP antenna computed using the frequency-domain and time-domain techniques, as well as 1 antenna and 2 antenna methods for each technique. In addition, the total efficiency is compared with measurements done using an anechoic chamber.

have better agreement in the upper frequency range, above 1 GHz, between the RC and anechoic measurement environments.

Using the concepts presented in earlier chapters and data collected from a two port RC measurement, the steps required in obtaining the total efficiency of the LP antenna have been shown. Along with the estimation of $\eta_{T,LP}$, the single configuration uncertainty estimation method can be used to provide a measure of confidence in the computed $\eta_{T,LP}$ results done using the frequency-domain technique. Following similar arguments made in [27], the mean squared terms e_b, $\sigma^2_{S_{11}}$, and $|\langle S_{11}\rangle|^2$ from (6.2) should have similar relative uncertainty. Thus, the single configuration relative uncertainty estimate, $\hat{\tilde{u}}_{e_b}$ (that was obtained from e_b), shown in Figure 6.5 is used to estimate the uncertainty of the different mean squared terms and is used in equation 2.53 along with e_b, $\sigma^2_{S_{11}}$, and $|\langle S_{11}\rangle|^2$ to obtain standard uncertainty estimates for each of those terms. The other term in (6.2) that can vary with RC spatial dependence is τ_{RMS}. The uncertainty of this must be found using a multiple configuration measurement, which has not been done with this specific data set. However, the relative uncertainty of τ_{RMS} for the same RC is given in [27] with a rough value of 0.007. The standard uncertainty computed from these different terms can be entered into (6.2) to give the confidence interval $\eta_{cd,LP,CI}$, given by:

$$\eta_{cd,LP,CI} = \sqrt{\frac{C_{RC}}{\omega(e_b \mp \hat{\tilde{u}}_{e_b}e_b)(\tau_{RMS} \mp 0.007\tau_{RMS})} \frac{\sigma^2_{S_{11}} \pm \hat{\tilde{u}}_{e_b}\sigma^2_{S_{11}}}{(1 - (|\langle S_{11}\rangle|^2 \pm \hat{\tilde{u}}_{e_b}|\langle S_{11}\rangle|^2))^2}} \qquad (6.24)$$

For the LP antenna data, the confidence interval is shown for the radiation efficiency and total efficiency in Figure 6.8.
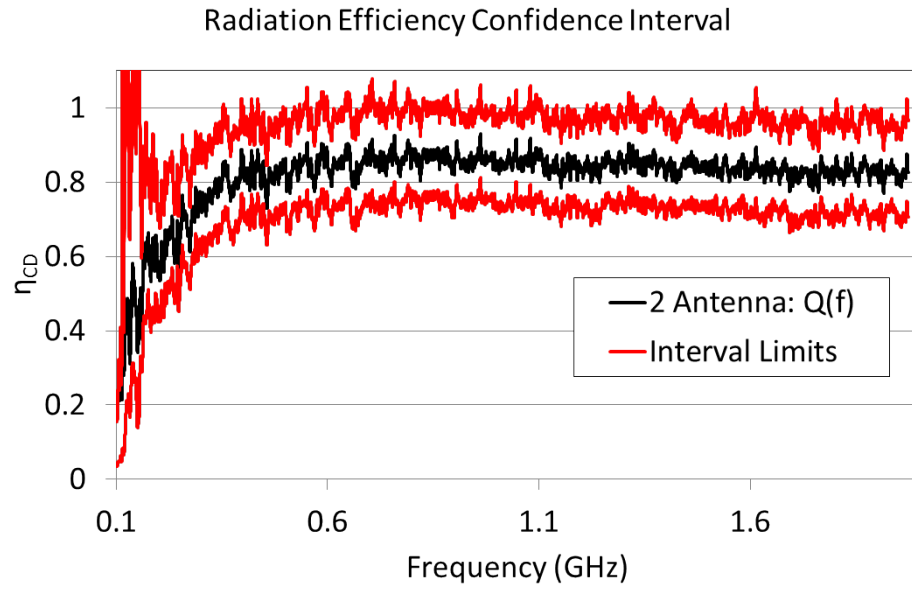
(a) Radiation Efficiency Confidence Interval
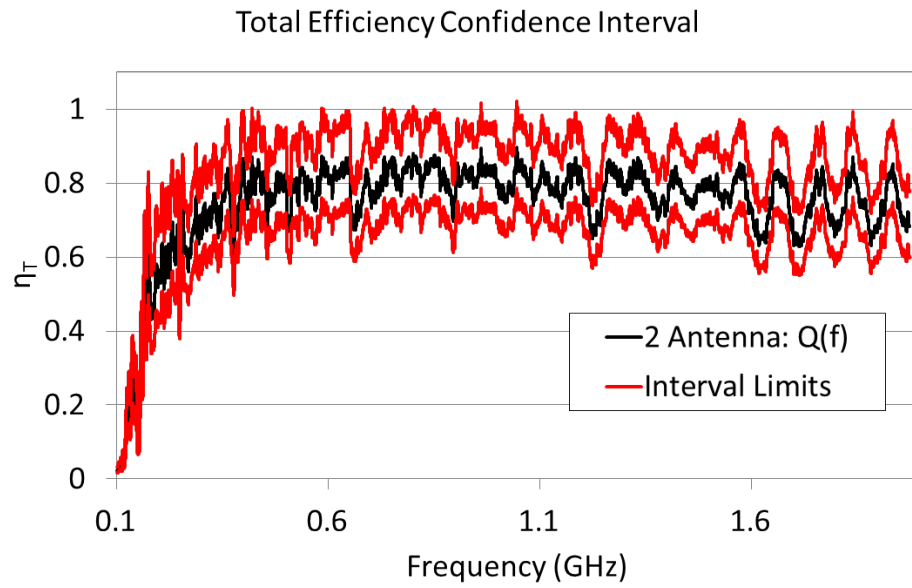
(b) Total Efficiency Confidence Interval

Figure 6.8: Confidence interval for the total and radiation efficiency results of the LP antenna computed using the frequency-domain technique.

Chapter 7

Conclusion

The topic explored in this thesis has been the use of the enhanced backscatter coefficient measurements taken in a reverberation chamber to obtain the relative uncertainty caused by the spatial dependence. In chapter 1, an overview of the RC was given that compared it to other types of measurement facilities and discusses the advantages and limitations of the RC. Of particular concern is the statistical distribution of samples measured in the RC, which has been shown to be related to the frequency of operation, the relative size of the RC and of the internal objects, and the effectiveness of the stirring method employed. In chapter 2, background theory was provided in order to facilitate the formulation of the RC characterization and analysis techniques used in the later parts of the thesis. Chapter 3 followed with a discussion of three methods for characterizing the behavior of the RC: the probability density function, the standard deviation of $\sigma_{\mathcal{T}}^2$ measured at many positions in the RC, and the power delay profile. These methods were used on example data sets to compare and contrast how the results vary under different conditions. Using measurements of transfer function $\sigma_{\mathcal{T}}^2$ at multiple positions an estimate of the relative uncertainty of the chamber for different configurations was given and termed $\hat{\hat{u}}_{\sigma_{\mathcal{T}}^2}$.

In chapter 4, the formulation of the enhanced backscatter coefficient, e_b, from two port S-parameter data was given. It was then shown that the computations of e_b can take the place of $\sigma_{\mathcal{T}}^2$ in a multiple antenna configuration/position measurement for computing the relative uncertainty of the RC, resulting in $\hat{\hat{u}}_{e_b}$. It was found that $\hat{\hat{u}}_{e_b}$ was slightly higher than $\hat{\hat{u}}_{\sigma_{\mathcal{T}}^2}$ for the cases shown. Many computations require the transmission and reflection data, so the advantage of $\hat{\hat{u}}_{e_b}$ is that

it includes $\sigma_{\mathcal{R}}^2$ for each antenna, in addition to $\sigma_{\mathcal{T}}^2$, meaning that the relative uncertainty obtained using e_b is more complete.

More importantly, in chapter 4 it was also shown that the variation of e_b over a relatively small bandwidth of frequencies, using a single configuration measurement, can be used to give nearly the same value of uncertainty as was obtained with the multiple configuration measurement. This is an extremely useful result. It means that the uncertainty of the RC facility can be estimated for every multi-port measurement conducted, which includes many of the cases for which it would be difficult to implement the multiple configuration measurement technique. The RC is a general purpose EM measurement facility and can be operated in many different configurations. Different amounts of RF absorber can be added to approximate the power delay profile of a real world environment. Large electronics that violate the electrically small criteria could be placed in the cavity of the RC to be tested. These things are done because while they violate basic assumptions made in RC measurement analysis, the uncertainty that is introduced can be within acceptable limits. Using the RC in these ways has a definite effect on the spatial uniformity of the RC. Using the single configuration uncertainty estimation technique, the uncertainty of any of these measurements can be estimated directly, rather than relying on uncertainty estimates taken under more idealized conditions.

Additionally, at the end of chapter 4, results from several different measurement data sets were presented in which a value of e_b obtained was different than the theoretical ideal value of 2. One cause was found to be attributable to errors in the VNA calibration. By observing the e_b results it was obvious that there was a problem with the measurement, whereas the $|\langle S_{11} \rangle|$ plot from the same data set did not show any obviously incorrect results. After subsequent measurements it was determined that a slight imperfection in the feed cable connector caused the calibration issue, which showed up as a small amount of excess noise in the $|\langle S_{11} \rangle|$ results. However, the e_b results had a much larger discrepancy in magnitude and were non-linear with frequency, both of which are much clearer indications of a problem and do not require subsequent measurements to know that something went wrong. This is valuable information to have because it gives a quick way to check

the quality of the measurement. Once a solution to the problem is implemented, e_b again gives a relatively quick comparison to determine if the solution fixed the issue.

It was additionally shown that high gain antennas pointed at the paddle in the RC also increase the value of e_b. This increase in e_b appears to be a function of how well the antenna's radiation is focused on the paddle. For standard gain horns, the gain of the antenna increases with frequency, so when the horn is pointed at the paddle, e_b has an increasing slope with frequency. An attempt was made to determine the change in e_b measured in the RC by taking the ratio of the radiated power focused on the paddle to the total radiated power. This quantity was termed the paddle coverage factor, CF, and was shown to have similarities in its behavior as the antennas focus on the paddle was changed by increasing its distance. However, the overall amount of change predicted by CF is far greater than how much e_b changes. A model paddle was built and placed in the anechoic chamber and the RC to compare the interaction between the antenna and the paddle inside both environments for varying antenna pointing directions. It was observed that over the low frequency portion of the full test bandwidth, $\sigma_{\mathcal{R}}^2$ in the anechoic chamber changes by a similar amount as CF does when the antenna pointing direction is changed from pointing directly at the center of the paddle to $40°$ rotated away from center. Thus, CF has reasonably good agreement when only a single paddle reflection is measured, but in the RC the waves reflect many times and the change in $\sigma_{\mathcal{R}}^2$ is much less than CF. In formulating CF the total maximum width of the paddle was used. Potentially an effective area of the paddle inside the RC is needed to correctly predict the change in e_b when a high gain antenna is pointed at a paddle.

In chapter 5, the one- and two-dimensional RC models based on Green's functions of a source within a bounded cavity were derived and used to predict the value of e_b for different types of parameter variation. It was shown that the one-dimensional model gives different values of e_b depending on the type of variation employed. Of those tested, frequency stirring in the one-dimensional model had the largest fluctuation in the results, having a minimum value of 1 with sharp periodic peaks, while source position variation gives an average value near 0.5 with small fluctuations, and wall variation resulted in a constant value of 1. This type of behavior may be

expected at very low frequencies in the RC, but the one-dimensional model does not produce results similar to the RC at frequencies with large mode density.

The two-dimensional RC model is written in terms of the TE modes, and appears to give results more similar to an actual RC. The similarity in results however is achieved by mixing the source position movement, wall position movement, and frequency stirring techniques at the same time. When this was done, the value of e_b obtained from the model is roughly 2.3. However, using the stirring techniques separately the value of e_b fluctuates rapidly with sharp and randomly distributed peaks and nulls. The PDP for these models showed a sharp and short decrease in value at early times, then a fairly constant value up to late times when aliasing errors again increase the value. It is apparent that the PDP in these models does not decay exponentially with time as would be expected in a real RC. The time-domain enhanced backscatter coefficient E_b resulted in a value of 2.3 at late times for the case that also resulted in small oscillation about 2.3 in the frequency domain, once enough frequency stirring was applied. However, the case that resulted in more oscillation in the value of e_b resulted in a late time value of E_b around 3. What these models show is that values of e_b much larger or smaller than 2 are caused by relatively high correlation between the stirred samples. Decorrelation between samples is most effectively achieved in the models by frequency stirring over very large bandwidths, which is only allowable due to the ideal nature of the sources. Potentially, a more accurate paddle coverage factor would need to relate the increase in correlation between samples when the antenna is pointed at the paddle.

In chapter 6, many of the concepts formulated and discussed in earlier chapters were used to compute the total efficiency of a log periodic antenna. The efficiency estimation results were compared with results from another RC and an anechoic chamber. It was shown that using a 25 MHz bandwidth window to obtain τ_{RMS} in the efficiency computation produced total efficiency results that appear to be consistent with anechoic chamber measurement results. Included with these results was the first applied use of the single configuration uncertainty estimation method using the enhanced backscatter coefficient for obtaining the confidence interval of the efficiency estimations. The relative uncertainty of the measurement is close to 0.12 at frequencies above 300

MHz, the known low frequency cutoff of the RC. This is a reasonable estimation of uncertainty since the minimum possible uncertainty for 100 samples is 0.1 for perfectly uncorrelated samples.

It has been shown that the enhanced backscatter coefficient is a useful quantity for characterization of the reverberation chamber. By observing the variation of e_b over multiple antenna configurations, the RC spatial variation can be determined in a similar manner to transfer function variation. In addition, the variation of e_b as a function of frequency can be used to determine the spatial variation for a single-measurement-configuration. It is noted that relatively wide bandwidths were needed to obtain similar standard deviations between the single- and multiple-configuration methods. The widest bandwidth used for the single-configuration method, 128 MHz, resulted in very good agreement between the single- and multiple-configuration relative uncertainty estimates, for all cases tested. Given the dimensions of the RC used, a cube with 3 m sides is a reasonable estimate for the working volume, and 100 MHz corresponds to a wavelength of 3 m. More test cases are needed over different frequency ranges, but it is not unreasonable to assume that the variation of e_b over frequency corresponds to the spatial variation of antennas within the working volume of the RC. This also gives a means for testing if the antennas are located within the working volume. In addition to estimating where the working volume is and the standard deviation caused by spatial non-uniformity, the value of e_b itself can also be used as a benchmark by which to determine if a measurement was completed correctly, or if something corrupted the data. It has been shown that the value can be very sensitive to calibration and frequency stirring issues. However, it is unknown if the increase in the value of e_b obtained from pointing high gain antennas at the paddle has any negative effects on the results computed from measured data. If the increase in the value of e_b does not represent an increase in correlation between samples, then the new value simply needs to be recorded for input into relevant computations such as antenna efficiency.

My personal contributions to this work are as follows. I performed the measurements for all of the data shown, except that collected in Experiment 1. I wrote the code for, and performed nearly all of the computations that have been presented. I additionally conceived of the test to compare the paddle coverage factor in anechoic and reverb environments, as well as constructed the monopole

and model paddles. Collected from the various sources cited in this thesis, I compiled the large list of theoretical analysis formulations and techniques required to perform the computations presented. I conducted many experiments to explore the value of e_b in support of its use as a quantity to use for RC characterization. The initial assumption was that the value of the enhanced backscatter could be used to characterize the statistical behavior of the RC. However, I hypothesized that the variation in e_b over frequency could be used to directly obtain the standard deviation caused by the spatial dependence of the RC. A key characteristic that makes it particularly well suited for this purpose is that it is theoretically a constant, which means that variations in its value over frequency can be used to estimate the RC's spatial non-uniformity. In support of this theory, I reprocessed the data collected for Experiment 1 to show that the variation of e_b over-frequency and over-measurement-position both result in similar values of standard deviation. Based on observations of power delay profiles, I proposed the definition of the time domain enhanced backscatter coefficient, E_b, which has been shown to have similar features to e_b. Furthermore, I wrote the code for, and designed the experiments implemented in, the one- and two-dimensional RC models used for exploring the value of e_b in a simplified environment.

Bibliography

[1] Anechoic Chamber at Ohio University's Avionics Engineering Center, October 2013.

[2] J. Appel-Hansen. "Reflectivity Level of Radio Anechoic Chambers". IEEE Transactions on Antennas and Propagation, AP-21(4):490 – 498, July 1973.

[3] C. A. Balanis. Antenna Theory Analysis and Design. New York, NY, John Wiley & Sons, 3rd edition, 2005.

[4] P. A. Bello and B. D. Nelin. "The Effect of Frequency Selective Fading on the Binary Error Probabilities of Incoherent and Differentially Coherent Matched Filter Receivers". IEEE Transactions on Communication Systems, 11:170 – 186, June 1963.

[5] N. Boriraksantikul. A TEM Cell Design to Study Electromagnetic Radiation Exposure From Cellular Phones. PhD thesis, University of Missouri, August 2008.

[6] U. Carlberg, P.-S. Kildal, and J. Carlsson. "Study of Antennas in Reverberation Chamber Using Method of Moments With Cavity Green's Function Calculated by Ewald Summation". IEEE Transactions on Electromagnetic Compatibility, 47(4):805 – 814, November 2005.

[7] C. Catheline, T. Gallot, P. Roux, G. Ribay, and J. Rosny. "Coherent Backscattering Enhancement in Cavities The Simple-Shape Cavity Revisited". Wave Motion, 48:214 – 222, 2011.

[8] D. C. Chang, B. H. Liu, and M. T. Ma. "Eigenmodes and Composite Quality Factor of a Reverberation Chamber". In NIST Technical Note 1066. National Institute of Standards and Technology, August 1983.

[9] X. Chen, P.-S. Kildal, and S.-H. Lai. "Estimation of Average Rician K-Factor and Average Mode Bandwidth in Loaded Reverberation Chamber". IEEE Antennas and Wireless Propagation Letters, 10:1437 – 1440, 2011.

[10] J. Chuang. "The Effects of Time Delay Spread on Portable Radio Communications Channels with Digital Modulation". IEEE Journal on Selected Areas in Communications, SAC-5(5):879 – 889, June 1987.

[11] J. D. Coder, J. M. Ladbury, and M. Golkowski. "On Lower Bound Antenna Efficiency Measurements in a Reverberation Chamber". In IEEE International Symposium in Electromagnetic Compatibility, pages 216 – 221, 2012.

[12] P. Corona, G. Ferrara, and M. Migliaccio. "Reverberating Chamber Electromagnetic Field in Presence of an Unstirred Component". IEEE Transactions on Electromagnetic Compatibility, 42(2):111 – 115, May 2000.

[13] P. Corona, J. Ladbury, and G. Latmiral. "Reverberation-Chamber Research - Then and Now: A Review of Early Work and Comparison With Current Understanding". IEEE Transactions on Electromagnetic Compatibility, 44(1):87 – 94, February 2002.

[14] D. G. Dudley. Mathematical Foundations for Electromagnetic Theory. New York, NY, John Wiley & Sons, 1994.

[15] C. R. Dunlap, C. L. Holloway, R. J. Pirkl, J. Ladbury, E. F. Kuester, D. A. Hill, and S. van de Beek. "Characterizing Reverberation Chambers by Measurements of the Enhanced Backscatter Coefficient". In IEEE International Symposium on Electromagnetic Compatibilty, pages 210 – 215, 2012.

[16] W. H. Emerson. "Electromagnetic Wave Absorbers and Anechoic Chambers Through the Years". IEEE Transactions on Antennas and Propagation, AP-21(4):484 – 490, July 1973.

[17] G. Ferrara, M. Migliaccio, and A. Sorrentino. "Characterization of GSM Non-Line-of-Sight Propagation Channels Generated in a Reverberating Chamber by Using Bit Error Rates". IEEE Transactions on Electromagnetic Compatibility, 49(3):467 – 473, August 2007.

[18] G. J. Freyer, M. O. Hatfield, D. M. Johnson, and M. B. Slocum. "Comparison of Measured and Theoretical Statistical Parameters of Complex Cavities". In IEEE International Symposium on Electromagnetic Compatibility Symposium Record, pages 250 – 253, 1996.

[19] E Genender, C. L. Holloway, K. A. Remley, J. Ladbury, G. Koepke, and H. Garbe. "Simulating the Multipath Channel with a Reverberation Chamber: Application to Bit Error Rate Measurement". IEEE Transactions on Electromagnetic Compatibility, 52(4):766 – 777, November 2010.

[20] L. H. Hemming. Electromagnetic Anechoic Chambers: A Fundamental Design and Specification Guide. New York, NY, IEEE Press, 2002.

[21] D. A. Hill. Electromagnetic Fields in Cavities: Deterministic and Statistical Theories. New York, NY, IEEE Press, 2009.

[22] D. A. Hill, M. T. Ma, A. R. Ondrejka, B. F. Riddle, M. T. Crawford, and R. T. Johnk. "Aperture Excitation of Electrically Large, Lossy Cavities". IEEE Transactions on Electromagnetic Compatibility, 36:169 – 178, 1994.

[23] C. H. Hodges and J. Woodhouse. "Theories of Noise and Vibration Transmission in Complex Structures". Reports on Progress in Physics, 49:107 – 170, 1986.

[24] C. L. Holloway, R. R. DeLyser, R. F. German, P. McKenna, and M. Kanda. "Comparison of Electromagnetic Absorber Used in Anechoic and Semi-Anechoic Chambers for Emissions and Immunit Testing of Digital Devices". IEEE Transactions on Electromagnetic Compatibility, 39(1):33 – 47, February 1997.

[25] C. L. Holloway, D. A. Hill, J. M. Ladbury, P. F. Wilson, G. Koepke, and J. Coder. "On the Use of Reverberation Chambers to Simulate a Rician Radio Environment for Testing of Wireless Devices". IEEE Transactions on Antennas and Propagation, 54(11):3167 – 3177, November 2006.

[26] C. L. Holloway, H. A. Shah, R. J. Pirkl, K. A. Remley, D. A. Hill, and J. Ladbury. "Early Time Behavior in Reverberation Chambers and Its Effect on the Relationships Between Coherence Bandwidth, Chamber Decay Time, RMS Delay Spread, and the Chamber Buildup Time". IEEE Transactions on Electromagnetic Compatibility, 54(4):714 – 725, August 2012.

[27] C. L. Holloway, H. A. Shah, R. J. Pirkl, W. F. Young, D. A. Hill, and J. Ladbury. "Reverberation Chamber Techniques for Determining the Radiation and Total Efficiency of Antennas". IEEE Transactions on Antennas and Propagation, 60(4):1758 – 1770, April 2012.

[28] C. L. Holloway, R. S. Smith, C. R. Dunlap, R. J. Pirkl, J. Ladbury, W. F. Young, D. A. Hill, W. R. Hansell, M. A. Shadish, and K. B. Sullivan. "Validation of a Two-Antenna Reverberation-Chamber Technique for Estimating the Total and Radiation Efficiency of Antennas". In 2012 International Symposium of Electromagnetic Compatability, pages 1 – 6, 2012.

[29] F. Jacobsen and A. R. Molares. "Sound Power Emitted by a Pure-Tone Source in a Reverberation Room". The Journal of the Accoustical Society of America, 126(2):676 – 684, August 2009.

[30] F. Jacobsen and A. R. Molares. "The Ensemble Variance of Pure-Tone Measurements in Reverberation Rooms". Journal of the Acoustical Society of America, 127(1):233 – 237, January 2010.

[31] E. Jakeman. "Enhanced Backscattering Through a Deep Random Phase Screen". Journal of Optical Society of America, 5(10):1638 – 1648, October 1988.

[32] J. G. Kostas and B. Boverie. "Statistical Model for a Mode-Stirred Chamber". IEEE Transactions on Electromagnetic Compatibility, 33(4):366 – 370, November 1991.

[33] J. Ladbury and D. A. Hill. "Enhanced Backscatter in a Reverberation Chamber: Inside Every Complex Problem is a Simple Solution Struggling to Get Out". In IEEE International Symposium on Electromagnetic Compatibility, pages 1 – 5, July 2007.

[34] J. Ladbury, G. Koepke, and D. Camell. "Evaluation of the NASA Langley Research Center Mode-Stirred Chamber Facility". In NIST Technical Note 1508. National Institute of Standards and Technology, January 1999.

[35] J. M. Ladbury and D. A. Hill. "An Improved Model for Antennas in Reverberation Chambers". In IEEE Internation Symposium on Electromagnetic Compatibility, pages 663 – 667, 2010.

[36] R. S. Langley and V. Cotoni. "The Ensamble Statistics of the Vibrational Energy Density of a Random System Subjected to Single Point Harmonic Excitation". Journal of Acoustical Society of America, 118(5):3064 – 3076, November 2005.

[37] F. B. J. Leferink, J. C. Boudenot, and W. van Etten. "Experimental Results Obtained in the Vibrating Intrinsic Reverberation Chamber". In IEEE International Symposium on Electromagnetic Compatibility, volume 2, pages 639 – 644, 2000.

[38] T. A. Loughry. "Frequency Stirring: An Alternative Approach to Mechanical Mode-Stirring for the Conduct of Electromagnetic Susceptibility Testing". Technical report, Phillips Airforce Laboratory, Kirtland Airforce Base, Albuquerque NM, November 1991. PL-TR–91-1036, AD-A243 551.

[39] D. Lubman. "Fluctuations of Sound with Position in a Reverberant Room". <u>The Journal of the Accoustical Society of America</u>, 44(6):1491 – 1502, 1969.

[40] L. C. Ludeman. <u>Random Processes: Filtering, Estimation, and Detection</u>. New York, NY, John Wiley & Sons, 2003.

[41] M. T. Ma, M. Kanda, M. L. Krawford, and E. B. Larsen. "A Review of Electromagnetic Compatibility/Interference Measurement Methodologies". <u>Proceedings of the IEEE</u>, 73(3):388 – 412, March 1985.

[42] A. A. Maradudin and E. R. Mendez. "Enhanced Backscatter of Light from Weak Rough, Random Metal Surfaces". <u>Journal of Applied Optics</u>, 32(19):3335 – 3343, July 1993.

[43] Institute of Electrical and Electronics Engineers. <u>IEEE Standard Dictionary of Electrical and Electronics Terms</u>. New York, NY, John Wiley & Sons, 1972.

[44] A. Papoulis and S. U. Pillai. <u>Probability, Random Variables, and Stochastic Processes</u>. New York, NY, McGraw-Hill, 2002.

[45] R. J. Pirkl. "Moments of the Truncated Complex Gaussian Distribution". In <u>NIST Technical Note 1560</u>. National Institute of Standards and Technology, November 2011.

[46] R. J. Pirkl, K. A. Remley, and C. S. Lotback. "Reverberation Chamber Measurement Correlation". <u>IEEE Transactions on Electromagnetic Compatibility</u>, 54(3):533 – 545, June 2012.

[47] D. M. Pozar. <u>Microwave Engineering</u>. New York, NY, John Wiley & Sons, 2005.

[48] V. Rajamani, C. Bunting, and J. West. "Differences in Quality Factor Estimation in Frequency and Time Domain". In <u>Asia-Pacific International Symposium on Electromagnetic Compatability</u>, pages 505 – 508, May 2012.

[49] T. S. Rappaport. <u>Wireless Communications Principles and Practice</u>. Upper Saddle River, NJ, Prentice Hall, 1996.

[50] K. A. Remley, R. J. Pirkl, A. S. Haider, and C. M. Wang. "Uncertainty From Choice of Mode-Stirring Technique in Reverberation-Chamber Measurements". Accepted for Publication IEEE Transactions on Electromagnetic Compatibility, 2013.

[51] R. E. Richardson. "Mode-Stirred Chamber Calibration Factor, Relaxation Time, and Scaling Laws". <u>IEEE Transactions on Instrumentation and Measurement</u>, IM-34(4):573 – 580, December 1985.

[52] K. Rosengren and P.-S. Kildal. "Radiation Efficiency, Correlation, Diversity Gain and Capacity of a Six-Monopole Antenna Array for a MIMO System: Theory, Simulation and Measurement in Reverberation Chamber". <u>IEEE Procedings of Microwave Antennas and Propagation</u>, 152(1):7 – 16, February 2005.

[53] M. R. Schroeder. "Measurement of Sound Diffusion in Reverberation Chambers". Journal of the Accoustical Society of America, 31(11):1407 – 1413, November 1959.

[54] M. R. Schroeder. "Frequency-Correlation FFunction of Frequency Responses in Rooms". Journal of the Accoustical Society of America, 34(12):1819 – 1823, December 1962.

[55] M. R. Schroeder. "Effect of Frequency and Space Averaging on the Transmission Responses of Multimode Media". Journal of the Accoustical Society of America, 46:277 – 283, 1969.

[56] R. Serra and F. Leferink. "Statistical Measurements of Fast Changing Electromagnetic Fields". In IEEE Internation Symposium on Electromagnetic Compatibility, pages 434 – 439, September 2010.

[57] S. van de Beek. "Characterizing Large-Form-Factor Devices in a Reverberation Chamber". Master's thesis, University of Twente, August 2012.

[58] S. van de Beek, R. Vogt-Ardatjew, H. Schipper, and F. Leferink. "Vibrating Intrinsic Reverberation Chamber for Shielding Effectiveness Measurements". In IEEE International Symposium on Electromagnetic Compatibility, pages 1 – 6, 2012.

[59] M. C. W. van Rossum and Th. M. Nieuwenhuizen. "Multiple Scattering of Classical Waves: Microscopy, Mesoscopy, and Diffusion". Reviews in Modern Physics, 71(1):313 – 371, January 1999.

[60] S. Wang, Z. Wu, G. Wei, Y. Cui, and L. Fan. "A New Method of Estimating Reveration Chamber Q-Factor with Experimental Validation". Progress in Electromagnetics Research Letters, 36:103 – 112, 2013.

[61] R. Waterhouse. "Statistical Properties of Revberant Sound Fields". Journal of the Accoustical Society of America, 43(6):1436 – 1444, 1968.

[62] R. L. Weaver and J. Burkhardt. "Weak Anderson Localization and Enhanced Backscatter in Reverberation Rooms and Quantum Dots". Journal of the Acoustical Society of America, 96(5):3186 – 3190, November 1994.

[63] S.-P. Yu and C. F. Bunting. "Statistical Investigation of Frequency-Stirred Reverberation Chambers". In IEEE International Symposium on Electromagnetic Compatibility, pages 155 – 159, 2003.

Appendix A

Statistical Notation and Concepts

Measured components of EM fields in RCs are considered to be random variables. While this is not strictly true, unless an infinite number of samples are taken, making this assumption simplifies the analysis process. In the following, the statistical notation and concepts used throughout this thesis will be presented, and the difference between a true random variable and an approximation using measured data will be explained.

A.1   Single Random Variable

A random function of the variable $Y(x) = y$ has the following two conditions:

$$P\{x : Y(x) = \pm\infty\} = 0$$

$$\{x : Y(x) \leq y\} \subset \Re \qquad \forall x$$

where P denotes "the probability of", and $\Re$ is the set of all real numbers. The first condition simply states that the random variable is bounded. The second condition must be met in order to guarantee the existence of the Cumulative Distribution Function. To satisfy these conditions Y must be a finite, real number. This definition works for the purposes of RC analysis because of the statistical independence of the real and imaginary parts of the field quantities.

The Cumulative Distribution Function (CDF) has the following definition [40]:

$$F_Y(x) \triangleq P\{x : Y(x) \leq y\} = P\{Y \leq y\} \tag{A.1}$$

which also has three conditions:

$$0 \leq F_Y(x) \leq 1 \qquad \forall x$$

$$F_Y(x_2) \geq F_Y(x_1) \qquad \text{for } x_2 > x_1$$

$$\lim_{a \to 0^+} F_Y(x + a) = F_Y(x)$$

These three conditions state that the CDF is bounded from above and below, is non-decreasing, and is continuous from the right, respectively. The CDF can be used to easily calculate the probability that Y will be within a given range of values. For example:

$$P\{a < Y \leq b\} = F_Y(b) - F_Y(a)$$

Another important use of the CDF is to find the Probability Density Function (PDF) of the random variable, defined by:

$$f_Y(x) \triangleq \frac{d}{dx} F_Y(x) \tag{A.2}$$

Thus, the CDF can also be found from the PDF by:

$$F_Y(x) = \int_{-\infty}^{x} f_Y(x) dx \tag{A.3}$$

Properties of the PDF are that it is positive for the entire range of x, the integral over all x must be unity, and like the CDF, can be used to calculate probabilities of events. However, since calculating the probabilities of events requires solving the same integral over different ranges, it is often just easier to first find the CDF and then proceed with finding the required probabilities.

The PDF and CDF are what are called total characterizations of the random variable. It is not always easy, or possible, to find an exact total characterization of a random variable. Even so, it is often valuable to at least obtain partial characterizations of a random variable, which can facilitate useful approximations to the PDF and CDF. The two partial characterizations that will be used in this thesis are:

$$\mu_Y = E[Y(x)] = \int_{-\infty}^{\infty} x f_Y(x) dx \tag{A.4}$$

$$\text{var}(Y) = E\left[(Y(x) - \mu_Y)^2\right] = \int_{-\infty}^{\infty} (x - \mu_Y)^2 f_Y(x) dx \tag{A.5}$$

where μ_Y is the mean and $\text{var}(Y)$ is the variance, respectively. Some fairly simple random variable distributions can be described using only the mean and variance, such as uniform and Gaussian distributions. However, more complicated systems will require higher orders of partial characterizations, such as moments of order k which are found by replacing x with x^k in the integral of (A.4).

Another way in which to view the PDF is through use of the Characteristic Function ϕ_Y. It is defined through the Fourier transform pair:

$$\phi_Y(\omega) = \int_{-\infty}^{\infty} f_Y(x) e^{j\omega x} dx = E\left[e^{j\omega Y(x)}\right] \tag{A.6}$$

$$f_Y(x) = \frac{1}{2\pi} \int_{-\infty}^{\infty} \phi_Y(\omega) e^{-j\omega x} d\omega \tag{A.7}$$

As usual, the Fourier transform is a tool that can be employed when it is convenient to do so. Depending on the random variable, it may be beneficial to use the Characteristic Function rather than the CDF, or vice versa. Another related function that can be useful for analyzing random variables is the moment generating function:

$$\mathfrak{M}_Y(t) \triangleq \int_{-\infty}^{\infty} f_Y(x) e^{tx} dx = E\left[e^{tY(x)}\right] \tag{A.8}$$

where the kth moment of the random variable Y is found as:

$$E\left[Y^k\right] = \frac{\partial^k \mathfrak{M}_Y(t)}{\partial^k t}\Big|_{t=0} \tag{A.9}$$

A.2   Discretely Sampled Data

The random variable Y is a statistical representation for some measurable quantity. By the central limit theorem, a set of measured data M will more closely approximate Y as the number of independent samples in M goes to infinity. A common notation that will be used in this thesis is the ensemble average of a set of measured data M, denoted by $\langle M \rangle$. The variance of M will be denoted as σ_M^2, and the standard deviation by σ_M. The ensemble average for a measured set of

data is given by:

$$\langle M \rangle = \frac{1}{N} \sum_N M \qquad (A.10)$$

where N is the number of samples in M. The variance of M is given by:

$$\sigma_M^2 = \left\langle |M - \langle M \rangle|^2 \right\rangle \qquad (A.11)$$

If the limit is taken as $N \to \infty$ we obtain:

$$\lim_{N \to \infty} \langle M \rangle = \mu_Y \qquad (A.12)$$

$$\lim_{N \to \infty} \sigma_M^2 = \text{var}(Y) \qquad (A.13)$$

Two sets of measured data taken at different locations, polarization angles and/or frequencies in an ideal RC are statistically independent. To test this for measured data in a real RC the coefficient of correlation can be calculated with discrete data sets using:

$$\rho_{M_1, M_2} = \frac{\sigma_{M_1, M_2}^2}{\sigma_{M_1}^2 \sigma_{M_2}^2} \qquad (A.14)$$

where the covariance σ_{M_1, M_2}^2 is defined by:

$$\sigma_{M_1, M_2}^2 = \left\langle |M1 - \langle M1 \rangle||M2 - \langle M2 \rangle| \right\rangle \qquad (A.15)$$

Perfect statistical independence of two data sets result in a coefficient of correlation with a value of 0.

A useful quantity often used in RC analysis is the power delay profile given in Section 2.5 by (2.47). A related quantity is the power spectral density $R_M(\Delta f)$ defined as the autocorrelation of data collected in the frequency-domain by [40]:

$$R_M(\Delta f) \triangleq E[M(f)M^*(f + \Delta f)] = \left\langle \int_0^\infty M(f)M^*(f + \Delta f) \right\rangle \qquad (A.16)$$

The PDP and R_M are Fourier transform pairs per the Wiener-Khinchin theorem given by [44]:

$$R_M(\Delta f) = \int_{-\infty}^\infty PDP(\tau)\mathrm{e}^{-j2\pi\Delta f\tau} d\tau \qquad (A.17)$$

and

$$PDP(\tau) = \frac{1}{2\pi} \int_{-\infty}^\infty R_M(\Delta f)\mathrm{e}^{j2\pi\Delta f\tau} d\Delta f \qquad (A.18)$$

where Δf and τ are relative frequency and delay, respectively.

Appendix B

Accounting for Antenna Imperfections in RC Measurements

Given the power diagram depicted in Figure 2.6, the power transmitted by antenna A, P_{Tx}, is given by the product of the input power, P_1, and total efficiency, $\eta_{T,A}$, to antenna A [3]:

$$P_{Tx} = \eta_{T,A} P_1 \tag{B.1}$$

Additionally, the power reflected back to the source P_3, is given by the product of the power reflected and scattered back to antenna A, P_{rf}, and $\eta_{T,A}$:

$$P_3 = \eta_{T,A} P_{rf} \tag{B.2}$$

Lastly, the power sent to the receiver from antenna B, P_2, is given by the product of the power received, P_{Rx}, and total efficiency, $\eta_{T,B}$, of antenna B:

$$P_2 = \eta_{T,B} P_{Rx} \tag{B.3}$$

The total efficiency is typically broken into efficiency due to antenna mismatch and material properties as:

$$\eta_T = \eta_r \eta_{cd} \tag{B.4}$$

where

$$\eta_r = 1 - |\Gamma|^2 \tag{B.5}$$

is the reflection efficiency, η_{cd} is the radiation efficiency, and Γ is the reflection coefficient of the antenna. The reason for this separation of efficiency terms is the difference in what causes the reduction in power and where the lost power goes. The reflection efficiency accounts for the reduction

in power that is due to the antenna's impedance mismatch. The power lost is either reflected back to the source or is scattered inside the RC depending on which direction the power is flowing. The radiation efficiency accounts for the reduction in power due to material loss that is generally dominated by the finite conductance of conductors and dielectrics, which can be enhanced by structural imperfections such as surface roughness. The power lost in this case is converted to heat.

The contribution of antenna mismatch and efficiency to the measured powers will each be handled separately, and the results can be combined at the end to obtain the contribution of both. First the effect of antenna material losses will be treated.

B.1   Antenna Material Loss

If the antenna is perfectly matched, then (B.1), (B.2) and (B.3) reduce to:

$$P_{Tx} = \eta_{cd,A} P_1 \qquad P_{Rx} = \frac{P_2}{\eta_{cd,B}} \qquad P_{rf} = \frac{P_3}{\eta_{cd,A}} \tag{B.6}$$

If the antenna is in the working volume of the RC, then the environment is not in the nearfield of the antenna, causing redistribution of the antenna currents from their values in isolation. If this assumption holds, the mean powers are simply:

$$\langle P_{Tx} \rangle = \eta_{cd,A} \langle P_1 \rangle \qquad \langle P_{Rx} \rangle = \frac{\langle P_2 \rangle}{\eta_{cd,B}} \qquad \langle P_{rf} \rangle = \frac{\langle P_3 \rangle}{\eta_{cd,A}} \tag{B.7}$$

This assertion does not hold at low frequencies or when the antenna is placed too close to the walls of the RC.

B.2   Antenna Impedance Mismatch

For antennas that have perfect radiation efficiency, the losses due to antenna mismatch are written as:

$$P_{Tx} = \eta_{r,A} P_1 \qquad P_{Rx} = \frac{P_2}{\eta_{r,B}} \qquad P_{rf} = \frac{P_3}{\eta_{r,A}} \tag{B.8}$$

Now the average transmitted, received, and reflected powers inside the RC can be written as:

$$\langle P_{Tx} \rangle = \langle \eta_{r,A} P_1 \rangle \tag{B.9}$$

$$\langle P_{Rx} \rangle = \left\langle \frac{P_2}{\eta_{r,B}} \right\rangle \tag{B.10}$$

$$\langle P_{rf} \rangle = \left\langle \frac{P_3}{\eta_{r,A}} \right\rangle \tag{B.11}$$

Further simplification of (B.9) to (B.11) requires that the reflection coefficient and other properties of the antenna are precisely defined. To that end, the cascaded network shown in Figure 2.7 is modified such that antenna A is connected to a lumped impedance element Z_L as in Figure B.1. In the following, this impedance will be used to represent the antenna placed in free space and in the RC. This is done in order to separate the intrinsic reflection and transmission properties of the antenna from those of the RC.
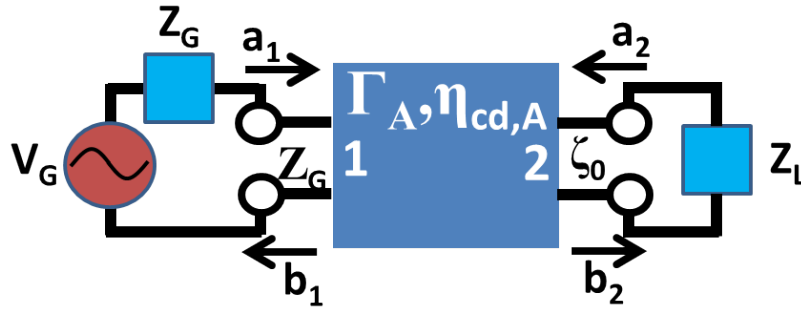

Figure B.1: Simplification of the diagram of Figure 2.7 in which the RC and antenna B are replaced by a single, lumped impedance Z_L that is set based on the choice of environment. A source is connected to the left of antenna A with source voltage V_G, and impedance Z_G.

The antenna's intrinsic reflection and transmission properties are determined by placing the antenna in an infinite medium of the RC cavity material. Assuming the cavity medium is homogeneous, this is achieved in the model by setting the lumped impedance to a constant given by:

$$Z_L = \zeta_0 \tag{B.12}$$

where ζ_0 is the intrinsic impedance of the RC cavity, which is generally assumed to be that of free space, 120π Ω. Using forward and backward wave notation [47], with a_1, b_1, a_2, and b_2 shown in

Figure B.1, the S-parameters and the wave amplitudes are related by:

$$b_1 = S_{11}a_1 + S_{12}a_2 \tag{B.13}$$

$$b_2 = S_{21}a_1 + S_{22}a_2 \tag{B.14}$$

Since the antenna A network element contains the effect of all of the antenna's imperfections, the output transmission line is considered perfectly matched to ζ_0 such that:

$$a_2 = 0 \tag{B.15}$$

With this the reflection and transmission coefficients are defined as:

$$\Gamma_A \triangleq \left. \frac{b_1}{a_1} \right|_{a_2=0} = S_{11} \tag{B.16}$$

$$\mathcal{T}_A \triangleq \left. \frac{b_2}{a_1} \right|_{a_2=0} = S_{21} \tag{B.17}$$

Next the scattering properties must be found looking to the left.
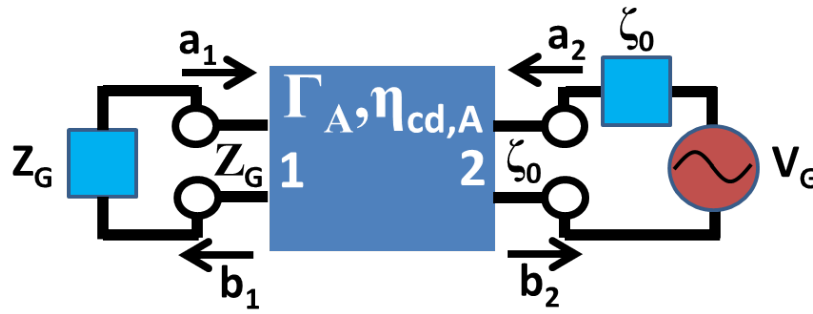

Figure B.2: Conceptual diagram for definition of antenna scattering. A new source is connected on the right with voltage V_G, and impedance ζ_0. The left side of antenna A is now terminated with impedance Z_G.

To get the transmission and reflection looking to the left, the model is again modified as in Figure B.2. This time a source is connected on the right side and has a source impedance of ζ_0, and the left side is terminated with a matched load equal to Z_G of the original source. Once again

the wave amplitudes are given by (B.13) and (B.14). This time we have a matched load on the left which gives:

$$a_1 = 0 \tag{B.18}$$

The antenna network element is passive and is also assumed to be reciprocal, which means that the transmission coefficient is the same in both directions. In this configuration the transmission coefficient is found as:

$$\mathcal{T}_A \triangleq \left. \frac{b_1}{a_2} \right|_{a_1=0} = S_{12} \tag{B.19}$$

Reciprocity does not imply that the reflection coefficients are the same, and in fact the mechanism of reflection in this case is completely different. An EM wave incident on an antenna will scatter some portion of the fields, even if it is perfectly matched. This is simply a property of the antenna being constructed from highly conductive metals. Thus, the field reflected from waves incident on the right side of antenna A, as shown in Figure B.2, is scattered. Therefore, the reflection coefficient of antenna A, looking to the left, is instead denoted as the scattering coefficient $\mathcal{S}_A$ and is given by:

$$\mathcal{S}_A \triangleq \left. \frac{b_2}{a_2} \right|_{a_1=0} = S_{22} \tag{B.20}$$

An important distinction between Γ_A and $\mathcal{S}_A$ is that at a single frequency Γ_A is a constant. On the other hand, $\mathcal{S}_A$ depends on angle of incidence and polarization of the measured field.

With the reflection coefficient of antenna A defined as (B.16), the reflection efficiency is:

$$\eta_{r,A} = 1 - |\Gamma_A|^2 \tag{B.21}$$

Performing the same operations on antenna B, the reflection efficiency is obtained as:

$$\eta_{r,B} = 1 - |\Gamma_B|^2 \tag{B.22}$$

Like the radiation efficiency η_{cd}, the reflection efficiency η_r is intrinsic to the antenna and does not change when the antenna is placed in the working volume of the RC. Thus (B.9) - (B.11) can be simplified as:

$$\langle P_{Tx} \rangle = \eta_{r,A} \langle P_1 \rangle \tag{B.23}$$

$$\langle P_{Rx} \rangle = \frac{\langle P_2 \rangle}{\eta_{r,B}} \tag{B.24}$$

$$\langle P_{rf} \rangle = \frac{\langle P_3 \rangle}{\eta_{r,A}} \tag{B.25}$$

With these relationships, if the reflection coefficient of the antenna is known, i.e. measured before-hand in free space, then (B.23) - (B.25) can be used to relate the measured power to the power inside the RC. While it seems fairly straightforward to make the additional free space measurement of the antenna in order to characterize its reflection coefficient, uncertainties involving movement of the test equipment, use of different test equipment, and/or non-ideal properties of the measurement environment may make it difficult to achieve low error in the measurement. If the reflection coefficient could be estimated using the RC data then many of these uncertainties would be reduced or vanish altogether. This will be explored in the next section.

B.3   Reflection Measurement in RCs

An assumption that is very often made in RC measurements is that the reflection coefficient of the antenna is approximately equal to the mean of the measured reflection as:

$$\Gamma \approx \langle S_{11} \rangle \tag{B.26}$$

While the added uncertainty in making this assumption is usually very low, there are cases in which it can lead to large errors. Thus, it is important to understand when this assumption can be made. The model shown in Figure B.1 is once again used, but this time the lumped impedance element Z_L is used to model the reflection properties of the RC. As such, we set $Z_L = Z_{RC}$ and the scattering coefficient of this stochastic RC impedance, $\mathcal{S}_{RC}$, is given the following properties:

- $|\mathcal{S}_{RC}| = |s|$ is a random variable bounded between $0 \leq r \leq 1$, with probability density function $f_{\mathcal{S}_{RC}}(r)$.

- $\langle \mathcal{S}_{RC} \rangle = 0$

- $\angle \mathcal{S}_{RC} = \phi$ is a random variable that is uniformly distributed and bounded by 0 and 2π.

- $|\mathcal{S}_{RC}|$ and $\angle\mathcal{S}_{RC}$ are statistically independent.

Using this model and the results from the previous section, the terms included in an RC S_{11} measurement can be determined.

Given Γ_A, $\mathcal{T}_A$, $\mathcal{S}_A$, and $\mathcal{S}_{RC}$, the forward and backward waves for Figure B.1, with stochastic impedance Z_{RC}, can be written as:

$$b_1 = \Gamma_A a_1 + \mathcal{T}_A a_2 \tag{B.27}$$

$$b_2 = \mathcal{T}_A a_1 + \mathcal{S}_A a_2 \tag{B.28}$$

$$a_2 = \mathcal{S}_{RC} b_2 \tag{B.29}$$

Combining (B.28) and (B.29) we get:

$$b_2 = \mathcal{T}_A a_1 + \mathcal{S}_A \mathcal{S}_{RC} b_2 \tag{B.30}$$

Combining (B.29) and (B.30), and solving for a_2 we get:

$$a_2 = \frac{\mathcal{T}_A \mathcal{S}_{RC} a_1}{1 - \mathcal{S}_A \mathcal{S}_{RC}} \tag{B.31}$$

With the solution of a_2 in terms of a_1, (B.31) can be combined with (B.27) to give:

$$b_1 = a_1 \left[\Gamma_A + \frac{\mathcal{T}_A^2 \mathcal{S}_{RC}}{1 - \mathcal{S}_A \mathcal{S}_{RC}}\right] \tag{B.32}$$

Now, since $S_{11} = \frac{b_1}{a_1}$ the ensemble average of S_{11} is:

$$\langle S_{11}\rangle = \left\langle \Gamma_A + \frac{\mathcal{T}_A^2 \mathcal{S}_{RC}}{1 - \mathcal{S}_A \mathcal{S}_{RC}}\right\rangle \tag{B.33}$$

Since Γ_A and $\mathcal{T}_A$ are constants, (B.33) can be simplified to:

$$\langle S_{11}\rangle = \Gamma_A + \mathcal{T}_A^2 \left\langle \frac{\mathcal{S}_{RC}}{1 - \mathcal{S}_A \mathcal{S}_{RC}}\right\rangle \tag{B.34}$$

Using the properties defined for $\mathcal{S}_{RC}$, it can be re-written as:

$$\mathcal{S}_{RC} = |s|\mathrm{e}^{-j\phi} \tag{B.35}$$

which makes (B.34):

$$\langle S_{11} \rangle = \Gamma_A + \mathcal{T}_A^2 \left\langle \frac{|s|e^{-j\phi}}{1 - \mathcal{S}_A|s|e^{-j\phi}} \right\rangle \tag{B.36}$$

Expanding the terms in $\langle \cdot \rangle$ into its geometric series gives:

$$\langle S_{11} \rangle = \Gamma_A + \mathcal{T}_A^2 \left\langle \sum_{n=0}^{\infty} \mathcal{S}_A^n |s|^{n+1} e^{-j\phi(n+1)} \right\rangle \tag{B.37}$$

Given the independence of the terms in $\langle \cdot \rangle$, (B.37) can be simplified to:

$$\langle S_{11} \rangle = \Gamma_A + \mathcal{T}_A^2 \sum_{n=0}^{\infty} \mathcal{S}_A^n \left\langle |s|^{n+1} \right\rangle \left\langle e^{-j\phi(n+1)} \right\rangle \tag{B.38}$$

If we take $\langle e^{-j\phi(n+1)} \rangle$ to the limit of containing an infinite number of independent samples then it can be evaluated using the expected value given by Equation A.4. Within the limits of ϕ the PDF is uniformly distributed and equal to $\frac{1}{2\pi}$, making the expected value of $e^{-jn\phi}$:

$$
\begin{aligned}
E[e^{-jn\phi}] &= \int_{-\pi}^{\pi} \frac{e^{-jn\phi}}{2\pi} r \, d\pi & \text{(B.39)} \\
&= \frac{r}{2\pi} \int_{-\pi}^{\pi} e^{-jn\phi} d\pi & \text{(B.40)} \\
&= -\frac{r}{2jn\pi} e^{-jn\phi} \big|_{-\pi}^{\pi} & \text{(B.41)} \\
&= \frac{r}{n\pi} \frac{e^{jn\pi} - e^{-jn\pi}}{2j} & \text{(B.42)} \\
&= \frac{r}{n\pi} \sin(n\pi) = 0 & \text{(B.43)}
\end{aligned}
$$

In addition, given the bounds of $|s|$ between 0 and 1, gives the final result of:

$$\langle S_{11} \rangle = \Gamma_A \tag{B.44}$$

Again, keeping in mind that (B.44) is only valid when:

$$\langle e^{-j\phi(n+1)} \rangle \approx E[e^{-jn\phi}]$$

This result was also obtained in [35] using the integral form of (B.36). Importantly, if the phase is not uniformly distributed then (B.44) will not hold. Thus, it is critical to the uncertainty of RC measurement results that measured data sets contain a large number of independent samples.